UNIVERSIDAD COMPLUTENSE DE MADRID

FACULTAD DE CIENCIAS FÍSICAS

Departamento de Óptica

TESIS DOCTORAL

Photonic devices based on sol-gel and on silicon

Dispositivos fotónicos con base sol-gel y de silicio

MEMORIA PARA OPTAR AL GRADO DE DOCTOR

PRESENTADA POR

Aitor Villafranca Velasco

Directores

María Luisa Calvo
Pavel Cheben

Madrid, 2013

Interdisciplinary Group for Optical Computing (GICO)
Complutense University of Madrid

Philosophy Doctor Thesis

Photonic devices based on sol-gel and on silicon

Dispositivos fotónicos con base sol-gel y de silicio.

Author: Aitor Villafranca Velasco
Advisors: María Luisa Calvo and Pavel Cheben

Thesis presented in fulfillment of the doctorate program of Optics Department,
Faculty of Physics, Complutense University of Madrid
March 2013

To my parents

Acknowledgements

First of all, I am extremely indebted to María Luisa Calvo, who welcomed me into this path and has guided me every step of the way with an unlimited dedication and support. I would also like to express my deepest gratitude to Pavel Cheben, whose mentorship has been an invaluable gift, and towards whom I will always profess a tremendous admiration.

During the years I have devoted to this doctorate, I have had the pleasure to work with great partners and collaborators. I would like to start by thanking everyone in the GICO group at the Complutense University for their help and support: Tania, Jose, Óscar, Maripaz, and specially, Álex, who has been (literally and figuratively) by my side during all this journey.

One of the best experiences of these past years has been the chance to work at the National Research Council of Canada. I want to thank again Siegfried Janz for that opportunity, as well as all the people who I had the honor to work with during those months: Dan-Xia Xu, Jens Schmid, André Delâge, Mirek Florjańczyk, Przemek Bock, and Martin Vachon.

I would also like to mention other excellent researchers I have been lucky enough to collaborate with: Iñigo Molina, Alejandro Ortega and Carlos Alonso, from the University of Malaga (ETSI Telecomunicación); Francisco Del Monte from CSIC; Pablo Dominguez and Miguel Ángel Rubio from UNED; and Svatopluk Civiš from the Academy of Sciences of the Czech Republic.

In the financial aspect, I would like to acknowledge the support from the Spanish Ministry of Economy (formerly as an independent Ministry of Science) through grants TEC2008-04105 and TEC2011-23629.

I would like to conclude these lines by thanking my family and friends, who have believed in all my projects and have made my life happier and more complete during these past years. In particular, I want to thank my parents, to whom this thesis is dedicated, for all their sacrifices and unconditional support, for putting all my needs ahead of their own, and for always expecting the best from me. Finally, my unlimited gratitude goes to my brother Asier, whose ability to solve all my problems with a couple of words still amazes me. Having you by my side makes any goal feasible and any journey worth taking. Thank you.

Table of contents

Resumen: Dispositivos fotónicos con base sol-gel y de Silicio

INTRODUCCIÓN Y OBJETIVOS

En las últimas décadas, los dispositivos fotónicos han sido objeto de una gran atención dentro de la comunidades científica y empresarial, gracias a su incomparable potencial para resolver las crecientes necesidades de ancho de banda de los usuarios, así como una herramienta esencial de observación del mundo que nos rodea. La espectroscopía óptica nos ha permitido acercarnos a la comprensión de algunos de los fenómenos a mayor escala del universo [Albert'11, Wilken'12], tales como el análisis de exoplanetas en busca de marcadores biológicos [Schwartz'12]; pero también de las partículas más pequeñas que conforman nuestra realidad [Yang'09, Mak'10, Nakajima'11]. La capacidad, precisión y distancia máxima de los enlaces ópticos está en continuo crecimiento [Predehl'12, Sakaguchi'11], y las interconexiones ópticas están dando forma al futuro de las redes de comunicaciones y de los supercomputadores [Alduino'07, Jalali'07]. A estas aplicaciones, se suman muchas otras, como por ejemplo sensores biológicos y ambientales [Densemore'07], sistemas ópticos de almacenamiento de datos [Haw'03], y conformado de haces para litografía [Dickey'03] o pinzas ópticas [Novotny'97], entre muchos otros.

En este marco, los requisitos impuestos sobre la eficiencia, calidad y tamaño de los dispositivos fotónicos son cada vez más exigentes. Es por ello, que el objetivo principal de los trabajos presentados en esta tesis es el diseño, fabricación y caracterización de dispositivos fotónicos altamente eficientes y competitivos para la manipulación óptica de espectros y de la polarización. Para ello, se han utilizado dos plataformas fotónicas complementarias, los vidrios holográficos fotopolimerizables y los circuitos fotónicos integrados en silicio, aprovechando las virtudes derivadas de la forma en la que cada una de ellas permite diseñar la distribución espacial de su índice de refracción. Por una parte, la óptica integrada en silicio presenta un elevado contraste de índice de refracción (Δn ~ 2) que permite implementar estructuras de guías de onda con un elevado confinamiento de modos ópticos, maximizando la densidad de integración de los dispositivos. Por el contrario, los vidrios fotopolimerizables presentan un contraste de índice menor, pero proporcionan la posibilidad de diseñar libremente en tres dimensiones las estructuras fotónicas, permitiendo implementar elementos difractivos de gran eficiencia y calidad óptica.

Los vidrios fotopolimerizables [Cheben'01] son un material holográfico sintetizado mediante técnicas sol-gel, que presenta una elevada modulación de índice de refracción, calidad óptica, eficiencia de difracción, sensibilidad, y estabilidad estructural [Calvo'06, Martínez'09, Martínez'10]. La incorporación a dichos vidrios de especies de alto índice de refracción (HRIS, *High Refractive Index Species*) basadas en circonio [DelMonte'06] ha permitido alcanzar cotas aún mayores de modulación de índice (Δn ~ 0.01), convirtiendo a este fotomaterial en un candidato ideal para la implementación de memorias holográficas [Haw'03]. Sin embargo, los vidrios fotopolimerizables típicamente presentan un espesor limitado a unas 200 µm, condicionando su aplicación a filtros holográficos [Barbastathis'99, Rakuljic'93, Quintanilla'81, Schoen'93]. Los objetivos concretos de esta tesis en lo referido a dispositivos fotónicos con base sol-gel son, por lo tanto, el desarrollo de una nueva formulación y técnica de síntesis para superar las limitaciones en espesor de los vidrios fotopolimerizables, la implementación de filtros de supresión de banda (*notch*) que aprovechen dicho espesor para lograr un ancho de banda reducido, y la investigación en métodos de síntesis sostenibles para este tipo de fotomaterial.

La plataforma de silicio sobre aislante (SOI, *Silicon-On-Insulator*) [Reed'08, Lockwood'10], impulsada por su bajo coste de producción y su capacidad de integración con la tecnología CMOS (*Complementary Metal Oxide Semiconductor*), ha experimentado grandes avances en los últimos años. El motor principal de la investigación en esta plataforma fotónica han sido las interconexiones ópticas [Kirchain'07], que pretenden superar el límite de ancho de banda proporcionado por las conexiones de cobre, pero su rango de aplicación incluye astronomía [Florjańczyk'12], espectroscopía [Cheben'07a], y sensado biológico y ambiental [Densemore'07], entre muchos otros. En particular, los objetivos de los trabajos presentados en esta tesis se centran en el desarrollo de dispositivos pasivos en silicio, y más concretamente, de espectrómetros, filtros, demultiplexadores y rotadores de polarización de alta eficiencia en un tamaño reducido (entre 10 µm × 450 nm y 10 mm^2 dependiendo del dispositivo). Estos dispositivos pretenden proponer alternativas competitivas a las conocidas en el estado de la técnica, tales como rotadores de polarización basados en la propagación de modos híbridos [Yamauchi'08, Brooks'06], y demultiplexadores y espectrómetros basados en AWGs (*Arrayed Waveguide Gratings*) [Cheben'07b, Pearson'00, Ohno'06] y redes *echelle* en guías de onda [Janz'04, Bidnyk'06, Brouckaert'07].

CONTENIDO DE LA INVESTIGACIÓN

A partir de los objetivos descritos, la presente tesis doctoral proporciona las siguientes aportaciones fundamentales:

- Se ha desarrollado una nueva fórmula y método de síntesis de vidrios fotopolimerizables incorporando especies de alto índice de refracción, que permiten superar las limitaciones de espesor del fotomaterial, llegando hasta 500 µm sin fracturas ni gelificación inhomogénea. Los vidrios sintetizados con esta técnica mantienen una elevada modulación de índice de refracción y una excelente calidad óptica. Presentan asimismo una elevada responsividad, que permite grabar dispositivos holográficos altamente eficientes con una sola exposición de corta duración y baja potencia, reduciendo asimismo el *scattering* resultante.

- Utilizando como soporte los vidrios holográficos de espesor elevado se han implementado filtros holográficos altamente selectivos, tanto paso-banda como de supresión de banda (*notch*). El aumento de espesor permite reducir el ancho de banda de los filtros, habiéndose demostrado un ancho de banda de tan sólo 0.3 nm, con una supresión de banda de -27.5 dB y un rizado de tan sólo 0.1 dB en la banda de paso. Los filtros fabricados presentan una excelente calidad óptica, bajo *scattering*, y una gran libertad de diseño. Sus prestaciones los convierten, por ejemplo, en candidatos ideales para la supresión de la línea de Rayleigh en espectroscopía Raman [Xie'02, Carrabba'90].

- Se ha estudiado la incorporación de líquido iónico a la composición de los vidrios fotopolimerizables en un intento de favorecer los procesos de fotopolimerización. Los efectos de dicha incorporación, tanto en materiales con y sin HRIS, se ha analizado en términos de modulación de índice de refracción, eficiencia de difracción, calidad óptica, dinámicas de difusión dentro de la matriz vítrea, viscosidad de la solución inicial, y *scattering* de las muestras antes y después de la grabación de redes de difracción holográficas.

- Se ha demostrado experimentalmente un nuevo tipo de espectrómetros integrados en silicio sobre aislante, en concreto, un espectrómetro de transformada de Fourier espacialmente heterodino que comprende un conjunto de interferómetros Mach Zehnder con diferencias de caminos ópticos crecientes a lo largo del *array*. Esta configuración genera un patrón estacionario de salida dependiente de la longitud de onda, a partir del cual el espectro original de la señal puede ser recuperado mediante técnicas computacionales, también desarrolladas para este trabajo de tesis doctoral. Dichas técnicas de recuperación espectral permiten asimismo corregir desviaciones de fabricación del sistema sin utilizar elementos activos adicionales. Gracias al uso de espirales enrolladas de forma compacta, se ha demostrado experimentalmente una resolución de hasta 40 pm en un tamaño de chip de tan sólo 12 mm^2.

- Se ha diseñado, fabricado y caracterizado un conversor de modos de polarización ultracompacto, capaz de alcanzar una conversión de modo TE a TM de hasta el 97.5% en una longitud de tan sólo 10 μm. El conversor de polarización se basa en el grabado de dos hendiduras asimétricas en una guía de onda de silicio, y puede ser implementado en un sólo paso de grabado al aprovechar la dependencia entre anchura y profundidad de grabado para anchuras reducidas (*RIE lag, Reactive Ion Etch lag*).
- Se ha demostrado experimentalmente un multiplexador/demultiplexador de banda ancha implementado mediante una red de difracción grabada en la pared lateral de una guía de onda curvada. Las medidas experimentales muestran una interferencia entre canales adyacentes de tan sólo -25 dB, pudiendo llegar hasta los -35 dB mediante la integración de etapas de demultiplexado consecutivas. El tamaño del dispositivo es de 100 μm × 160 μm, reduciendo significativamente el de otras alternativas tales como AWGs y proporcionando una mayor resistencia a errores de fabricación.
- A partir de la tecnología de redes de difracción en pared lateral, se ha diseñado, fabricado y caracterizado un filtro paso banda con dos etapas de filtrado en cascada para conseguir una notable ratio de rechazo de las bandas de supresión de hasta -40 dB en un dispositivo de 300 μm × 500 μm. El dispositivo proporciona un ancho de banda de 6.2 nm con una caída de - 4 dB/nm en los bordes de la banda de paso.

CONCLUSIONES

Todos los resultados descritos se integran dentro de un propósito común de proporcionar nuevos dispositivos fotónicos pasivos de altas prestaciones que permiten manipular y analizar el espectro y la polarización de la luz en una amplia gama de aplicaciones, tales como espectroscopía, comunicaciones ópticas, astronomía, y sensado biológico y ambiental, entre otros. Los dispositivos presentados, implementados en vidrios fotopolimerizables y silicio sobre aislante, aprovechan al máximo las virtudes particulares de estas plataformas, consiguiendo notables avances en el estado de la técnica de la óptica difractiva e integrada, y abren prometedoras vías de investigación e industrialización en el campo de los dispositivos fotónicos.

REFERENCIAS

[Albert’11] S. Albert, K. K. Albert, P. Lerch and M. Quack, *Faraday Discuss.* **150**, 71 (2011).

[Alduino’07] A. Alduino and M. Paniccia, *Nat. Photonics* **1**, 153 (2007).

[Barbastathis’99] G. Barbastathis, M.Balberg, and D. J. Brady, *Opt. Lett.* **24**, 811 (1999).

[Bidnyk’06] S. Bidnyk, D. Feng, A. Balakrishnan, M. Pearson, M. Gao, H. Liang, W. Qian, C.-C. Kung, J. Fong, J. Yin, and M. Asghari, *IEEE Photon. Technol. Lett.* **18**, 2392 (2006).

[Brooks’06] C. Brooks, P. E. Jessop, H. Deng, D. O. Yevick, and G. Tarr, *Opt. Eng.* 45, 044603 (2006).

[Brouckaert’07] J. Brouckaert, G. Roelkens, D. Van Thourout and R. Baets, *Phot. Tech. Lett.* **19**, 1484 (2007).

[Calvo’06] M. L. Calvo, P. Cheben, Ó. Martínez-Matos, F. del Monte, and J. A. Rodrigo, *Phys. Rev. Lett.* **97**, 084801 (2006).

[Carrabba’90] M. M. Carrabba, K. M. Spencer, C. Rich and D. Rauh, *Appl. Spectrosc.* **44**, 1558 (1990).

[Cheben’01] P. Cheben and M.L. Calvo, *Appl. Phys. Lett.* **78**, 1490 (2001).

[Cheben‘07a] P. Cheben, J. H. Schmid, A. Delâge, A. Densmore, S. Janz, B. Lamontagne, J. Lapointe, E. Post, P. Waldron, and D.-X. Xu, *Opt. Express* **15**, 2299 (2007).

[Cheben‘07b] P. Cheben, "Wavelength dispersive planar waveguide devices: Echelle gratings and arrayed waveguide gratings,” in *Optical Waveguides: From Theory to Applied Technologies* (eds. M. L. Calvo and V. Lakshminaryanan) (CRC Press, London, 2007).

[DelMonte’06] F. Del Monte, Ó. Martínez-Matos, J. A. Rodrigo, M.L. Calvo and P. Cheben, *Adv. Mater.* **18**, 2014 (2006).

[Densmore’06] A. Densmore, D.-X. Xu, P. Waldron, S. Janz, P. Cheben, J. Lapointe, A. Delâge, B. Lamontagne, J. H. Schmid, and E. Post, *IEEE Phot. Technol. Lett.* **18**, 2520 (2006).

[Densmore’07] A. Densmore, D.-X. Xu, P. Waldron, S. Janz, P. Cheben, A. Delâge, P. Cheben and J. Lapointe, *Proc SPIE.* **6477**, 18 (2007).

[Dickey’03] Fred M. Dickey, *Opt. Photonics News* **14**, 30 (2003).

[Florjańczyk’12] M. Florjańczyk, C. Alonso-Ramos, P. Bock, A. Bogdanov, P. Cheben, I. Molina-Fernández, S. Janz, B. Lamontagne, A. Ortega-Moñux, and A. Scott, *Opt. Quant. Electron.* **44,** 549 (2012).

[Haw’03] M. D. Haw, M. Gillie and W. C. K. Poon, *Nature* **422**, 556 (2003).

[Jalali’07] B. Jalali, *Nat. Photonics* **1**, 193 (2007).

[Janz’04] S. Janz, A. Balakrishnan, S. Charbonneau, P. Cheben, M. Cloutier, A. Delâge, K. Dossou, L. Erickson, M. Gao, P.A. Krug, B. Lamontagne, M. Packirisamy, M. Pearson, and D.-X. Xu, I*EEE Photon. Technol. Lett.* **16**, 503 (2004).

[Kirchain’07] R. Kirchain and L. Kimerling, *Nat. Photonics* **1**, 303 (2007).

[Lockwood’10] D. J. Lockwood and L. Pavesi, *Silicon photonics II: components and integration* (Springer, Berlin, 2010).

[Mak’10] K. F. Mak, M. Y. Sfeir, J. A. Misewich and T. F. Heinz, *Proc. Natl. Acad. Sci. USA* **107**, 14999 (2010).

[Martínez’09] Ó. Martínez-Matos, J.A. Rodrigo, M. L. Calvo and P. Cheben, *Opt. Lett.* **34**, 485 (2009).

[Martínez’10] Ó. Martínez-Matos, J. A. Rodrigo, M. P. Hernández-Garay, J. G. Izquierdo, R. Weigand, M. L. Calvo, P. Cheben, P. Vaveliuk, and L. Bañares, *Opt. Lett.* **35**, 652 (2010).

[Nakajima’11] N. Nakajima, T. Liang, S. Ishida, Y. Tomioka, K. Kihou, C. H. Lee, A. Iyo, H. Eisaki, T. Kakeshita, T. Ito and S. Uchida, *Proc. Natl. Acad. Sci. USA* **108**, 12238 (2011).

[Novotny’97] L. Novtny, R. X. Bian and X. S. Xie, *Phys. Rev. Lett* **79**, 645 (1997).

[Ohno’06] F. Ohno, K. Sasaki, A. Motegi, and T. Baba, *Jpn. J. Appl. Phys.* **45**, 6126 (2006).

[Pearson’00] M. R. T. Pearson, A. Bezinger, A. Delâge, J. W. Fraser, S. Janz, P. E. Jessop, and D.-X. Xu, *Proc. SPIE* **3953**, 11 (2000).

[Predhel’12] K. Predehl, G. Grosche, S. M. F. Raupach, S. Droste, O. Terra, J. Alnis, Th. Legero, T. W. Hänsch, Th. Udem, R. Holzwarth and H. Schnatz, *Science* **336**, 441 (2012).

[Quintanilla’81] M. Quintanilla and A. M. de Frutos, *Appl. Opt.* **20**, 879 (1981).

[Rakuljic’93] G. A. Rakuljic and V. Leyva, *Opt. Lett.* **18**, 459 (1993).

[Reed’08] T. Reed, *Silicon photonics: the state of the art* (Wiley, Hoboken, 2008).

[Sakaguchi’11] J. Sakaguchi, Y. Awaji, N. Wada, A. Kanno, T. Kawanishi, T. Taru, T. Kobayashi and M. Watanabe, “109-Tb/s (7×97×172-Gb/s SDM/WDM/PDM) QPSK transmission through 16.8-km homogeneous multi-core fiber,” presented at *Optical Fiber Communication Conference*, Los Angeles (USA), June 2011.

[Schoen’93] C. L. Schoen, S. K. Sharma, C. E. Helsley and H. Owen, *Appl. Spectrosc.* **47**, 305 (1993).

[Schwartz’12] E. Schwartz, S. G. Lipson and E. N. Ribak, *Astron J.* **144**, 71 (2012).

[Xie’02] C. Xie, M. A. Dinno and Y. Li, *Opt. Lett.* **27**, 249 (2002).

[Wilken’12] T. Wilken, G. Lo Curto, R. A. Probst, T. Steinmetz, A. Manescau, L. Pasquini, J. I. González-Hernández, R. Rebolo, T. W. Hänsch, T. Udem and R. Holzwarth, *Nature* **485**, 611(2012).

[Yamauchi’08] J. Yamauchi, M. Yamanoue, and H. Nakano, *J. Lightwave Technol.* **26**, 1708 (2008).

[Yang’09] J. Yang, D. Hüvonen, U. Nagel, T. Room, N. Ni, P. C. Canfield, S. L. Bud’ko, J. P. Carbotte and T. Timusk, *Phys. Rev. Lett.* **102**, 187003 (2009).

Abstract: Photonic devices based on sol-gel and on silicon

INTRODUCTION AND OBJECTIVES

In the last decades, photonic devices have attracted a great deal of attention both within the scientific and business communities, due to their remarkable potential to solve ever increasing user's bandwidth demands, but also the society general desire to understand the world that surrounds us. Optical spectroscopy is an essential tool for understanding some of the largest-scale aspects of the universe [Albert'11, Wilken'12], such as exoplanet spectral analysis for biological signatures [Schwartz'12], but also the investigation on the behaviour of the smallest particles [Yang'09, Mak'10, Nakajima'11]. The capacity and length of optical links is continuously increasing [Predehl'12, Sakaguchi'11], and all-optical interconnects are shaping the future of communication networks and supercomputers [Alduino'07, Jalali'07]. Photonics have also proven essential for many other applications, such as biological and environmental sensors [Densemore'07], optical data storage [Haw'03], beam-shaping for lithography [Dickey'03], or optical trapping [Novotny'97], to name a few.

In this scenario, performance, efficiency and dimensional requirements of photonic devices are becoming extremely demanding. For this reason, the primary goal of the works presented in this thesis is the design, fabrication and characterization of highly efficient and competitive photonic devices for spectral and polarization handling. Two complementary photonic platforms have been used for this purpose, namely photopolymerizable holographic glasses and silicon-on-insulator, advantageously using the particular strengths derived from the way each of them enables the design of the spatial distribution of refractive index. Silicon-on-insulator has a very high refractive index contrast (*Δn* ~ 2) which allows implementing waveguides with highly confined optical modes and bend radii of a few mircometers, hence maximizing device integration. Photopolymerizable glasses have a lower refractive index contrast (*Δn* ~ 0.01), but enable to freely design and implement three-dimensional refractive index structures, resulting in diffractive photonic devices with a high diffraction efficiency and excellent optical quality.

Hybrid organic-inorganic photopolymerizable glasses [Cheben'01] are a class of holographic photomaterials typically synthesized with sol-gel techniques. They present a high refractive index modulation, optical quality, diffraction efficiency, sensitivity and structural stability [Calvo'06, Martínez'09, Martínez'10]. By incorporating zirconium-based High Refractive Index Species (HRIS) [DelMonte'06], refractive index modulation of Δn ~ 0.01 has been achieved. These features make photopolymerizable glasses an optimal candidate for holographic data storage [Haw'03]. However, the thickness of photopolymerizable glasses is typically less than ~200 μm, which limits their applicability to holographic filters [Barbastathis'99, Rakuljic'93, Quintanilla'81, Schoen'93]. The goals of this thesis work in sol-gel materials are the development of a novel formulation and synthesis technique of photopolymerizable glasses to overcome their thickness limitation, the implementation of notch filters that use the advantage of increased thickness for a narrower wavelength response, and the research of ionic liquid incorporation to the photopolymerizable glass components.

Silicon photonics [Reed'08, Lockwood'10], benefitting from a mass-scale cost-efficient fabrication and CMOS integration capabilities, have experienced a remarkable development in the last years. This development has been mainly driven by optical interconnects [Kirchain'07] and their promise of overcoming the bandwidth bottleneck of copper connections, but their application range encompasses diverse fields such as telecommunications [Zheng'10], astronomy [Florjańczyk'12], spectroscopy [Cheben'07a], biological and environmental sensing [Densemore'07] and others. In particular, the main goals of this thesis regarding silicon photonics is the development of compact and efficient passive devices such as spectrometers, filters, demultiplexers and polarization converters. The proposed devices are competitive alternatives to those known in the state of the art, such as polarization mode converters based on hybrid mode propagation [Yamauchi'08, Brooks'06] and demultiplexers and spectrometers based on AWGs (Arrayed Waveguide Gratings) [Cheben'07b, Pearson'00, Ohno'06] and waveguide *echelle* gratings [Janz'04, Bidnyk'06, Brouckaert'07].

CONTENT OF THE RESEARCH

In the framework of the described goals, the works of this doctoral thesis include the following fundamental contributions:

- A novel formulation and synthesis method of photopolymerizable glasses with high refractive index species have been developed, overcoming previous material thickness limitations. The new material allows to fabricate even and crack-free glass samples up to 500-µm thick. Photopolymerizable glasses synthesized with this technique have a high refractive index modulation and an excellent optical quality. They also show a high sensitivity, which allows the recording of efficient optical elements in a single-shot exposure with comparatively low recording power, while minimizing scattering.

- Highly spectrally selective holographic filters have been implemented in the photopolymerizable glasses with enhanced thickness. Notch filters with a bandwidth as low as 0.3 nm have been demonstrated with a maximum rejection ratio of -27.5 dB and a 0.1 dB ripple in the pass bands. The fabricated filters show an excellent optical quality and low scattering. Performance of these filters makes them ideal candidates, for example, for Rayleigh line suppression in Raman spectroscopy applications [Xie'02, Carrabba'90].

- The incorporation of ionic liquid to photopolymerizable glasses has been studied, in an effort to enhance the photopolymerization process. The effects of said incorporation, both in samples with and without HRIS, have been further characterized in terms of refractive index modulation, diffraction efficiency, optical quality, diffusion dynamics within the glass matrix, solution viscosity and scattering before and after the recording of holographic gratings.

- A novel integrated spectrometer configuration for the SOI platform has been experimentally demonstrated, in particular, a spatial heterodyne Fourier-transform spectrometer comprising an array of Mach-Zehnder interferometers with increasing optical path differences between the arms of each interferometer. This configuration results in a wavelength-dependent stationary output pattern from which the input spectrum is retrieved by computational techniques. Additionally, a spectral retrieval algorithm capable of compensating fabrication deviations without requiring active phase error compensation elements has been developed. By using tightly coiled silicon wire waveguide spirals, a spectral resolution of 40 pm has been demonstrated for a device footprint of only 12 mm^2.

- An ultracompact polarization mode converter has been designed, fabricated and characterized. The devices show a polarization mode conversion efficiency of 97.5% in a length as low as 10 µm. The mode converter is based on two asymmetrical trenches etched in a silicon wire waveguide, and was implemented in a single etching step by advantageously using the calibrated etch depth variations due to Reactive Ion Etching (RIE-lag) effect for small feature sizes (<100 nm).

- A curved-waveguide sidewall-grating multiplexer/demultiplexer has been demonstrated, with a crosstalk between adjacent channels of -25 dB. This value can be decreased down to -35dB by integrated a second consecutive diffraction grating, the lowest crosstalk reported for a microphotonic demultiplexer device. The footprint of the device is only 100 µm × 160 µm, significantly smaller than other alternatives devices such as AWGs of similar performance. Grating chirping and apodization allows to optimize coupling to output waveguides and minimize phase errors. Subwavelength index matching boundary is used to mitigate Fabry-Perot effects.

- Using the sidewall grating technology, a passband filter with two cascaded filtering stages has been designed, fabricated and characterized. An increased rejection ratio of the stop-bands of -40 dB is achieved in a device as small as 300 µm × 500 µm. The device shows a full-width at half-maximum bandwidth of 6.2 nm, with a roll-off of -4 dB/nm at the passband edges.

CONCLUSIONS

All the described results are integrated within the common goal of providing novel passive photonic devices with advanced performances for spectral and polarization handling. These devices can be applied to a wide range of fields, such as spectroscopy, astronomy, optical interconnects, telecommunications, and biological and environmental sensing, to name a few. The proposed devices, implemented in sol-gel photopolymerizable glasses and SOI, advantageously use the particular strengths of each respective platform in order to further advance the state of the art of diffractive and guided wave optics, with promising research and industrial application opportunities.

REFERENCES

[Albert'11] S. Albert, K. K. Albert, P. Lerch and M. Quack, *Faraday Discuss.* **150**, 71 (2011).

[Alduino'07] A. Alduino and M. Paniccia, *Nat. Photonics* **1**, 153 (2007).

[Barbastathis'99] G. Barbastathis, M.Balberg, and D. J. Brady, *Opt. Lett.* **24**, 811 (1999).

[Bidnyk'06] S. Bidnyk, D. Feng, A. Balakrishnan, M. Pearson, M. Gao, H. Liang, W. Qian, C.-C. Kung, J. Fong, J. Yin, and M. Asghari, *IEEE Photon. Technol. Lett.* **18**, 2392 (2006).

[Brooks'06] C. Brooks, P. E. Jessop, H. Deng, D. O. Yevick, and G. Tarr, *Opt. Eng.* 45, 044603 (2006).

[Brouckaert'07] J. Brouckaert, G. Roelkens, D. Van Thourout and R. Baets, *Phot. Tech. Lett.* **19**, 1484 (2007).

[Calvo'06] M. L. Calvo, P. Cheben, Ó. Martínez-Matos, F. del Monte, and J. A. Rodrigo, *Phys. Rev. Lett.* **97**, 084801 (2006).

[Carrabba'90] M. M. Carrabba, K. M. Spencer, C. Rich and D. Rauh, *Appl. Spectrosc.* **44**, 1558 (1990).

[Cheben'01] P. Cheben and M.L. Calvo, *Appl. Phys. Lett.* **78**, 1490 (2001).

[Cheben'07a] P. Cheben, J. H. Schmid, A. Delâge, A. Densmore, S. Janz, B. Lamontagne, J. Lapointe, E. Post, P. Waldron, and D.-X. Xu, *Opt. Express* **15**, 2299 (2007).

[Cheben'07b] P. Cheben, "Wavelength dispersive planar waveguide devices: Echelle gratings and arrayed waveguide gratings," in *Optical Waveguides: From Theory to Applied Technologies* (eds. M. L. Calvo and V. Lakshminaryanan) (CRC Press, London, 2007).

[DelMonte'06] F. Del Monte, Ó. Martínez-Matos, J. A. Rodrigo, M.L. Calvo and P. Cheben, *Adv. Mater.* **18**, 2014 (2006).

[Densmore'06] A. Densmore, D.-X. Xu, P. Waldron, S. Janz, P. Cheben, J. Lapointe, A. Delâge, B. Lamontagne, J. H. Schmid, and E. Post, *IEEE Phot. Technol. Lett.* **18**, 2520 (2006).

[Densmore'07] A. Densmore, D.-X. Xu, P. Waldron, S. Janz, P. Cheben, A. Delâge, P. Cheben and J. Lapointe, *Proc SPIE.* **6477**, 18 (2007).

[Dickey'03] Fred M. Dickey, *Opt. Photonics News* **14**, 30 (2003).

[Florjańczyk'12] M. Florjańczyk, C. Alonso-Ramos, P. Bock, A. Bogdanov, P. Cheben, I. Molina-Fernández, S. Janz, B. Lamontagne, A. Ortega-Moñux, and A. Scott, *Opt. Quant. Electron.* **44,** 549 (2012).

[Haw'03] M. D. Haw, M. Gillie and W. C. K. Poon, *Nature* **422**, 556 (2003).

[Jalali'07] B. Jalali, *Nat. Photonics* **1**, 193 (2007).

[Janz'04] S. Janz, A. Balakrishnan, S. Charbonneau, P. Cheben, M. Cloutier, A. Delâge, K. Dossou, L. Erickson, M. Gao, P.A. Krug, B. Lamontagne, M. Packirisamy, M. Pearson, and D.-X. Xu, I*EEE Photon. Technol. Lett.* **16**, 503 (2004).

[Kirchain'07] R. Kirchain and L. Kimerling, *Nat. Photonics* **1**, 303 (2007).

[Lockwood'10] D. J. Lockwood and L. Pavesi, *Silicon photonics II: components and integration* (Springer, Berlin, 2010).

[Mak'10] K. F. Mak, M. Y. Sfeir, J. A. Misewich and T. F. Heinz, *Proc. Natl. Acad. Sci. USA* **107**, 14999 (2010).

[Martínez'09] Ó. Martínez-Matos, J.A. Rodrigo, M. L. Calvo and P. Cheben, *Opt. Lett.* **34**, 485 (2009).

[Martínez'10] Ó. Martínez-Matos, J. A. Rodrigo, M. P. Hernández-Garay, J. G. Izquierdo, R. Weigand, M. L. Calvo, P. Cheben, P. Vaveliuk, and L. Bañares, *Opt. Lett.* **35**, 652 (2010).

[Nakajima'11] N. Nakajima, T. Liang, S. Ishida, Y. Tomioka, K. Kihou, C. H. Lee, A. Iyo, H. Eisaki, T. Kakeshita, T. Ito and S. Uchida, *Proc. Natl. Acad. Sci. USA* **108**, 12238 (2011).

[Novotny'97] L. Novtny, R. X. Bian and X. S. Xie, *Phys. Rev. Lett* **79**, 645 (1997).

[Ohno'06] F. Ohno, K. Sasaki, A. Motegi, and T. Baba, *Jpn. J. Appl. Phys.* **45**, 6126 (2006).

[Pearson'00] M. R. T. Pearson, A. Bezinger, A. Delâge, J. W. Fraser, S. Janz, P. E. Jessop, and D.-X. Xu, *Proc. SPIE* **3953**, 11 (2000).

[Predhel'12] K. Predehl, G. Grosche, S. M. F. Raupach, S. Droste, O. Terra, J. Alnis, Th. Legero, T. W. Hänsch, Th. Udem, R. Holzwarth and H. Schnatz, *Science* **336**, 441 (2012).

[Quintanilla'81] M. Quintanilla and A. M. de Frutos, *Appl. Opt.* **20**, 879 (1981).

[Rakuljic'93] G. A. Rakuljic and V. Leyva, *Opt. Lett.* **18**, 459 (1993).

[Reed'08] T. Reed, *Silicon photonics: the state of the art* (Wiley, Hoboken, 2008).

[Sakaguchi'11] J. Sakaguchi, Y. Awaji, N. Wada, A. Kanno, T. Kawanishi, T. Taru, T. Kobayashi and M. Watanabe, "109-Tb/s (7×97×172-Gb/s SDM/WDM/PDM) QPSK transmission through 16.8-km homogeneous multi-core fiber," presented at *Optical Fiber Communication Conference*, Los Angeles (USA), June 2011.

[Schoen'93] C. L. Schoen, S. K. Sharma, C. E. Helsley and H. Owen, *Appl. Spectrosc.* **47**, 305 (1993).

[Schwartz'12] E. Schwartz, S. G. Lipson and E. N. Ribak, *Astron J.* **144**, 71 (2012).

[Xie'02] C. Xie, M. A. Dinno and Y. Li, *Opt. Lett.* **27**, 249 (2002).

[Wilken'12] T. Wilken, G. Lo Curto, R. A. Probst, T. Steinmetz, A. Manescau, L. Pasquini, J. I. González-Hernández, R. Rebolo, T. W. Hänsch, T. Udem and R. Holzwarth, *Nature* **485**, 611(2012).

[Yamauchi'08] J. Yamauchi, M. Yamanoue, and H. Nakano, *J. Lightwave Technol.* **26**, 1708 (2008).

[Yang'09] J. Yang, D. Hüvonen, U. Nagel, T. Room, N. Ni, P. C. Canfield, S. L. Bud'ko, J. P. Carbotte and T. Timusk, *Phys. Rev. Lett.* **102**, 187003 (2009).

I

General introduction

1.1. Current challenges in photonics

Due to its remarkable ability to analyze and manipulate light, and to the impressive advances in micro and nano-fabrication technologies, photonics have become a fundamental part of diverse research fields such as astronomy, communications or biochemistry, just to name a few [Bland'12, Soref'10]. Furthermore, recent advances in the industrialization of the fabrication processes of photonic devices, which advantageously use industrial infrastructures developed for micro-electronics, are bringing them ever closer to our everyday life, including data interconnects, biological and environmental sensors, hand-held spectrometers, and many others.

As an example, optical spectroscopy has been a canonical technology for over a century [Michelson'87] for shedding light both on the fundamental properties of the smallest particles [Yang'09, Mak'10, Nakajima'11] and the largest-scale aspects of the universe [Albert'11b, Schwartz'12, Wilken'12]. At the same time, optical fiber networks have become the principal communication arteries of our world, providing remarkable precision even in the longest distances [Predehl'12] and bringing an unprecedented speed to our data connections [Sakaguchi'11], Fang'10]. As the optical network is getting closer to our homes literally every day, new efficient all-optical interconnects [Alduino'07, Jalali'07] are shaping the future of data communications.

In the present scenario, photonic devices with demanding specifications are constantly being sought. Scientists and product developers seek to build spectrometers with better resolutions and demultiplexers with lower crosstalk, to manipulate light in small footprints and yet obtain high-quality performances. Furthermore, low-cost and sustainable device fabrication are required in order to apply photonics both to innovative research and to our everyday life.

The studies included in the present doctoral thesis aim precisely towards these goals: developing compact high-quality photonic devices capable of manipulating light in an efficient manner, and specifically its spectrum and polarization properties. For this purpose, two different but complementary platforms for the development of photonic devices are studied, namely holographic photomaterials based on hybrid organic-inorganic sol-gel glasses and integrated optics based on silicon-on-insulator (SOI) waveguide platform.

At their core, both platforms are based on the design of optical structures by locally modifying the refractive index of the medium, while the way this refractive index difference is achieved determines the particular strengths of each platform. In the case of silicon photonics, optical waveguides are created by selectively etching a planar silicon wafer. The subsequent high refractive index contrast between the silicon waveguides and the insulator SiO_2 cladding ($\Delta n \sim 2$) allows a high confinement of the guided optical modes and a dense waveguide integration, but the design freedom is limited to a single waveguide plane and conditioned by the etching technologies, typically limited to a few (often single) etch depths unless complex fabrication methods are employed. On the contrary, holographic media present a homogeneous refractive index distribution, which is altered by exposure to actinic light to achieve the desired patterns. This process generates a comparatively low refractive index modulation ($\Delta n \sim 0.01$), but in exchange, allows three-dimensional design of the refractive index patterns. The benefits of each platform (high mode in-plane confinement versus three-dimensional design) can be advantageously used in a wide range of waveguide and diffractive optical devices and applications.

Our starting point for holographic photonic devices are photopolymerizable glasses [Cheben’01, DelMonte’06]. Its high refractive index modulation allows to record, permanently and with high efficiency, three-dimensional refractive index distributions, following their exposure to an interference pattern of a specific wavelength. This enables to record both the amplitude and the phase of incident light, and provides an additional degree of freedom in the design of optical elements, compared to planar waveguide photonic circuits. For example, the three-dimensional refractive index modulation has been advantageously used in high-density holographic data storage systems [Haw’03, Psaltis’95, Mok’00, Solymar’81, Wilson’10]. Unlike conventional data recording media, holographic photomaterials enable superposed (multiplexed) recording of data blocks [Mok'93] as well as a simultaneous page-oriented readout. These features result in a greatly increased storage capacity and readout speed.

Holographic optical elements (HOE) have been used in a wide range of applications, for example modeling of pulsed and continuous laser sources [Brady'92, Hill'93], deformation measurement through interferometric techniques [Vest'79], microscopy [Barbastathis'99], identification of chemical compounds through spectral signature [Cao'09] and recognition of visual patterns [Fujii'80, Fleisher'90].

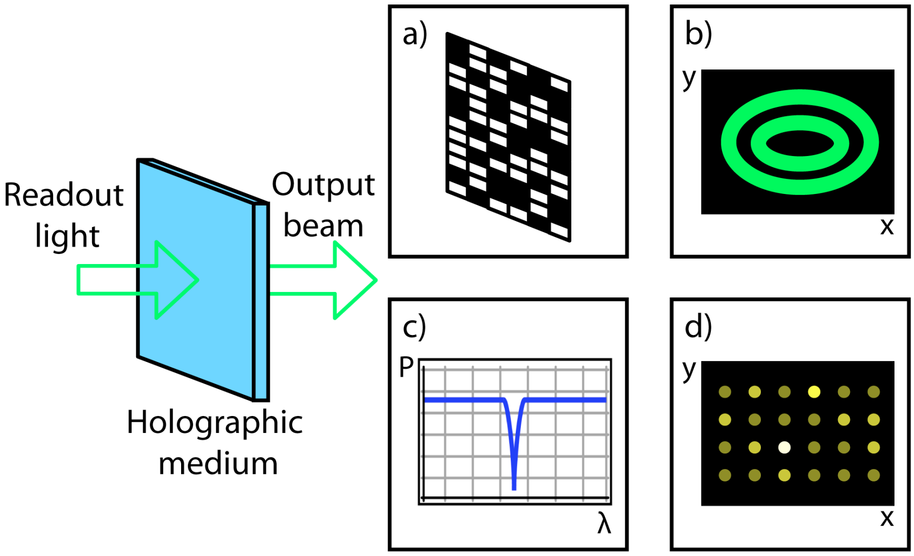

Figure 1.1. *Examples of photonic devices implemented in holographic photomaterials.* ***a)*** *Holographic data storage [Haw'03]: a collimated light source reconstructs a spatial light distribution corresponding to a previously recorded data block.* ***b)*** *Beam shaping [Brady'92]: the spatial power distribution of the input beam is transformed to generate a specific optical mode.* ***c)*** *Holographic notch filter [Xie'02]: a narrow wavelength range is blocked and removed from the spectral distribution of the output beam.* ***d)*** *Visual pattern recognition [Fleisher'90]: a plurality of matched filters, previously multiplexed in the holographic medium, generate an array of outputs corresponding to the correlation of the input signal with each of the matched filters.*

The performance of these holographic devices greatly depends on the holographic medium in which they are implemented. In particular, one of the most promising and versatile platforms for the development of holographic devices are photopolymerizable glasses incorporating high refractive index species and synthesized with sol-gel techniques [DelMonte'06]. Photopolymerizable glasses have already demonstrated remarkable performance in terms of refractive index modulation, diffraction efficiency, spatial resolution, sensitivity, optical quality, and structural stability [DelMonte'06, Calvo’06, Martínez’09, Martínez’10]. However, material thickness was previously limited to about 200 µm, restricting its potential for holographic spectral filtering.

Based on this photomaterial, we explore different modifications to its formulation and synthesis process in order to enable the implementation of photonic devices in holographic samples with enhanced thickness. In particular, we aim towards the development of high-quality narrow notch filters for applications such as Rayleigh line suppression in Raman spectroscopy [Xie’02, Carrabba’90, Pelletier’91].

On the other hand, the fabrication techniques of the silicon-on-insulator (SOI) platform have already reached a stage of maturity, mainly because of SOI applications in CMOS microelectronics. Despite requiring integration with other materials such as germanium for implementing active elements (light sources, modulators and photodetectors), SOI provides high refractive index contrast, low-cost fabrication at mass-scale and integration with CMOS electronics, making this platform an ideal candidate for low-cost compact optoelectronic devices with high optical performances.

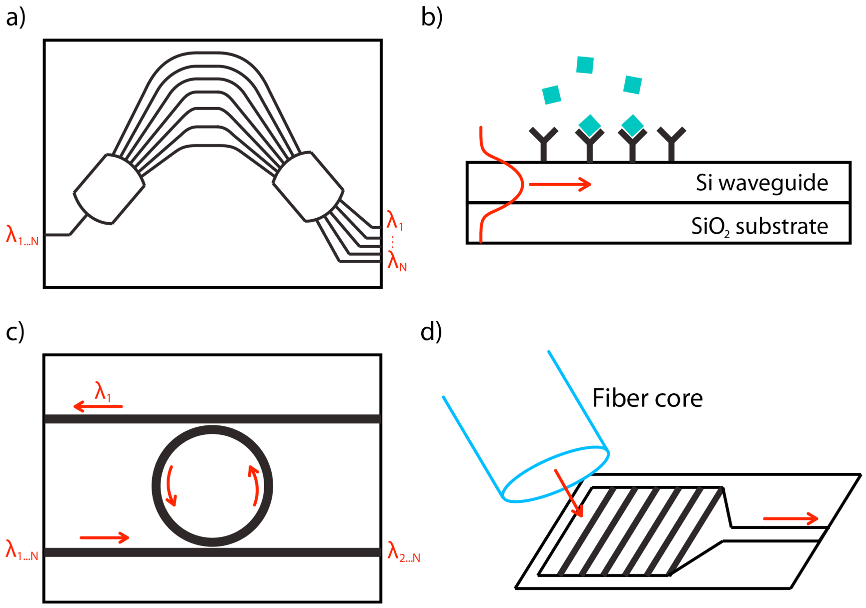

***Figure 1.2.** Application examples of silicon-on-insulator photonic devices. **a)** Optical interconnects [Kirchain’07]: a wavelength dispersive element separates input light into a plurality of output channels. **b)** Biological sensors [Densmore’07]: the presence of biological molecules in proximity of the waveguide surface modifies the propagation characteristics of the guided modes, and therefore, the transmittance of the device, **c)** Integrated filters [Madsen’98]: a single channel is coupled to a ring resonator and extracted from the input signal. **d)** Fiber-to-chip couplers [Halir’10]: a diffraction grating receives the optical mode transmitted by the optical fiber core and couples it into a silicon wire waveguide.*

Recent advances in silicon photonics include the development of diverse photonic structures including multiplexers/demultiplexers [Cheben‘07b, Doerr’06], filters and resonators [Madsen’98], couplers [Cheben’10, Halir’10], polarization mode converters [Vermeulen’10, Zhang’10], splitters [Fukuda’06], buffers [Xia’07], photodetectors [Feng’09], modulators [Liu‘08a] and interferometers [Zhao’95]. These structures can be used as building blocks to integrate more complex photonic devices, such as optical interconnects [Kirchain’07], spectrometers [Cheben‘07a], and biological and environmental sensors [Densmore’07]. Furthermore, due to the high refractive index contrast of the SOI platform, all these devices can be implemented with densely integrated waveguide structures in very compact footprints.

However, in order to develop silicon-based photonic devices that can be competitive at a large market scale, issues like optical performance, integration capacity, and robustness against fabrication imperfections are of critical importance. Ee take advantage of the high-precision fabrication techniques perfected at the facilities of the National Research Council of Canada (NRC), and seek to design advanced polarization converters, spectrometers, demultiplexers and filters, with high quality optical performance and ultracompact footprints.

By advantageously using the particular strengths of the two photonic platforms (sol-gel photopolymerizable glasses and SOI), this thesis presents an original proposal for the analysis, design, synthesis and characterization of highly competitive photonic elements that represent significant milestones towards building new generations of efficient optical devices that can be used in diverse applications such as spectroscopy, communications, air-borne sensing, and biological and environmental analysis.

1.2. Document organization

This thesis is organized as follows. In Chapter II, the fundamentals of volume holography are reviewed. State-of-the art holographic photomaterials are discussed, focusing on photopolymerizable glasses and specifically on the technical challenges that were overcome by the present work in order to develop narrowband spectral filters.

Chapter III is devoted to introducing silicon photonics and its potential for the development of integrated photonic components such as polarization converters, demultiplexers, spectrometers, and passband filters.

Chapter IV presents the scientific publications containing the thesis results regarding the development of holographic filters in photopolymerizable glasses with enhanced thickness, as well as a comparative study regarding the incorporation of ionic liquid to the synthesis of this photomaterial.

In Chapter V the silicon-based photonic components which were designed, fabricated and characterized during the studies of the present thesis are presented through the scientific publications in which they have been reported. These devices include compact polarization rotators, sidewall grating demultiplexers and passband filters, and Fourier-transform spatial heterodyne spectrometer chips.

Chapter VI contains the general conclusions obtained from this work.

Annex A details the experimental methods used in this research, including the synthesis, recording and characterization of photopolymerizable glasses, and the design, fabrication and characterization techniques of the devices implemented in SOI.

Finally, the document incorporates the list of references and abbreviation, as well as the publications that the presented studies have generated.

II

Introduction to photonic devices based on sol-gel photopolymerizable glasses

Photopolymerizable glasses have proven to be a versatile and efficient material for holographic applications. In this chapter, the synthesis and recording mechanisms of this kind of photomaterial are described, as well as the challenges posed by its application to narrowband holographic filters. The fundamentals of volume holography are also discussed.

2.1. Theoretical framework of volume holography

Optical holography is based on the recording in a photosensitive material of a three-dimensional interferogram created by two mutually coherent light beams [Gabor'48, Collier'71, Caulfield'79, Hariharan'87, Leiths'92]. After exposure to the light modulation of the interferogram, the photomaterial undergoes a series of physical, chemical or physicochemical changes that modify the spatial distributions of the refractive index and/or the extinction coefficient of the medium in response to the interference pattern. This results in the recording of a holographic diffraction grating that comprises the complex field information (phase and amplitude) of the recording light beams. Said recording is either permanent (WORM photomaterials, Write Once Read Many) [Mok'93, Cheben'96] or erasable with light exposure to the appropriate wavelengths [Berg'96].

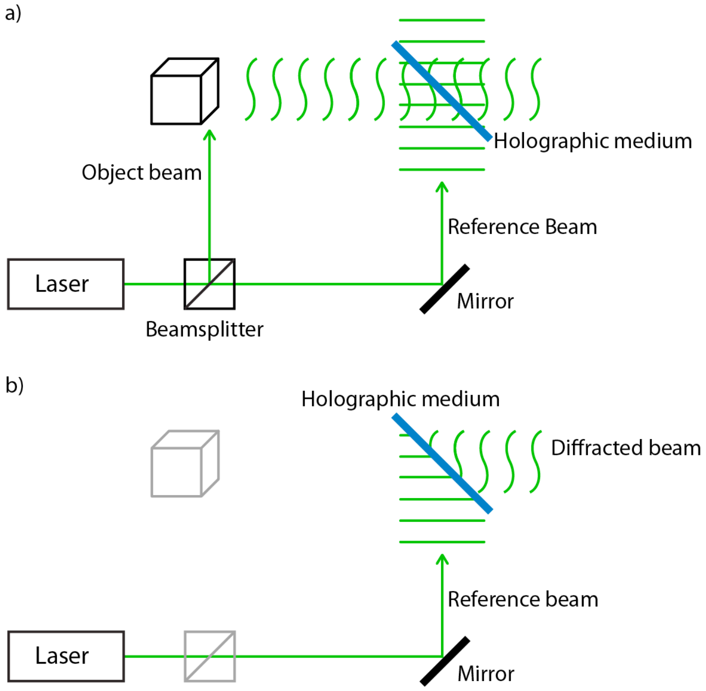

Figure 2.1. a) *Recording of a transmission hologram by interference of two mutually coherent light beams.* ***b)*** *Readout of the recorded hologram.*

In a typical holographic application, one recording beam is an object beam which contains the information to be processed, whereas the other beam is a reference beam (originating from the same coherent light source) with a predetermined phase and amplitude, typically a collimated beam. After recording, if the hologram is illuminated with the reference beam, the diffraction by the grating generates a holographic replica of the original object beam at the output of the holographic medium. This process is depicted in figure 2.1.

Depending on the geometry of recording configuration, transmission or reflection holograms are formed. In a transmission hologram (fig. 2.2.a), the two recording beams are incident on the same side of the sample. Therefore, readout beams are diffracted by the hologram towards the opposite side. In a reflection hologram (fig. 2.2.b), the recording beams are incident contra-directionally from opposite sides of the holographic medium, and hence the readout beam is diffracted back towards the same side it is incident on the sample.

A simple Holographic Optical Element (HOE) that allows us to characterize a holographic photomaterial is a volume phase holographic grating (VPHG) with a periodic refractive index modulation and no spatial variation of the medium absorbance. This configuration results from the interference of two collimated mutually coherent light beams, as shown in figure 2.2.

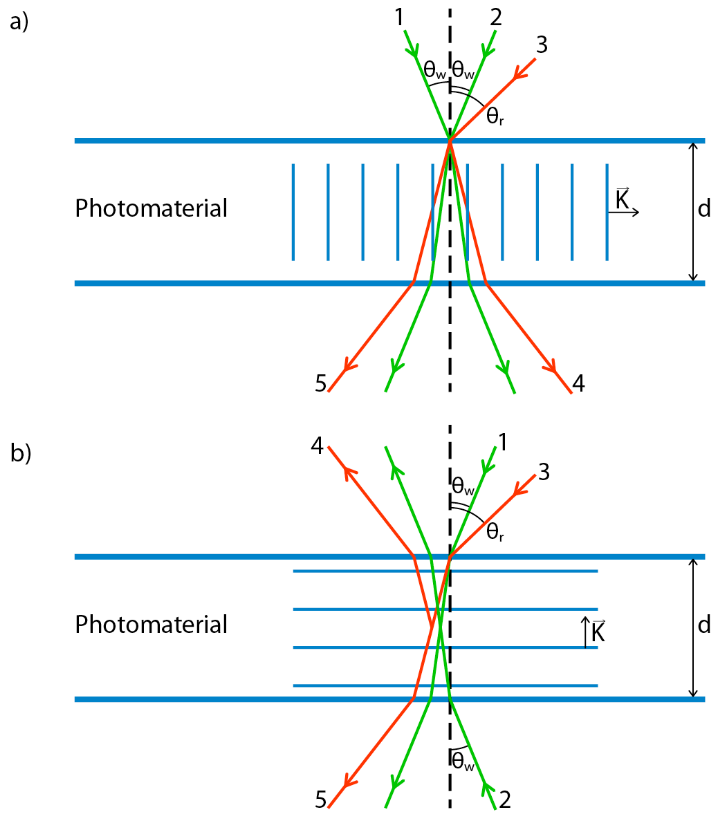

Figure 2.2. a) *Transmission hologram recording and readout of a plane transmission volume diffraction grating with grating vector* $\vec{K}$ *by interference of recording beams 1 and 2, incident with angles* θ_w *and* $-\theta_w$ *in a photomaterial of thickness d. Readout is performed by incidence of beam 3 at an angle* θ_r*, which is diffracted by the grating and generates beams 4 (-1st diffraction order) and 5 (transmitted beam or 0th diffraction order).* ***b)*** *Holographic recording and readout of a plane volume reflection diffraction grating.*

Diffraction gratings can operate in two different regimes: volume regime (Bragg) and thin grating regime (Raman-Nath) [Magnusson'78, Gaylord'81]. Volume gratings present a single diffracted beam, whereas thin gratings generate multiple diffraction orders. In order to determine if a periodic holographic grating operates in a volume (Bragg) diffraction regime, the *Q* parameter is used. The following condition was introduced in 1936 by Extermann *et al.* [Extermann'36], with Q>10 corresponding volume regimes:

$$Q = \frac{2\pi\lambda d}{\sqrt{\varepsilon_1}\Lambda^2} \tag{2.1}$$

where λ is the wavelength, d is the thickness of the grating, ε_1 is the average relative dielectric permittivity of the medium, and Λ is the grating period. We define the grating vector $\vec{K}$ as:

$$\left|\vec{K}\right|^2 = \left(\frac{2\pi}{\Lambda}\right)^2 \tag{2.2}$$

and the propagation constant β as the modulus of the propagation vector of a light beam of wavelength λ in a medium of average refractive index n:

$$\beta = \frac{2\pi n}{\lambda} \tag{2.3}$$

The Q parameter can be hence expressed as:

$$Q = \frac{\left|\vec{K}\right|^2 d}{\beta} \tag{2.4}$$

In order to characterize the response of a plane VPHG, its diffraction efficiency is typically measured as:

$$\eta = \frac{P_{-1}}{P_0 + P_{-1}} \tag{2.5}$$

where P_0 and P_{-1} are the optical power of the transmitted and *-1st* diffracted order respectively. This definition of diffraction efficiency assumes negligible absorption losses in which incident power P_{in} is diffracted into the zero and *-1st* diffracted order. A more detailed analysis including the losses yields:

$$P_0 + P_{-1} = \frac{e^{-\alpha d}}{L_r \cdot L_p \cdot L_s} P_{in} \tag{2.6}$$

where α is the medium absorbance and L_r, L_p and L_s are the losses associated with reflections in the photomaterial input and output interfaces, depolarization of incident light, and scattering, respectively. In a photopolymerizable glass with refractive index of ~1.5, Fresnel losses at each interface reduce around 4% of the incident power, whereas their excellent optical quality and transparency make absorption and scattering losses negligible.

In order to characterize a plane VPHG, the angular dependence of its diffraction efficiency is typically studied, also known as angular selectivity curve. Holographic grating formation theory can be framed within the dynamic theory of diffraction [Batterman'64]. Kogelnik's two coupled waves theory [Kogelnik'69], is a first-order scalar approximation to said formulation, and determines the relation between the wave vectors of the incident beam ($\vec{k}_i$) and the diffracted beam ($\vec{k}_d$) as a function of the grating vector $\vec{K}$:

$$\vec{k}_3 + \vec{K} = \vec{k}_4 \tag{2.7}$$

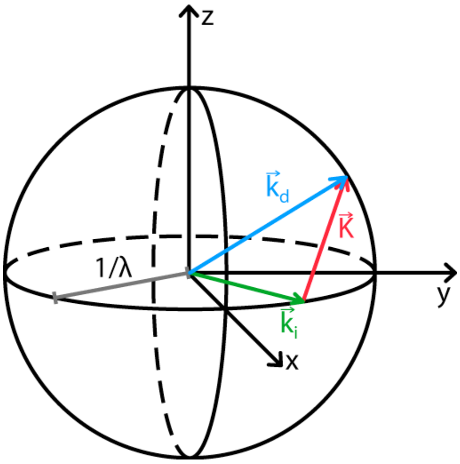

Figure 2.3. *Ewald sphere showing the relation between the grating vector $\vec{K}$ and the incident ($\vec{k}_i$) an diffracted beam ($\vec{k}_d$).*

Following Kogelnik's theory, we consider a one-dimensional scalar model for the electric permittivity of a grating with no absorption. The electric permitivity ε_r therefore depends of position vector $\vec{r}$ according to:

$$\varepsilon_r(\vec{r}) = \varepsilon_1 + \varepsilon_2 \cos(\vec{K} \cdot \vec{r}) \tag{2.8}$$

where ε_1 is the average relative dielectric constant of the medium and ε_2 is the phase modulation of the grating. The modulation of the electric permittivity corresponds to a refractive index modulation Δn, defined as the difference between the maximum (n_{max}) and minimum (n_{min}) refractive indexes of the diffraction grating:

$$\Delta n = n_{\max} - n_{\min} = \sqrt{\mu_r}\left(\sqrt{\varepsilon_{r_0} - \varepsilon_{r_1}} - \sqrt{\varepsilon_{r_0} + \varepsilon_{r_1}}\right) \tag{2.9}$$

where μ_r is the relative magnetic permeability of the medium, and ε_0 and μ_0 are the vacuum electric permittivity and magnetic permeability, respectively.

We consider the propagation inside the holographic medium of two waves, incident wave ψ_i and first order diffracted wave ψ_d, defined as:

$$\psi_i = R(x)\exp[-i\beta(x\cos\theta_i + y\sin\theta_i)] \tag{2.10}$$

$$\psi_d = S(x)\exp[-i\beta(x\cos\theta_d + y\sin\theta_d)] \tag{2.11}$$

where *R(x)* and *S(x)* are the wave amplitudes of ψ_i and ψ_d; and θ_i and θ_d are the propagation angles of ψ_i and ψ_d inside the holographic medium. The resulting wave differential equation is:

$$\nabla^2 E + \beta^2\left[1 + \frac{\varepsilon_{r_1}}{\varepsilon_{r_0}}\cos\beta(p_1 - p_2)\right]E = 0 \tag{2.12}$$

with:

$$p_1 = x\cos\theta_i + y\sin\theta_i \tag{2.13}$$

$$p_2 = x\cos\theta_d + y\sin\theta_d \tag{2.14}$$

where θ_i and θ_d are related to the grating vector according to Eq. 2.7. By applying the first order approximation, phase terms are negligible:

$$\exp(-2i\beta p_1) \approx \exp(-2i\beta p_2) \approx 1 \tag{2.13}$$

Furthermore, considering that amplitudes *R(x)* and *S(x)* vary slowly along the medium, with a low coupling between the two signals, second derivative terms are also negligible. With these described approximations, the following solution to Eq 2.12 is obtained for the grating diffraction efficiency angular dependence:

$$\eta(\theta_i) = \frac{\sin^2\sqrt{\chi^2(\theta_i) + \phi^2}}{1 + \dfrac{\chi^2(\theta_i)}{\phi^2}} \tag{2.16}$$

with:

$$\chi(\theta_i) = (\theta_i - \theta_B)\frac{2\pi n d}{\lambda}\sin\theta_B \tag{2.17}$$

$$\phi = \frac{\pi \Delta n d}{\lambda \cos\theta_B} \tag{2.18}$$

where θ_B is Bragg's angle, which is the angle of the incident beam at which diffraction efficiency is maximized.

$$\sin(\theta_B) = \frac{\lambda}{2\Lambda} \tag{2.19}$$

From Eqs. 2.16 and 2.17, the maximum diffraction efficiency of the VPHG is found as a function of the refractive index modulation. A periodic variation of the maximum diffraction efficiency with Δn is observed. When the refractive index modulation surpasses the first maximum (100% diffraction efficiency), the grating becomes overmodulated.

$$\eta_{\max} = \eta(\theta_B) = \sin^2\left(\frac{\pi d \Delta n}{\lambda \cos\theta_B}\right) \tag{2.20}$$

For a plane diffraction grating with unknown thickness and refractive index modulation, both parameters can be determined by measuring the angular dependence of diffraction efficiency near Bragg's angle, and fitting this angular selectivity curve to its theoretical expression given by Eq. 2.16. Notice that the Full-Width at Half-Maximum (FWHM) of the diffraction efficiency curve is inversely proportional to the grating thickness and to its spatial frequency. Furthermore, a higher sidelobe level is typically present in overmodulated regimes.

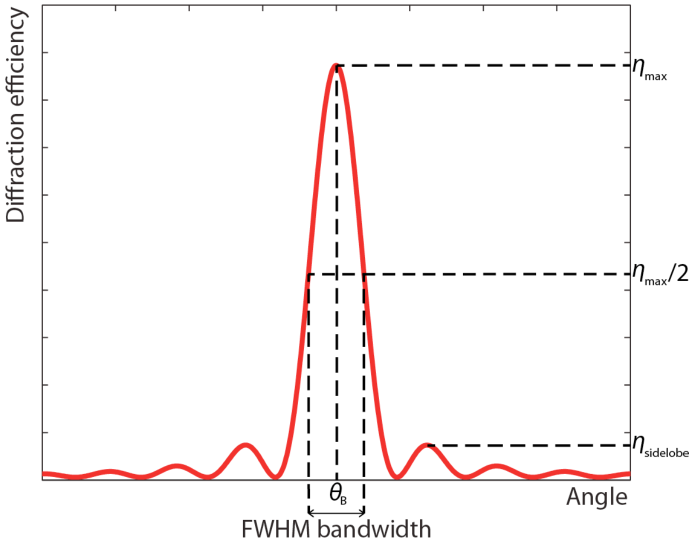

Figure 2.4. *Diffraction efficiency near Bragg's angle for a volume holographic diffraction grating.*

2.2. Holographic photomaterials

VPHGs can be adapted for specific holographic applications by a judicious design of the object and reference beams. For example, holographic data storage systems [Haw'03, Psaltis'95, Mok'00, Solymar'81, Wilson'10] rely on encoding the object beam with spatially distributed binary data. The three-dimensional refractive index modulation of holographic photomaterials enables multiplexing of data blocks [Mok'93], further increasing the system capacity. Other adapted designs of the object beam enable diverse holographic applications such as laser pulse modeling [Brady'92, Hill'93], interferometric deformation measurement [Vest'79], or optical filtering [Schoen'93].

In most holographic photomaterials based upon amorphous materials the recorded interference patterns are permanent once the recording process is finalized. Such materials can be applied to the so-called Write Once Read Many (WORM) memories. However, there have also been advances in rewritable holographic materials for optical storage [Luo'05] and for telepresence systems [Blanche'10], mostly based upon photorefractive media.

Regardless of the specific application in mind, materials need to meet several requirements in order to implement high-quality Holographic Optic Elements (HOE) [Calvo'08, Calvo'09]. A high photosensitivity enables short recording times and low recording energies, which also reduces the stability requirements of the setup and broadens the range of laser sources that can be used. A high refractive index modulation and dynamic range allows reaching diffraction efficiencies close to 100% and benefits storage and multiplexing capacity. As in any optical element, a high optical quality is required, and subsequently, high transparency and low scattering to minimize losses and noise build-up in the signal. Finally, a high structural and thermal stability is desired to avoid distortions of the recorded holograms.

Another factor to be considered when choosing a holographic photomaterial is post-processing. In some cases, after the finalization of the actinic exposure and the formation of the refractive index profile inside the holographic photomaterial, additional physical or chemical processes are required to render this distribution permanent. For example, development and fixing steps are required in silver halide materials [Bjelkhagen'95]. For photorefractive materials such as Lithium or Potassium niobates [Mok'93, Montemezzani'90], a thermal treatment with temperatures over 100ºC is required to fix the refractive index modulation to the holographic medium. Typically, faster and less aggressive methods are desirable in order to reduce strains induced to the photomaterial and to simplify the hologram recording process. The performance of several types of holographic photomaterials is presented in table 2.1, showing the wavelength range that can be used for the holographic recording, the maximum reported refractive index modulation, the usual thickness range, and the required curing process.

	Sensitive λ (nm)	**Δn**	**Thickness (mm)**
Dichromate gelatine [Shanktoff'68]	< 540	10^{-2}	0.1-0.6
Potassium niobate [Montemezzani'90]	400 - 600	10^{-4}	1 - 10
Dupont HRF-150 [Smothers'90]	500 - 550	2.8×10^{-3}	0.038
Lithium niobate [Mok'93]	400 - 600	3×10^{-3}	1 - 20
Photorefractive polymers [Meerholz'94, Zhang'04]	480 - 830	10^{-2}	0.01 – 0.05
Polaroid CROP photopolymer [Curtis'94]	480 - 540	5×10^{-3}	0.2 – 0.5
Photopolymer-filled nanoporous Vycor Glass [Schnoes'99]	480 - 540	10^{-5}	1.5
Silver halide gelatin [Neipp'99]	580-630	5×10^{-2}	2
Silica Gel methyl methacrylate organically modified ceramic [Cheben'96]	300-400	1.1×10^{-4}	0.2
Lucent acrylate [Colvin'00]	500 - 532	9×10^{-3}	1
TiO_2 nanoparticle–photopolymer composites [Sánchez'05]	300 - 400	1.5×10^{-2}	0.01
Highly transparent ZrO_2 nanoparticle-dispersed acrylate polymers [Suzuki'06]	300-400	5×10^{-3}	0.02-0.05

Table 2.1. *Properties of selected holographic materials.*

Among many of available holographic photomaterials, photopolymerizable materials have shown a excellent performance in terms of refractive index modulation and optical quality [Sincerbox'94, Lessard'95, Coufal'00]. These holographic media comprise a monomeric species whose polymerization is selectively triggered by a sensitizer or photoinitiator after exposure to a light interference pattern of the appropriate wavelength. The photon energy transfer from the actinic light to the sensitizer results in the generation of free radicals that inititates a chain process of polymerization [Calvo'08]. As a consequence of this process, a single photon may trigger the polymerization of thousands of monomer molecules, reducing the optical power required to record the diffraction gratings.

The photopolymerization process results in high sensitivity and refractive index modulation, but also presents a challenge in terms of dimensional stability. Due to the conversion of the monomeric species into polymeric chains, the volume of the holographic medium is reduced after light exposure. This shrinkage compromises the data storage capability of some photopolymerizable materials, and can distort the recorded holograms.

2.2.1 Green holography

One of the current challenges in photomaterial research is the development of sustainable fabrication processes in which the use of toxic and hazardous substances is avoided or at least limited. Conventional holographic materials typically comprise highly volatile toxic substances, such as acrylamide (AA) based photopolymerizable monomeric species. These substances can be liberated during the photomaterial synthesis, generating a health hazard for workers when manufacturing in bulk. Furthermore, their toxicity can surpass the life cycle of the implemented holographic optical elements, damaging the environment if the residues are not dealt with appropriately.

Recently, some efforts have been made towards developing environmental-friendly holographic photopolymers [Ortuño’07, Cody’12], achieving refractive index modulations in the order of more toxic photomaterials such as AA-based photopolymers ($\Delta n \sim 10^{-3}$). In particular, a sodium salt (5’-riboflavin monophospate) has been proposed as a dye to substitute the photoinitiator, whereas AA monomers are replaced by a less toxic monomeric species based on sodium acrylate [Ortuño’07]. 1-mm-thick samples were fabricated, with maximum diffraction efficiencies in the range of 75%.

A low-toxicity diacetone acrylamide-based photopolymer has also been proposed as an alternative, further incorporating glycerol to increase the maximum refractive index modulation [Cody’12]. Refractive index modulations up to $\Delta n = 2.2 \times 10^{-3}$ were achieved in 100-µm-thick samples. Recorded gratings presented a spatial frequency of 1000 lines/mm and a maximum diffraction efficiency of 90%.

2.3. Photopolymerizable glasses

Photopolymerizable glasses are a subgroup of photopolymerizable materials, belonging to the class of organic-inorganic nanocomposites. These materials alleviate the shrinkage problem by using a rigid porous matrix in which the monomeric species and the photoinitiator are dispersed. Larger thicknesses than in photopolymers can also typically be achieved.

Holographic photomaterials can be synthesized with sol-gel techniques, as first introduced in 1996 [Cheben’96]. Unlike conventional glass and ceramic fabrication techniques, which require processing at elevated temperatures, sol-gel reactions, first discovered by Ébelemen [Ébelemen’55], allow to synthesize glasses at low temperatures, including room temperature. To this effect, organic components are incorporated in a hybrid organic-inorganic liquid solution which undergoes a gelation process to produce the glass matrix. Sol-gel techniques have been applied to diverse state-of-the art photomaterials, whose main characteristics are shown in table 2.2.

	Δn	Diffraction efficiency (%)	Spatial resolution (lines/mm)
Silica Gel methyl methacrylate organically modified ceramic [Cheben'96]	1.1×10^{-4}	93	54
Photopolymerizable glass with inorganic glassy host [Cheben'01]	3×10^{-4}	98	100
Acrylamide photopolymerizable sol-gel materials [Carretero'04, Murciano'06]	10^{-3}	83	5400
Photopolymerizable glass with Zr-based HRIS [DelMonte'06]	10^{-2}	99	4000

Table 2.2. *Holographic performance for selected photopolymerizable glasses.*

In particular, the present work focuses on the organically-modified photopolymerizable glasses synthesized using sol-gel technique [Cheben'01]. This hybrid organic-inorganic photomaterial is based on a porous silica matrix with dispersed monomeric and photoinitiator species. The sol gel starting solution comprises glycidoxypropyltrimethoxysilane (GMPTS), 2-phenoxyethyl acrylate (POEA) and Tetraethylorthosilicate (TEOS). The reaction is cathalized by hydrochloric acid, and takes place in a controlled temperature between 20ºC and 50ºC. A detailed description of the synthesis procedure is included in Annex A.1.

When exposed to an interference pattern of two mutually coherent light beams with a wavelength within the sensitivity range of the photoinitiator species, polymerization of the monomer is triggered in the illuminated regions of the medium. The polymerization of the monomer results in a reduction of monomer concentration near interference maxima. This monomer concentration gradient results in a migration of monomer molecules from the unexposed regions of the photomaterial towards the illuminated areas. This migration continues even after holographic exposure is finalized, in a process known as dark diffusion. The migrated monomer also takes part in the polymerization and hence in the recording of the diffraction grating, as shown in figure 2.5. As the length of the polymeric chain increases, their mobility within the vitreous matrix is hindered, resulting in a permanent refractive index distribution that follows the interference pattern.

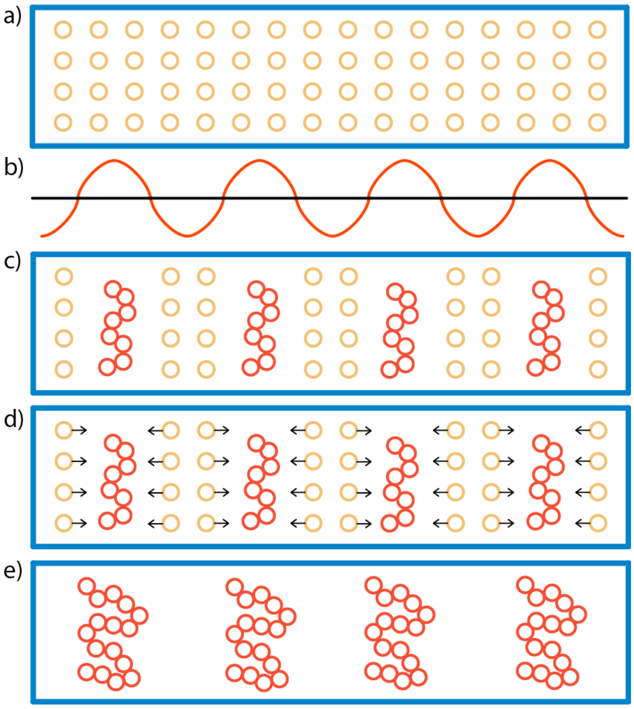

Figure 2.5. *Schematic of the holographic grating recording in a photopolymerizable glass, following Colburn-Haines model for the grating formation [Colburn'71].* ***a)*** *Photopolymerizable glass before exposure.* ***b)*** *Two beam interference pattern.* ***c)*** *Polymerization of the illuminated monomer.* ***d)*** *Monomer diffusion.* ***e)*** *Polymerization of the diffused monomer molecules.*

When exposed to the recording interference pattern, a short delay is observed before diffraction efficiency starts increasing. This delay is referred to as an induction period in which the thermal inhibitors are destroyed and the dissolved molecular oxygen is consumed by the photogenerated free radicals [Cheben'01]. As soon as the polymerization of the monomer starts taking place, an increase in the diffraction efficiency and the refractive index modulation is observed. This temporal evolution of the refractive index modulation in the absence of of actinic light (dark diffusion) can be fitted to a sum of exponential functions, with as many terms as the number of components of the composition contributing to the refractive index modulation [Martínez'07]:

$$\Delta n(t) = \sum C_i \left[1 - e^{-t/\tau_i}\right] \tag{2.21}$$

where C_i is the weight factor that determines the partial contribution of the component i to the refractive index modulation, and τ_i is its difussion time constant. In a medium with a single monomeric species and no additional elements contributing to the refractive index modulation, the dark diffusion process can therefore be fitted to a single exponential function [Piazzola'00]:

$$\Delta n(t) = C_M \left[1 - e^{-t/\tau_M} \right] \tag{2.22}$$

where C_M and τ_M are the weight factor and time constant of the monomer.

In photopolymerizable glasses with a single monomeric species, refractive index modulations up to $\Delta n = 4.5 \times 10^{-3}$ were achieved [Cheben'01], among the highest values reported in a photopolymerizable composition [Calvo'08]. Additionally, synthesized samples presented high sensitivity, a very good optical quality and low scattering.

2.3.1. Photopolymerizable glasses with high refractive index species

The refractive index modulation limit of sol-gel photopolymerizable glasses was further increased in 2006 by the incorporation of a High Refractive Index Species (HRIS) at molecular level [DelMonte'06]. In particular, the HRIS used was a combination of zirconium isopropoxide $Zr(O_iPr)_4$ with metacrylic acid (MA) as a chelating agent to prevent the precipitation of the zirconia clusters. The glass matrix is synthesized by hydrolisis of zirconium and silica alcoxides $\{Si, Zr\}(OR)_n$, with R being R an alkyl group, followed by a polycondensation reaction:

$$\{Si, Zr\}(OR)_n + nH_2O \rightarrow \{Si, Zr\}(OH)_n + nR(OH) \tag{2.23}$$

$$\{Si, Zr\}(OH)_n \rightarrow MO_{n/2} + \frac{n}{2} H_2O \tag{2.24}$$

During light exposure, polymerization and diffusion mechanisms within the glass matrix result in a variation of the HRIS concentration following the interference pattern. Since the refractive index of the zirconium dioxide (n ~ 2.2 at 632.8 nm wavelength) is greater than the average of the glass matrix (n ~ 1.45 at the same wavelength), this distribution of the HRIS concentration further increases the achievable refractive index modulation up to $\Delta n \sim 10^{-2}$ [DelMonte'06]. Additionally, the incorporation of HRIS to polymeric photomaterials has shown to increase the photomaterial sensitivity [Omura'10]. When the HRIS is included in the glass matrix and it is free to diffuse, the temporal evolution of Δn after a recording pulse can be fitted to the sum of two exponentials [Martínez'07]:

$$\Delta n(t) = C_M \left[1 - e^{-t/\tau_M} \right] + C_{HRIS} \left[1 - e^{-t/\tau_{HRIS}} \right] \tag{2.25}$$

where C_{HRIS} and τ_{HRIS} are the weight factor and diffusion time constant of the HRIS, respectively. The larger molecular weight of HRIS compared to monomer species results in a longer diffusion time for HRIS ($\tau_M < \tau_{HRIS}$).

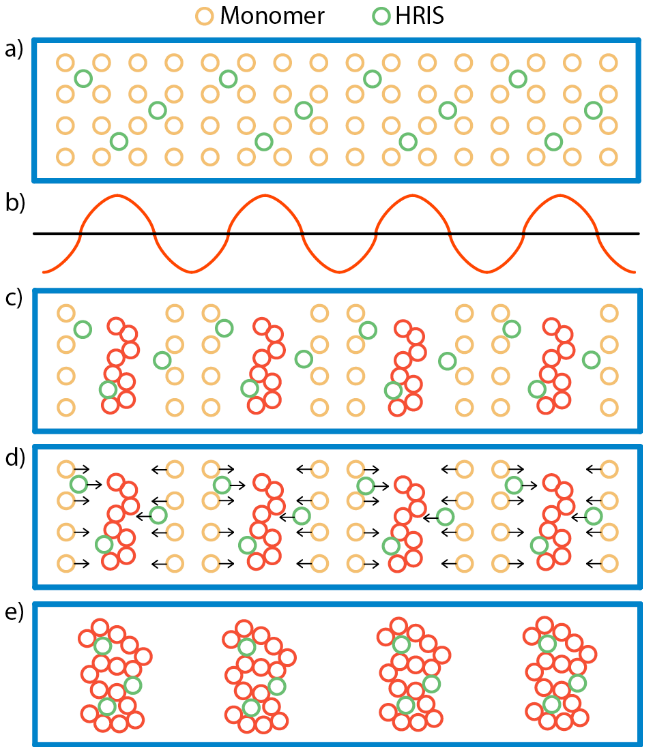

Figure 2.6. *Schematic of the holographic grating recording in a photopolymerizable glass incorporating HRIS.* ***a)*** *Photopolymerizable glass before holographic exposure.* ***b)*** *Two-beam interference pattern.* ***c)*** *Polymerization of the illuminated monomer.* ***d)*** *Diffusion of the remaining monomer and HRIS species.* ***e)*** *Polymerization of the diffused monomer and metacrylic acid.*

Photopolymerizable glasses incorporating HRIS have shown remarkable performance for the recording of volume phase holographic gratings (VPHG). High refractive index modulation, sensitivity, excellent optical quality and low scattering for a wide range of spatial frequencies and recording and readout conditions [Calvo’06, Martínez’09, Martínez’10]. The photopolymerizable glass incorporating HRIS has been used to develop devices for polarization control [Martínez‘09a]. This photomaterial has also shown remarkable performances for femto-second pulse shaping [Hernández’11], with a high Laser Induced Damage Threshold (LIDT). The material was also used to observe Pendellösung effect for the first time at optical wavelengths [Calvo’06].

2.4. Holographic filters

2.4.1. Applications

One of the most important applications of holographic photomaterials is optical filtering. Holographic filters have been used in diverse fields, such as microscopy [Barbastathis'99], spectral identification of chemical compounds [Cao'09], automatic recognition of visual patterns [Fujii'80, Fleisher'90], and transformation of continuous and pulsed laser beams [Quintanilla'81, Hernández'11], to name a few.

In particular, by recording a Bragg diffraction grating in a holographic photomaterial, efficient passband and stopband filters have been implemented [Rakuljic'93]. An attractive feature of holographic filters is that spectral bandwidth can be controlled by modifying the spatial frequency of the recorded grating and the thickness of the holographic medium. This has allowed the development of holographic notch filters [Schoen'93] with a high suppression ratio in a narrow wavelength range.

One of the applications which benefits from holographic notch filters is Raman spectroscopy [Xie'02]. Raman spectroscopy allows the spectral characterization and identification of molecules through their unique vibrational and rotational modes [Colthup'90]. As shown in figure 2.7, the sample under analysis is illuminated with a monochromatic laser source, which interacts with the vibrational and rotational modes of the molecules, with frequency shifts resulting from Raman scattering process.

The induced Raman scattering is typically collected in a spectrometer setup. However, Raman scattering signal is typically several order of magnitude weaker than elastic Rayleigh scattering, and can hence be masked by the presence of the latter. For this reason, Raman spectroscopy configurations require an efficient notch filter with a very narrow bandwidth around the pump wavelength. Due to their high diffraction efficiency and narrow passband, holographic notch filters are often used for this purpose [Xie'02, Carrabba'90, Pelletier'91].

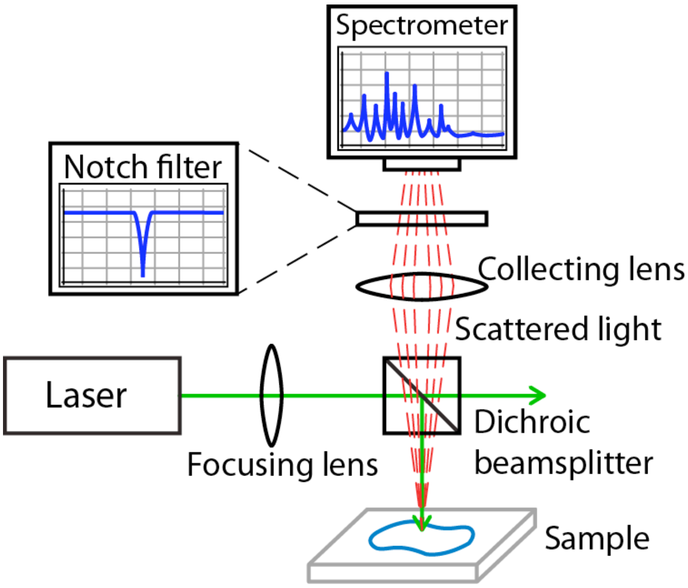

Figure 2.7. *Schematic of a typical Raman spectroscopy setup.*

2.4.2. Holographic filter thickness limitation

In order to develop high-quality optical filters, a holographic medium with a high refractive index modulation, low absorption and low scattering is required [Karsten'07]. Photopolymerizable materials have shown excellent performance in terms of dynamic range and optical quality [Sincerbox'94, Lessard'95]. In particular, sol-gel photopolymerizable glasses with HRIS [DelMonte'06] present an extremely low scattering and a high refractive index modulation that allows diffraction efficiencies close to 100%, making them promising candidates for applications in spectral filtering.

Nevertheless, when a very narrow notch or passband filter is required, two additional requirements need to be meet to reduce the filter bandwidth, namely, large spatial resolution and thickness. Regarding the first issue, photopolymerizable glasses have proven some of the highest spatial resolutions among holographic photomaterials, with holographic gratings of spatial frequencies of 4000 lines/mm [Martínez'09b].

However, organic polymeric binders used in holography are typically limited to thicknesses of less than a few hundred micrometers. This is also the case of the photopolymerizable glasses with HRIS [DelMonte'06], with a maximum thickness of ~200 µm. In order to make narrowband notch filters while benefiting from the optical quality, sensibility, resolution and dynamic range of photopolymerizable glasses with HRIS, this thickness limitation needed to be overcome. For this purpose, a novel formulation and synthesis process was developed as part of the studies presented in this thesis, as detailed in section 4.1.

2.5. Ionic liquid

Ionic liquids have focused a great interest in the last years both in fundamental chemistry and in industrial fabrication processes, as a “green” alternative to conventional solvents for chemical reactions [Wassercheid'03, Klingshirn’05]. Ionic liquids are organic salts with ionic structure that are found in liquid form at room temperature. They present an extremely low volatility, which is desirable in many chemical processes as it prevents the evaporation of toxic substances which is typical of other solvents. Ionic liquids also present a high viscosity [Sanmamed’07].

Other advantages of ionic liquids are their high thermal stability, high polarity, and hydrophilic behavior. Additionally, ionic liquids have been shown to remarkably accelerate polymerization reactions [Carmichael’00, Hong’02, Harrisson’02]. In particular, this effect has been demonstrated for some holographic media based on photopolymers [Lin’08]. Furthermore, the incorporation of ionic liquid resulted in an increase of the sensitivity of the photomaterial, as well as its spatial resolution and refractive index modulation. Efficiencies up to 34% were reached in a 10-µm-thick sample.

The incorporation of ionic liquid to the composition of photopolymerizable glass typically results in an increased scattering in the recorded diffraction grating [Lin’09]. The amount of induced scattering depends on the concentration of ionic liquid in the sample. This is usually an undesirable effect for data storage and filtering applications, but can be advantageously applied to the design of optical diffusers [Lin’09].

In particular, we studied the incorporation of ionic liquid to hybrid organic-inorganic photopolymerizable glasses aiming for increased sensitivity and accelerated polymeric reactions, as well as to study the fundamental processes of holographic recordings in this photomaterial. 1-Butyl-3-methylimidazolium tetrafluorborate [bmin][BF_4] was chosen as the ionic liquid to be incorporated to the photopolymerizable glasses in the present study. Its chemical structure is shown in figure 2.8.

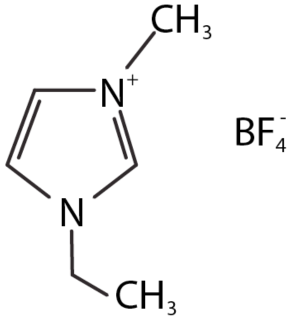

Figure 2.8. *1-Butyl-3-methylimidazolium tetrafluorborate chemical structure.*

The effects of incorporating this particular ionic liquid to photopolymerizable glasses, both with and without HRIS, were characterized in terms of refractive index modulation, diffraction efficiency, dark diffusion, scattering and optical quality, as shown in section 4.2. Furthermore, the viscosity of the photomaterial solutions with and without ionic liquid was analyzed with single particle micro-rheology techniques [Domínguez'11]. Ionic liquids present a high viscosity [Sanmamed'07], which affects the overall viscosity of the solution and the diffusion dynamics within the vitreous matrix. In particular, studies performed at the Chemical Sciences Faculty of UNED showed a viscosity of 20 mPa.s for the photopolymerizable glass solution without ionic liquid, and 90 mPa.s for the solution incorporating ionic liquid, which explains the slower dark diffusion dynamics of the latter.

Besides the aforementioned studies, the incorporation of choline chloride to photopolymerizable glasses was also tested. Choline chloride is an organic salt that can be used to synthesize ionic liquids to act as non-volatile solvents in chemical processes [Abbott'04, Sheu'02]. However, preliminary studies showed a very poor coexistence with the Zirconium-based HRIS, resulting in precipitation of the solution before the start of the gelation process.

2.6. Goals of the present work

The main goal of the present research in sol-gel based photopolymerizable glasses is to enhance its previous performances in order to implement high quality holographic filters. In particular, we focused on the design of highly-selective notch and passband holographic filters.

To overcome the thickness limitations of photopolymerizable glasses incorporating HRIS, a new formulation and synthesis method were proposed. The effect of sample thickness on holographic responsivity, refractive index modulation, scattering and dark diffusion of the photomaterial were characterized. Additionally, the incorporation of ionic liquid to photopolymerizable glasses was studied.

The respective results are included in chapter IV of the present thesis. The synthesis processes for the conventional formulation, for the photomaterial incorporating ionic liquid, as well as the recording and characterization setup used in these studies are further detailed in Annex A.

III

Introduction to photonic devices based on planar silicon waveguides

Recent advances in silicon photonics have enabled the development of compact optical integrated circuits including modulators, switches, photodetectors, wavelength multiplexers, spectrometers and sensors. In this chapter, the state of the art of integrated photonic devices based on silicon waveguides is revised. In particular, polarization mode converters, demultiplexers, filters and spectrometers for this platform are presented, providing the theoretical background for the photonic devices designed and fabricated as part of the present thesis.

3.1. The silicon-on-insulator platform

In the last years, there has been a worldwide debate in the photonics community regarding which technological platform is best suited for integrated optics, the two main contenders being Silicon-on-Insulator (SOI) [Reed'08, Lockwood'10] and III-V semiconductor platforms such as indium phosphide [Nagarajan'10] and gallium arsenide [Vodopyanov'08].

One of the main advantages of silicon-based integrated optics is the high refractive index contrast ($\Delta n \sim 2$) between the silicon waveguides and the insulator SiO_2 cladding. This refractive index contrast results in highly-confined optical mode with bend radii as small as a few micrometers, which enables a dense waveguide integration and a substantial reduction of the footprint of the photonic devices [Cheben'03].

The main drawback of SOI compared to III-V semiconductors is the lack of active elements such as light sources, and specifically lasers [Tanaka'90]. This issue is specially relevant given the fact that one of the main drivers for silicon integrated photonic research is potentially overcoming the bandwidth bottleneck of copper interconnect communications where active elements are crucial.

In an effort to overcome these limitations, light emitting diodes in silicon integrated optics have been demonstrated [Green'01], although the efficiencies still do not match those of the III-V sources. In a more viable approach, hybrid alternatives have been pursued to integrate active elements such as germanium with silicon [Campenhout'08]. With recent advances in SOI and III-V integration technologies [Justice'12], silicon-based circuits are becoming increasingly competitive in a wide range of photonic applications, and not only in passive components. Light sources [Dehlinger'04], modulators [Roth'07], and photodetectors [Chen'09] have been developed, resulting in integrated transceivers modulation speeds exceeding 40 Gbps [Zheng'12].

Furthermore, SOI offers distinct mass-scale manufacturing and commercialization benefits. SOI photonic circuits are CMOS compatible, and their fabrication techniques take advantage of an enormous existing infrastructure developed for silicon micro-electronics. Additionally, the cost of silicon wafers is significantly lower than those of III-V materials, facilitating the production of low cost photonic chips. Presently, SOI is a remarkably versatile platform that can be applied to a wide range of applications, extending beyond optical communications and interconnects (which remain its main drivers), and into handheld spectrometers, disposable sensors for environmental and biological analysis, and space-born devices, to name a few.

In particular, in the works of the present thesis, we focus our research on exploiting the benefits of the high refractive index contrast of the SOI platform in order to develop very compact high-performance passive photonic devices for spectral and polarization handling. These photonic devices can be used as generic building blocks for various applications including optical communications and interconnects, biological and environmental sensing, and spectroscopy.

Details about the fabrication techniques of integrated optical silicon chips are included in Annex A.4.

3.2. Spatial heterodyne Fourier-transform spectrometers

3.2.1. Introduction to Fourier-transform spectroscopy

Fourier-transform spectrometry [Becker'72, Griffiths'07] is a powerful spectral analysis technique, essentially based on the classical Michelson interferometer set-up [Michelson'87]. The output intensity of the interferometer is measured for a varying optical path difference (Δx_i) between the interferometer two arms, typically implemented with a moving mirror as it is schematically shown in figure 3.1. By scanning the interferometer optical delay, a wavelength-dependent pattern is obtained, from which the input spectrum is calculated by Fourier transformation (FT).

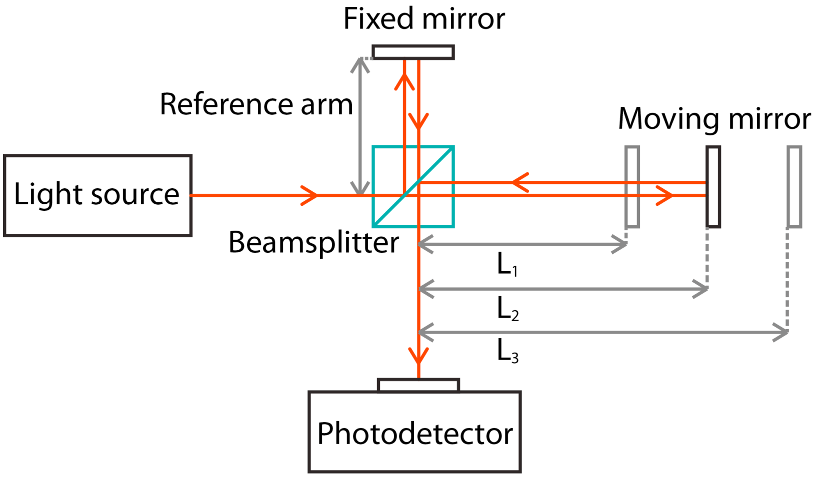

Figure 3.1. A typical *Fourier-transform spectroscopy setup based on a Michelson interferometer. A moving mirror is used to sample a plurality of optical path differences between the two arms of the interferometer. The input spectrum is calculated from the measured intensity variations by Fourier transformation.*

This spectroscopic configuration presents two main advantages. First, it benefits from the intrinsically large *étendue* (optical throughput) of the Michelson interferometer [Jacquinot'54], making it particularly suitable for the analysis of spatially extended and incoherent light sources. Secondly, the spectral resolution of the device is determined by the longest optical path difference between the arms of the interferometer, allowing to achieve high resolutions by using a longer optical path delay. In particular, latest developments have incorporated optical delays as long as 11.7 meters, reaching a resolution of 0.0005 cm^{-1} [Albert‘11a]. Due to the versatility and high resolution of Fourier-transform spectroscopy, this kind of spectrometers have extensively been used in a wide range of applications in industry and academia. Emerging advanced applications include the highly-resolved analysis of electronic structures in the UV range [DeOliveira’11] or the spectral analysis of extrasolar planets in order to search for spectral lines associated with the presence of biological molecules [Schwartz’12]. Furthermore, Fourier-transform spectrometers can be used in combination with extreme laser sources, such as the Prague Asterix Laser System (PALS) [Jungwirth’05] or the Extreme Light Infrastructure (ELI) project [Mourou’11], which provide ultra short pulses (10-15 fs) with a power up to 10 Petawatts. This operation range enables the study of light-matter interactions at an intensity 10 times higher than the previously achievable levels, enabling the highly-resolved analysis of chemical and physical processes occurring in high-energy laser sparks. The high spectral resolution and *étendue* advantage of Fourier-transform spectroscopy makes this technique particularly well suited for applications in astrophysics, such as the analysis of the Unidentified Infrared Band (UIB) found in interstellar spectra [Albert‘11b], or the location of exoplanets with Earth-like mass and orbit [Wilken’12].

However, in order to perform accurate spectroscopic measurements with high-resolution Fourier-transform spectrometers, a high degree of stability of the setup must me maintained. This is particularly challenging as large-scale bulk optical instruments are required to implement the long optical path delays. Also, the need of a moving element (mirror) to sample the optical delay line impose strict requirements on precision of mechanical components, and implies a prolonged acquisition time for each spectral measurement, further complicating the stabilization of the device.

3.2.2. Spatial heterodyne Fourier-transform spectroscopy

Spatial heterodyne Fourier-transform (SHFT) spectroscopy [Harlander’04] circumvents the need for a moving mirror by performing all the interferometric measurements in parallel and instantaneously, resulting in an output stationary spatial pattern which contains the information equivalent to the original optical delay line sweep. That is, instead of having a single output which varies temporally as different optical path differences are sampled, SHFT provides a plurality of stationary outputs, each of them corresponding to a different optical path difference. As a consequence, the full set of interferometric measurements can be performed in a single shot, greatly reducing the temporal stability requirements, while additionally allowing time-resolved spectral measurements. This is particularly advantageous when dynamic chemical reactions are analyzed, and it can be applied to both continuous and pulsed light sources.

SHFT spectroscopy concept was originally implemented in a bulk optic configuration in the ultraviolet range [Harlander'92, Harlander'02] by replacing the moving mirrors by diffraction gratings, as shown in figure 3.2. In this implementation, the input light beam is collimated and split into two arms, each arm comprising a diffraction grating rotated at an angle θ from the direction of light propagation. The optical beams are diffracted by the two gratings with wavelength-dependent angles of opposite signs, so when the two wavefronts are combined at the beamsplitter, a stationary two-beam interferometric pattern is produced. For a monochromatic input, this process results in a periodic stationary pattern, with a period determined by the input wavelength. For an arbitrary spectral signal, Fourier decomposition yields a plurality of spectral components, each of these components producing its own stationary interference pattern with a specific period. The total output interferogram is formed as the sum of all the contributing Fourier components. As a result, an imaging plane perpendicular to the propagation direction of the output light beam comprises spatially distributed interferometric information of the spectral density of the input signal.

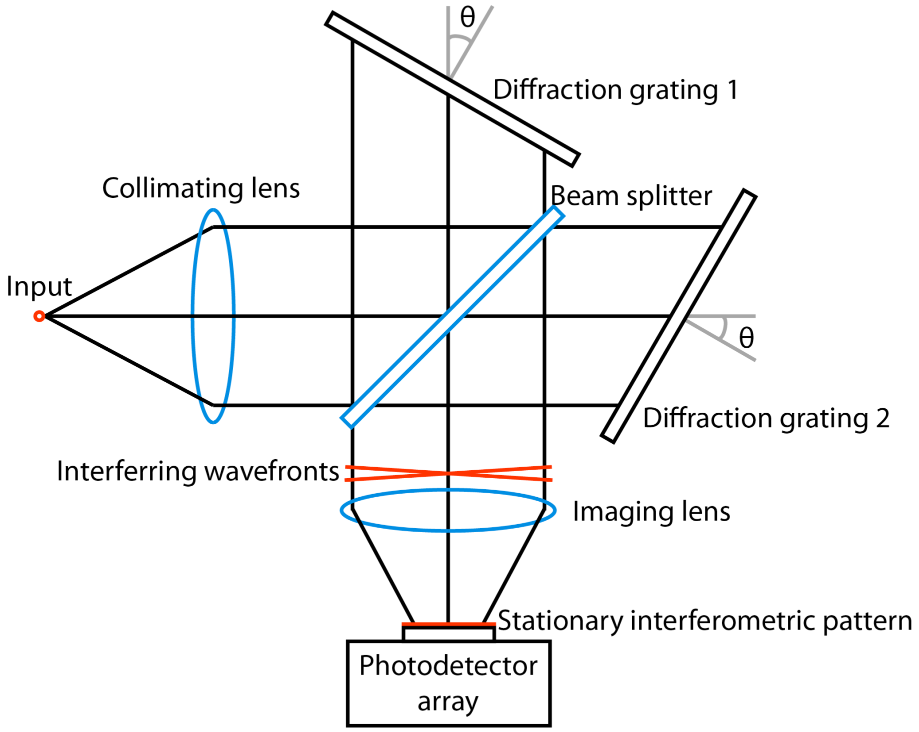

Figure 3.2. *Spatial heterodyne Fourier-transform spectrometer implemented using bulk optics. Mirrors in the Michelson interferometer are replaced with diffraction gratings. The angular tilts (θ) of the gratings results in an stationary interference pattern at the photodetector, where each point corresponds to a sampled optical path difference of an equivalent Michelson interferometer.*

In other words, the time-variant signal of a conventional Fourier-transform interferometer, which comprises the information of sweeping a range of optical path differences, is effectively converted into a spatially-variant signal comprising the same substantial information. The intensity at each position of the imaging plane hence corresponds to a sampled optical path difference of a Michelson interferometer. The output intensity spatial distribution is measured with a photodetector array, for example a CCD camera or focal plane array. As each position of the photodetector array is mapped to an optical path difference, the input spectral density distribution can be retrieved with conventional Fourier-transform methods. This can also be regarded as an application of the Wiener-Khinchinn theorem relating the autocorrelation function and the signal spectrum through the Fourier transformation [Cohen'95]. A more detailed discussion on the spectral retrieval process is included in section 3.2.3.

Since the SHFT configuration only requires stationary and passive components, the concept can be readily implemented in SOI integrated optics by using waveguide interferometers. In particular, the stationary diffraction gratings can be implemented in planar waveguides with arrayed waveguide gratings [Cheben'05]. Similarly to bulk optics FT spectrometers, integrated SHFT spectrometers have an increased *étendue* and can be implemented with a large input aperture. For example, a planar input waveguide with a width up to 40 μm was demonstrated without deterioration of the device performance. This is a significant advantage compared to other integrated spectrometers such as AWGs [Cheben'07b] or waveguide echelle gratings [Janz'04], whose optical throughputs are limited by the requirement of a single monomode wire waveguide.

A specific consequence of the integration of SHFT devices is the discretization of the output interferogram. Whereas in bulk optics SHFT spectrometers the output interferogram is continuous, and is only discretized by sampling with the pixels of the photodetector array [Harlander'02], in an integrated SHFT spectrometer there is a finite number of receiver waveguides, each of them sampling the optical power corresponding to a specific optical path difference of an interferometer. Since each output waveguide implements an interferometric measurement of linearly increasing optical path difference, an array of Mach-Zehnder Interferometers (MZI) with linearly increasing length differences between their arms can be used [Florjańczyk'07], as shown in figure 3.3. In particular, the use of an interferometer array enables a multiple aperture input, with the subsequent increase in *étendue* compared to conventional planar waveguide spectrometers. Furthermore, by providing independent access to each interferometer output, fabrication deviations from the ideal behavior, as well as environmental fluctuations, can be calibrated and compensated. A detailed analysis of a SHFT inteferometer array is presented in section 3.2.3

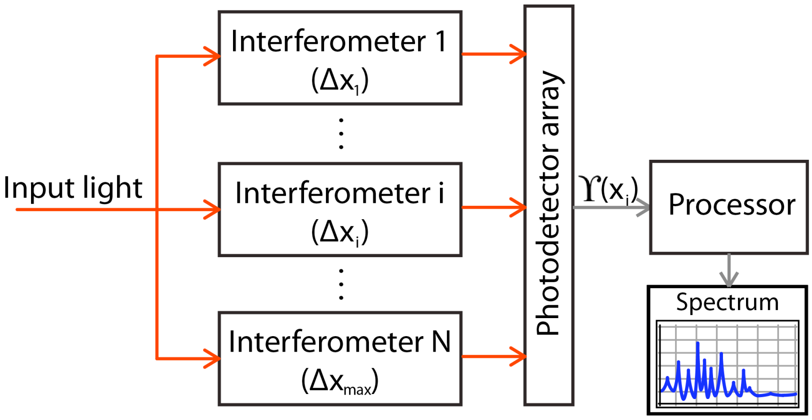

Figure 3.3. *Schematic of a spatial heterodyne Fourier-transform spectrometer based on an array of Si-wire waveguide Mach-Zehnder interferometers with linearly increasing optical path differences. Input light is coupled to the interferometer array, resulting in an output stationary wavelength-dependent interferogram $\Upsilon(x_i)$. The interferogram is measured in a single shot with a photodetector array. A Fourier-transform spectral retrieval algorithm is applied to compute the spectrum of the input signal.*

In particular, in the works presented in this thesis we build upon the MZI array configuration [Florjańczyk'07], and benefit from the high refractive index and optical mode confinement in Si-wire waveguides in order to implement very long optical delays in a reduced footprint. In particular, tightly coiled microphotonic spiral waveguide with linearly increasing length were used to increase the resolution and to substantially reduce the footprint of the device. The design, fabrication and experimental demonstration of SHFT spectrometer with microphotonic spirals is presented in section 5.1.

3.2.3. Theoretical framework of an SHFT interferometer array

We shall consider a light source illuminating an array of N Mach-Zehnder waveguide interferometers with linearly increasing length differences (ΔL_i = iΔL) between the two arms of each interferometer, up to a maximum value ΔL_{max}. These physical length differences result in optical path differences:

$$\Delta x_i = i\Delta x = n_g \Delta L_i = i n_g \Delta L \tag{3.1}$$

where Δx is the optical path difference increment between consecutive intereferometers and n_g is the group index of the fundamental mode of the interferometer arm waveguide:

$$n_g = \frac{c}{v_g} = \frac{n}{1 + \frac{\lambda}{n}\frac{dn}{d\lambda}} \tag{3.2}$$

where c is the speed of light in the vacuum, v_g is the group velocity, n is the refractive index of the medium, and λ is the wavelength. Therefore, the output of the MZI array is a discretization of the response of a single MZI with a continuous optical path difference sweep, with a sampling function defined by a Dirac comb *D(x)* with a period equal to the the optical path difference increment Δx:

$$D(x) = \sum \delta(x_i) = \sum_{i=1}^{N} \delta(i\Delta x) \tag{3.3}$$

The transmittance of each MZI is therefore a periodic (sinusoidal) function with maxima at:

$$\sigma_{\max}(i) = k\Delta x_i = ik\Delta x = kn_g\Delta L_i \tag{3.4}$$

where $\sigma_{max}(i)$ are the wavenumbers (inverse of the wavelength) corresponding to the maxima of the i-th MZI transfer function and k is an integer number. In an ideal case with linear optical path difference increments, and in absence of phase errors in the MZI array, there is a plurality of periodically spaced wavenumbers, also referred as Littrow wavenumbers (σ_L), for which all the MZI of the array have maximal transmittance (Fig. 3.4.a), that is:

$$\sigma_L = k\Delta x_{\max} = kN\Delta x \tag{3.5}$$

For a narrowband light source at an arbitrary wavenumber between two consecutive Littrow wavenumbers, the output of the MZI array is a stationary periodic pattern (Fig. 3.4.b), with a wavelength-dependent period. The periodicity property of the transmittance functions of the interferometers also implies that for two arbitrary input narrowband sources with central wavenumbers separated by the distance equal to the separation of two Littrow wavenumbers, the output interferogram $\Upsilon(x_i)$ is invariant:

$$\Upsilon(\sigma, x_i) = \Upsilon(\sigma \pm n\Delta\sigma_L, x_i) \tag{3.6}$$

where n is an integer number and $\Delta\sigma_L$ is the difference between two consecutive Littrow wavenumbers. Furthermore, the interferogram is also symmetrical respective to the center wavenumber between two Littrow wavenumbers:

$$\Upsilon(\sigma_L + \frac{\Delta\sigma_L}{2} - \Delta\sigma, x_i) = \Upsilon(\sigma_L + \frac{\Delta\sigma_L}{2} + \Delta\sigma, x_i) \tag{3.7}$$

where $\Delta\sigma$ is an arbitrary wavenumber separation. As a consequence, the Free Spectral Range (FSR) of the device is half the separation between two Littrow wavenumbers. In particular, we shall consider a FSR starting at a Littrow wavenumber:

$$FSR \in (\sigma_L, \sigma_L + \frac{\Delta\sigma_L}{2}) \tag{3.8}$$

Within said FSR, the transformation between the reciprocal spaces defined by the input spectrum and the output pattern is linear and univocal. Since any input spectrum can be expressed as the linear combination of multiple narrowband sources, the corresponding output pattern is a linear combination of the outputs associated to said plurality of narrowband sources (Fig. 3.4.c).

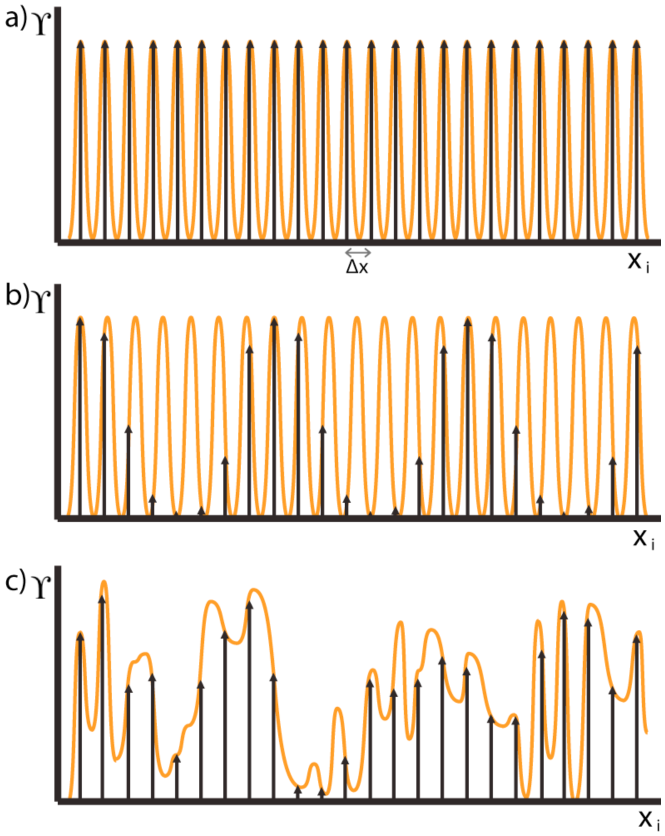

Figure 3.4. *Continuos interferometric response of a Mach-Zehnder Interferometer (orange) and discretized stationary interferometric output patterns Υ of a spatial heterodyne Fourier-transform spectrometer (black), as a function of the optical path difference x_i, for the following input spectral distributions:* ***a)*** *An ideal monochromatic light source at a Littrow wavenumber.* ***b)*** *An ideal monochromatic light source at a wavenumber different from the Littrow wavenumber.* ***c)*** *An arbitrary spectral distribution within the free spectral range of the device.*

By generalizing this fundamental concept, we can express the output interferogram Υ (x_i) generated by any arbitrary spectral density $B(\sigma)$ within an aliasing-free FSR as a cosine Fourier transformation:

$$\Upsilon(x_i) = \int_0^{FSR} B(\bar{\sigma}) \cos 2\pi\bar{\sigma} x_i d\bar{\sigma} \tag{3.9}$$

where $\bar{\sigma}$ is the wavenumber relative to the Littrow wavenumber ($\bar{\sigma} = \sigma - \sigma_L$). Given the univocality of the transformation within the FSR, for an output interferogram generated by an arbitrary input signal under analysis, the corresponding input spectral distribution can be computed by a discrete cosine Fourier transform:

$$B(\bar{\sigma}) = \frac{2\Delta x_{\max}}{N} \sum_i^N \Upsilon(x_i) \cos 2\pi\bar{\sigma} x_i \tag{3.10}$$

The wavelength resolution $\delta\lambda$ of this configuration is determined by the maximum optical path difference of the most unbalanced interferometer (equivalent to the maximum length of the optical delay line of a conventional Fourier-transform spectrometer):

$$\delta\lambda = \frac{\lambda_0^2}{\Delta L_{\max} n_g} \tag{3.11}$$

where λ_0 is the central operation wavelength of the device. The analysis range is limited by the shortest optical path difference, which given the linear spacing of optical path differences between interferometers, is in turn determined by the number N of interferometers of the array (equivalent to the number of sampling points in a conventional Fourier-transform spectrometer):

$$FSR = \delta\lambda \frac{N}{2} \tag{3.12}$$

It should be noted that integrated SHFT spectrometers provide multiple discretized outputs, and therefore Eq. (3.10) is a finite summation of terms corresponding to sampled optical path differences. This discretization inherently results in the truncation of the spatial interferogram, which in turn generates oscillatory ripple in the retrieved spectrum. This effect is well-known in classical Fourier-transform spectroscopy, and can be reduced by applying an apodization window $W(x_i)$ to the spectral retrieval algorithm of Eq. (3.10):

$$B(\bar{\sigma}) = \frac{2\Delta x_{\max}}{N} \sum_i^N \Upsilon(x_i) W(x_i) \cos 2\pi\bar{\sigma} x_i \tag{3.13}$$

The apodization window reduces the weight applied to the terms corresponding to the longer optical path differences, and smooths the transition between the sampled points and the cut-off region, thereby reducing the ripple resulting from the Fourier transform. As shown by figure 3.5, different apodization windows can be used, each of them presenting an inherent spectral broadening and sidelobe level. A trade-off between these two factors needs to be considered when selecting the apodization window for a particular application, with the optimal function being determined by the resolution requirements of the application.

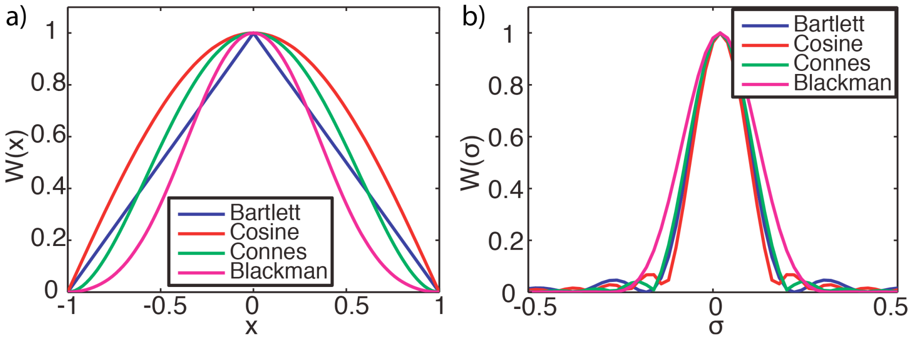

Figure 3.5. ***a)*** *Examples of apodization functions W(x) for ripple reduction in Fourier-transform spectroscopy, as used in Eq. (3.13).* ***b)*** *Fourier transform of the apodization functions.*

Bartlett function (triangle function): $W(x) = 1 - \frac{|x|}{a}$

Cosine function: $W(x) = \cos\left(\frac{\pi x}{2a}\right)$

Connes function: $W(x) = \left(1 - \frac{x^2}{a}\right)^2$

Blackman function: $W(x) = \frac{21}{50} + \frac{1}{2}\cos\left(\frac{\pi x}{a}\right) + \frac{2}{25}\cos\left(\frac{2\pi x}{a}\right)$

The spectral retrieval using Eq. (3.10) and Eq. (3.13) implies an ideal case in which the output transmittance functions match perfectly the theoretical response of the interferometers. Nevertheless, two main deviations from the ideal behaviour need to be considered in a practical experiment. First, waveguide propagation losses result in amplitude errors and uneven fringe visibility along the interferometer array. The visibility V of a MZI transmittance function, which defines the relation between the maximum output intensity I_{max} and the minimum output intensity I_{min} is determined by Eq (3.13). The particular case of a fully coherent source ($|\gamma(\tau)|=1$) is considered, with $\gamma(\tau)$ being the degree of complex coherence.

$$V = \frac{I_{\max} - I_{\min}}{I_{\max} + I_{\min}} = \frac{2\sqrt{I_1 I_2}}{I_1 + I_2} \tag{3.14}$$

where I_1 and I_2 are the intensities in each arm of the interferometer before recombination. From Eq. (3.14) it is obvious that the visibility is maximal when the two arms are balanced (same output intensity), and decreases with the unbalance of output intensities. Due to waveguide propagation losses, the output intensity of an MZI arm decreases as its length increases, resulting in a reduced visibility for increasing optical path difference Δx_{i}. This visibility reduction fundamentally limits the maximum optical path difference of the spectrometer, and therefore its resolution. However, even in a typical operation regime far from this fundamental limit, the effect of reduced visibility needs to be accounted for to avoid distortions in the retrieved spectrum. Advantageously, this effect can be mathematically compensated by making each term of the interferogram relative to the maximum output power range of the interferometer:

$$B(\bar{\sigma}) = \frac{2\Delta x_{\max}}{N} \sum_{i}^{N} \frac{\Upsilon(x_i) - I_{\min}(x_i)}{I_{\max}(x_i) - I_{\min}(x_i)} W(x_i) \cos 2\pi\bar{\sigma} x_i \tag{3.15}$$

The second deviation from the theoretical model is caused by the phase errors in the interferometers transmittance functions, resulting from deviations in the oscillation frequency of each interferometer. Fabrication deviations from the designed geometrical length difference of the device and changes of mode propagation constants (for example caused by changes in waveguide width) result in errors in the optical path lengths across the array. This results in a misalignment of the transmittance functions with random wavelength shifts between the maxima for different interferometers. With this degeneration of the alignment of the interferometers, the condition for the Littrow wavenumbers presence is not met by the array. Spectral retrieval by using Eq. (3.10), in which all wavenumbers are relative to the Littrow wavenumber, cannot thereby be applied. Environmental variations such as temperature changes can induce additional phase shifts in the transmittance functions of the interferometers, distorting the interferograms associated with a given input spectrum.

In order to correct the phase errors and correctly retrieve the input spectrum, two different approaches can be followed. First, the phase errors can be actively corrected by dedicated phase shifting elements in each interferometer, therefore aligning the responses of all the interferometers of the array to Littrow condition. In the case of planar waveguide SHFT spectrometers, this can be performed by incorporating independent heaters as phase shifters for each interferometer [Takada'11] to tune each transmittance function independently. This way, a maximum of each interferometer is aligned to the Littrow wavenumber and cosine Fourier-transform spectral retrieval of Eq. (3.10) can be used. However, this approach adds to fabrication complexity since independent heaters, control electronics, and an elaborate tuning process before each measurement are required.

As an alternative approach, we propose to incorporate the phase errors measured in a calibration step directly into the spectral retrieval algorithm, circumventing the need of using active phase compensation. In the present thesis, a novel spectral retrieval algorithm based on the inversion of a calibration matrix is developed (section 5.1), capable of a robust compensation of fabrication errors and environmental changes. This phase error compensation technique relies entirely on computational tools, circumventing the need of dedicated hardware elements to actuate on the spectrometer.

Finally, some additional considerations should be made regarding the *étendue* and configuration of the inputs and outputs of SHFT spectrometers implemented with photonic waveguides. In a conventional integrated spectrometer (e.g. AWG), the *étendue* is limited by the optical throughput of a single input monomode waveguide. Since waveguide SHFT spectrometers can be implemented with an array of N independent interferometers, two different input configurations can be used, namely, a single input waveguide and a multiple aperture input. In the first case, the *étendue* of the device is also limited by the single waveguide, with incoming light being split into the interferometer array, for example by cascaded y-splitters. As a result, the same signal is sent to all the interferometers of the array, as assumed by the previous theoretical model. Some distortions of the MZI transmittance functions can arise from light splitting elements and resulting Fabry-Pérot resonances, but this effect is typically negligible with state-of-the-art splitters. Furthermore, this effect is spectrally stationary, and is therefore corrected by the calibration matrix retrieval algorithm.

As an alternative to this configuration, the *étendue* limitation can be overcome by using a separate input waveguide for each of the N interferometers. In this case, the total *étendue* of the device is N times larger than the *étendue* of an input waveguide, this configuration being particularly desirable for analyzing spatially extended light sources. When spatially extended light sources are used, the input spectral content of the signal is coupled into all the interferometers of the array through the input waveguides, the thereby enabling to use the same theoretical model and retrieval algorithm as in the single aperture configuration.

The high mode confinement of silicon wire waveguides enable separations between adjacent input waveguides in the order of micrometers without incurring in coupling effects. Together with the small bend radii (a few micrometers) of Si-wire waveguides, this enables a dense interferometer integration for increased resolution and FSR in a small footprint. Greater separations between input waveguides can be implemented for spatially extended sources with a larger beam size, without detriment in the spectral retrieval process. On the output plane, each MZI output is measured independently and in parallel. The distance between outputs, the pixel size of the photodetector array, and the light collecting scheme (if present), are thereby judiciously designed to prevent any interference between adjacent MZI outputs.

3.3. Polarization mode converters

The high refractive index contrast of the SOI platform can be advantageously used to achieve high density integration. However, this advantage comes at the cost of a large polarization dependence of silicon waveguides [Cheben'03, Dai'04]. In SOI waveguides, quasi-TE (Transversal Electric) and quasi-TM (Transversal Magnetic) modes have significantly different propagation constants and experiment different propagation losses. As a consequence, most photonic devices implemented in silicon wire waveguides are nominally designed to operate for a single polarization (typically TE). In applications where input light polarization is undetermined, the polarization diversity technique is typically used [Fukuda'08]. In this technique, a polarization splitter [Fukuda'06, Kiyat'05, Liang'05] divides TM- and TE-polarized light into two waveguides. Light polarization in one of the waveguides is rotated by a polarization converter, achieving the same polarization state at the outputs of the two waveguides, which are coupled into two identical photonic circuits. At the output of the circuit operating with the rotated polarization, an additional polarization mode converter returns the signal to its original polarization state, and both outputs are recombined.

In order to evaluate the performance of a polarization converter several parameters need to be considered. The main parameter is polarization conversion efficiency (η), defined as the ratio between the power of the converted polarization and the total output power. That is, for TE-to-TM conversion:

$$\eta_{TE-TM} = \frac{P_{TM}}{P_{TE} + P_{TM}} \times 100\% \tag{3.16}$$

where P_{TE} and P_{TM} are the optical power of the TE- and TM-polarized modes at the output of the device. This relation is often expressed in a logarithmic scale through the extinction ratio (ER):

$$ER_{TE-TM}(dB) = 10\log_{10}\left(\frac{P_{TM}}{P_{TE}}\right) \tag{3.17}$$

Besides achieving a good mode conversion, the polarization converter should also have low insertion losses and a short conversion length (also called half-beat length), defined as the length at which a TE-polarized input is converted into a TM-polarized output, and vice versa. Finally, the operational bandwidth of a converter should be maximized. This parameter is typically defined either as the wavelength range with an extinction ratio within a 3 dB difference of the maximum ER, or as the wavelength range within which a 90% conversion efficiency is achieved.

There are several physical effects that can be used to implement polarization mode converters in integrated optics. Asymmetrical waveguides can be designed to guide two fundamental hybrid modes, that is, optical modes which are 50% TE-polarized and 50% TM-polarized, as shown by figure 3.6. When a TM- or TE-polarized input light reaches the polarization converter section of the waveguide, both hybrid modes are equally excited, and start propagating along the waveguide. Since the hybrid modes have different effective indexes and propagation constant, they are phase-shifted along the polarization converter. In particular, this phase shift periodically generates a 90º rotation of the polarization angle, effectively converting a TE-polarized input into a TM-polarized output and vice versa. The half-beat length ($L_{1/2}$), at which this 90º rotation occurs, is defined by:

$$L_{1/2} = \frac{\pi}{\Delta\beta} = \frac{\pi}{\beta_1 - \beta_2} \tag{3.18}$$

where β_1 and β_2 are the propagation constants of the two hybrid modes and $\Delta\beta$ is the difference between said propagation constants.

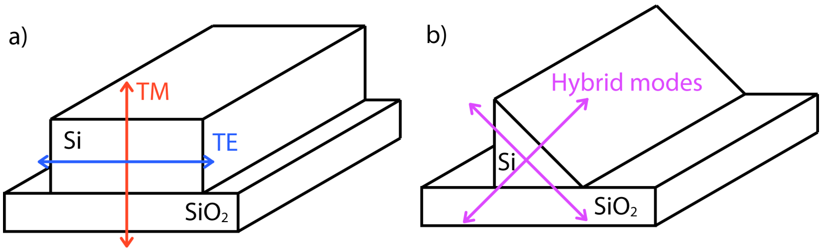

Figure 3.6. a) *Quasi-TM and quasi-TE modes guided in a silicon wire waveguide. Arrows indicate direction of principal electric field (E) component.* ***b)*** *Hybrid modes in a polarization rotator section.*

As shown in figure 3.7, several waveguide geometries can support rotated hybrid modes. First, sloped waveguide walls can efficiently induce the required waveguide asymmetry [Yamauchi’08, Brooks’06] (Figs. 3.7.a, 3.7.b). A theoretical conversion length of only 2 µm has been reported for a triangular waveguide [Yamauchi’08]. Second, multiple etch depths can be used to break waveguide vertical symmetry [Vermeulen’10, Zhang’10] (Figs. 3.7.c, 3.7.d). The shortest conversion length demonstrated with this configuration is 9 µm, with a conversion efficiency of 89% at a central wavelength of 1540 nm [Vermeulen’10].

However, these approaches have a significant drawback as they cannot be implemented with conventional lithographic techniques. Sloped waveguides require complex fabrication techniques with multiple steps, resulting in a poor control on the slope angle and surface quality. Multiple etch depths also imply an increased number of patterning and etching steps during the fabrication of the device, which can cause significant deviations from the ideal design due to small but unavoidable misalignments between etching steps.

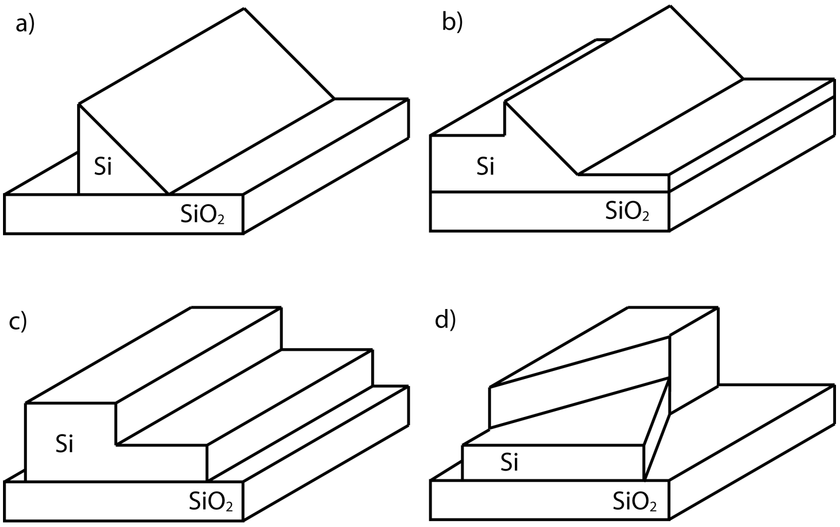

Figure 3.7. *Schematic examples of state-of-the-art polarization converters in Silicon-on-Insulator based on hybrid mode propagation.* ***a)*** *Triangular waveguide [Yamauchi'08].* ***b)*** *Waveguide with sloped sidewalls and different etch depths [Brooks'06].* ***c)*** *Asymmetrical waveguides with two etch depths [Vermeulen'10].* ***d)*** *Combination of vertical and horizontal waveguides [Zhang'10].*

As an alternative to hybrid mode propagation, polarization rotators based on light coupling between multiple waveguides were proposed [Yue'09], as shown in figure 3.8. With judicious design, polarization mode conversion can be achieved with waveguides of constant height and different widths [Liu'11, Dai'11], requiring only a single etch step. Polarization converters based on cross-polarization coupling effects have yielded theoretical conversion efficiency of 87% for a 44-µm-long waveguide [Liu'11], with conversion efficiency increasing to values close to 100% in a configuration with a conversion length of 100 µm [Dai'11].

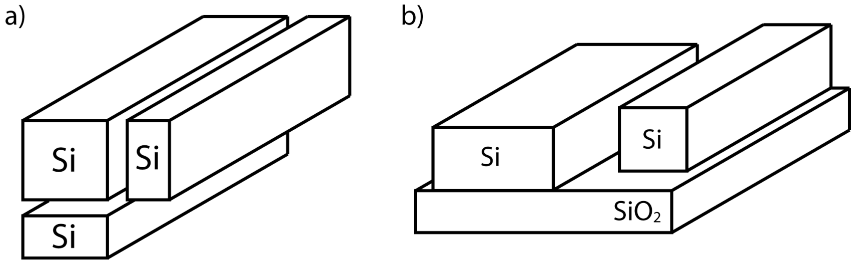

Figure 3.8. *Schematic examples of state of the art polarization converters in silicon-on-insulator based on mode coupling effect.* ***a)*** *Intermediate coupling to a multimode waveguide [Yue'09].* ***b)*** *Cross-polarization coupling [Liu'11, Dai'11].*

Finally, polarization converters based on hybrid mode guiding can also be implemented by inducing the asymmetry through etching one or more longitudinal trenches, as shown in figure 3.9. For trenches with dimensions smaller than the wavelength of the guided signal, an asymmetrical effective refractive index profile is achieved, mimicking the effect of a slanted sidewall. This concept has been implemented in III-V semiconductor integrated optics, obtaining a conversion length of 210 µm with a single trench [Kim'09], and 150 µm with multiple trenches [Holmes'06]. In both cases, conversion efficiency surpassed 95%.

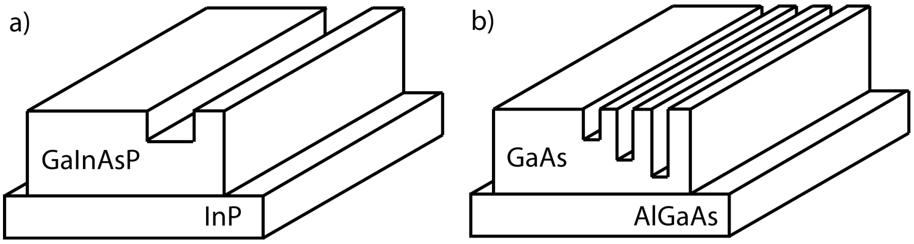

Figure 3.9. *Schematic structures of polarization converters in III-V semiconductor waveguides with **a)** single trench [Kim'09] and **b)** multiple trenches [Holmes'06].*

Although etching trenches with different dimensions typically require complex fabrication processes with multiple steps, certain combinations of trench depths and widths can be achieved in a single etching step by advantageously using the effect known as Reactive Ion Etch (RIE) lag [Holmes'06]. The RIE lag is observed as a partial etching of features with reduced dimensions, caused by the restrictions in the incident angles of the etching ions. As the feature width decreases, the number of ions incident upon the feature area is also reduced, hence decreasing the etch rate. For small features in which the RIE lag is apparent, the relation between etch width and depth can be calibrated, defining a plurality of trench dimensions that can be implemented with a single etch step.

In the light of the described state of the art, one of our goals was to implement an ultracompact and efficient polarization converter for the SOI platform, which could be readily fabricated and integrated in a wire waveguide. For this purpose, we explored an asymmetrical dual trench configuration, with trench widths and depths designed to be fabricated in a single etching step with the RIE lag effect (Fig 3.10). The design, fabrication and characterization of the polarization converter device is described in section 5.2.

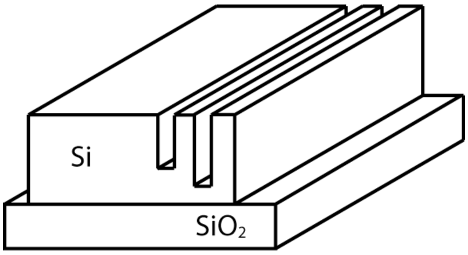

Figure 3.10. *Schematic structure of the fabricated polarization converter, implemented in a silicon wire waveguide with two asymmetrical longitudinal trenches [Section 5.2, Velasco'12].*

3.4. Waveguide multiplexers and demultiplexers

Compact and efficient multiplexers and demultiplexers are required for the development of commercially viable silicon photonics transceivers for wavelength division multiplexed (WDM) communications and interconnects [Doerr'06, Cheben'07b]. The established technology to perform this task in integrated optics are Arrayed Waveguide Gratings (AWG) [Pearson'00, Ohno'06, Dumon,'06, Liu'08b, Pathak'11] and waveguide echelle gratings [Bidnyk'06, Brouckaert'07, Feng'06]. When operating as a demultiplexer, both devices employ a passive wavelength dispersive element to spatially separate different wavelength channels, each into different output waveguides. When operating as a multiplexer, the wavelength dispersive element combines different wavelength channels, each coupled from a separate waveguide, into a single output waveguide with the multiplexed (multi-wavelength) signal.

In AWGs, the wavelength dispersive element is an array of waveguides, typically with linearly increasing lengths across the array, as shown in figure 3.11. This configuration results in a wavelength-dependent relative phase difference between adjacent waveguides at the array output aperture. Consequently, each channel is focused at a different position of the focal curve. Receiver waveguides are typically located at the Rowland circle [Rowland'82] to minimize wavefront aberrations. Light is coupled in and out of the waveguide array through input and output slab waveguide combiners respectively.

AWG implemented in SOI benefit from a small waveguide bend radius and a high mode confinement due to the high refractive index contrast between the silicon waveguide core and SiO_2 cladding, resulting in substantially more compact devices compared to AWGs in glass. However, the high refractive index contrast implies a larger optical intensity at the waveguide boundaries, rendering the guided modes more susceptible to fabrication imperfections, and particularly, to the roughness of the waveguide sidewalls. This results in deviations from the theoretically constant optical path increment between adjacent waveguides, i.e. phase errors and output wavefront distortions, and ultimately deteriorating the crosstalk of the device.

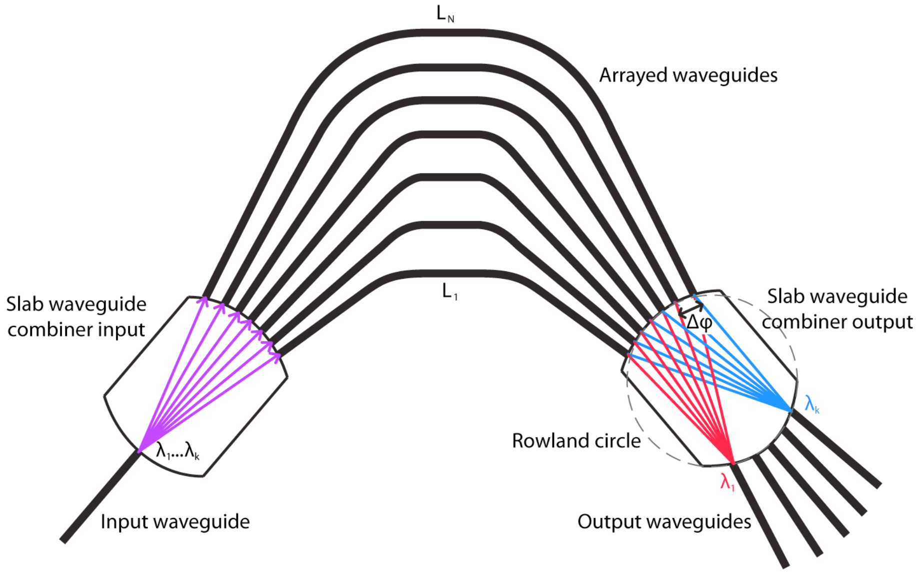

Figure 3.11. *Arrayed Waveguide Grating (AWG) demultiplexer. Input light is coupled from input waveguide through input combiner into an array of waveguides with linearly increasing optical paths. As a result of the phase difference between the outputs of adjacent waveguides, the focusing points of the central wavelengths of the channels are spatially separated along the Rowland circle.*

Waveguide echelle grating demultiplexers, schematically presented in figure 3.12, are a more compact alternative to AWGs. They are implemented with diffraction gratings as the wavelength dispersive element, focusing each channel in a different position along the Rowland circle, where different wavelength channels are intercepted by an array of output waveguides. Other alternative multiplexing devices include cascaded Mach-Zehnder interferometers and ring resonators filters [Xia'07], both their transfer functions are highly sensitive to fabrication deviations. This limitation can be overcome by using active (tunable) ring resonators [Han-Yong'08, Sherwood'08, Zheng'10, Wen'11], but the inclusion of active elements implies a greater fabrication complexity and cost, as well as the incorporation of control electronics which increase operation and fabrication complexity.

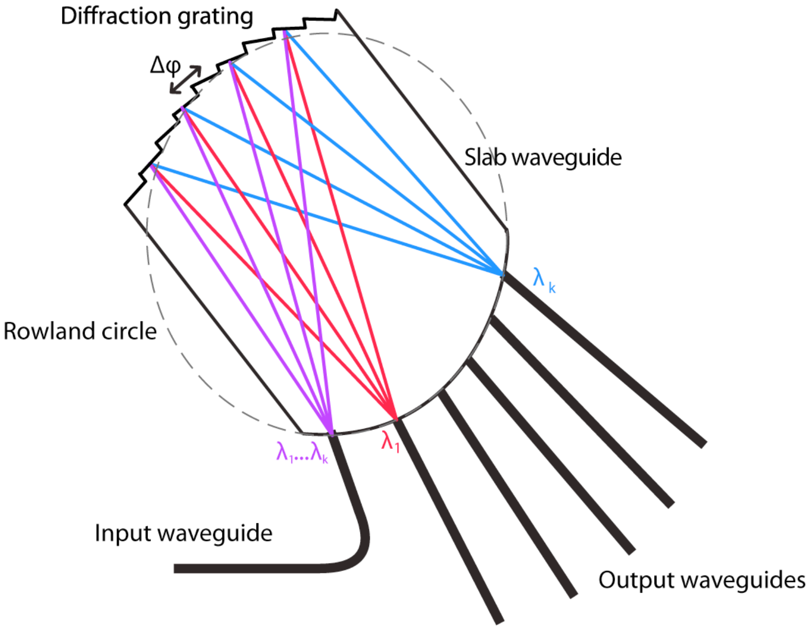

Figure 3.12. *Waveguide echelle grating demultiplexer. Input light is diffracted by the etched waveguide grating in a reflecting geometry. After propagation through the slab waveguide, different wavelength channels are coupled into the output waveguide array. Concave diffraction gratings acts as the wavelength dispersion and focusing element.*

In the works presented in this thesis, we propose an alternative multiplexer/ demultiplexer configuration for the SOI platform which benefits from the reduced footprint of echelle gratings while at the same time providing a higher efficiency and wavefront apodization. In particular, the device is based on a blazed and apodized diffraction grating etched in the sidewall of a curved input waveguide, as schematically shown in figure 3.13. The wavelength dispersion properties are similar as in an echelle grating device, and waveguide channels are spatially separated along the Rowland circle. However, and in contrast to echelle gratings, sidewall grating can be apodized without incurring additional losses, since the optical power that is not diffracted at a specific section of the grating and remains in the waveguide and is diffracted by further sections of the diffraction grating.

An important advantage of the proposed device compared to AWGs is an increased tolerance to fabrication variations and errors. In AWGs, the accumulated phase error of each waveguide of the array is different for different waveguides, increasing the relative error between adjacent waveguides. On the contrary, in a sidewall grating demultiplexer, the light (waveguide mode) follows a common path along the input waveguide as it is progressively diffracted, therefore the phase error between two adjacent facets of the grating does not accumulate.

The experimental demonstration of this device, as well as a detailed explanation of the operation principles is discussed in section 5.3. The device is 100 µm × 160 µm, the smallest size yet reported for a demultiplexer of comparable performance.

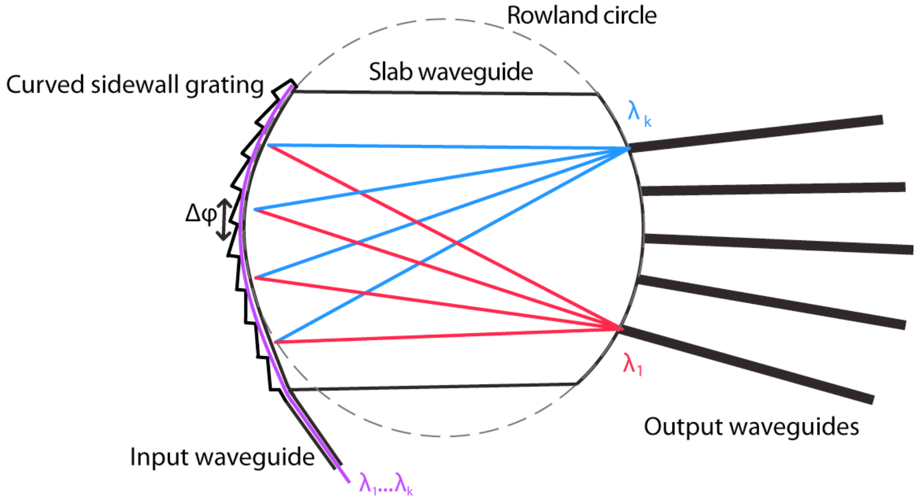

Figure 3.13. *Sidewall grating demultiplexer. Input light is guided along a curved waveguide and progressively diffracted by a diffraction grating etched on its sidewall. The diffraction process is wavelength-dependent, resulting in the focusing of each wavelength in a different position along the Rowland circle [Rowland'82].*

Furthermore, the proposed demultiplexer configuration based on a curved sidewall grating was also implemented as a passband filter by using a single output waveguide. The central operational wavelength of the device is selected by judiciously designing the grating period and the position of the output waveguide along the Rowland circle. Furthermore, the reduced footprint and comparatively low intrinsic loss of the device enables cascading several filtering stages for reduced crosstalk and enhanced spectral selectivity. The design, fabrication and characterization of this sidewall grating photonic filter is discused in section 5.4.

3.5. Goals of the present work

The main goals of this thesis regarding silicon-based photonic devices is to design, fabricate and characterize four distinct devices for wavelength and polarization management, all of them presenting highly competitive performances in remarkably compact footprints:

- A SHFT spectrometer, with an array of Mach-Zehnder interferometers comprising silicon wire waveguides with microphotonic spirals for increased spectral resolution in a compact footprint.

- An ultra-compact polarization converter, implemented by etching two subwavelength asymmetrical trenches in a silicon wire waveguide.
- A sidewall grating demultiplexer, with apodized and chirped diffraction grating for improved coupling to the output waveguides, reduced crosstalk and apodization advantage
- A sidewall grating bandpass filter, with cascaded filtering stages for enhanced suppression of the rejection bands.

The design, fabrication and characterization of these devices is shown in chapter V, with further details on the experimental methods in Annex A.

IV

Published results on sol-gel glass based photonic devices

This chapter presents the results of this thesis on the development of holographic filters in photopolymerizable glasses, as published in the following peer reviewed journal papers:

4.1. Photopolymerizable organically modified holographic glass with enhanced thickness for spectral filters (Journal of Applied Physics).

4.2. Photopolymerizable glasses incorporating high refractive index species and ionic liquid: A comparative study (Journal of Applied Physics).

JOURNAL OF APPLIED PHYSICS **113**, 033101 (2013)

Photopolymerizable organically modified holographic glass with enhanced thickness for spectral filters

A. V. Velasco,[1] M. L. Calvo,[1] and P. Cheben[2]
[1]*Department of Optics, Faculty of Physics, Complutense University of Madrid, 28040 Madrid, Spain*
[2]*National Research Council Canada, Ottawa, Ontario K1A 0R6, Canada*

(Received 7 November 2012; accepted 21 December 2012; published online 15 January 2013)

A novel formulation and synthesis method to overcome the thickness limitations in samples of photopolymerizable glasses with high refractive index species is presented. The reported method allows the recording of volume holographic diffraction gratings in samples of ~500 μm thickness with a high optical quality and low scattering. Holographic grating recording is performed in a single coherent light exposure step, resulting in volume gratings of high optical quality. A holographic notch filter implemented in a 500 μm thick photopolymerizable glass with a spectral bandwidth below 0.3 nm and an excellent filter extinction ratio of <-27 dB is also demonstrated. *© 2013 American Institute of Physics*. [http://dx.doi.org/10.1063/1.4775787]

I. INTRODUCTION

Holographic filters are fundamental components used in a variety of applications, such as microscopy,[1] pattern recognition,[2,3] beam transformation,[4] chemical spectrum identification,[5] and general narrowband filtering,[6] to name a few. In particular, holographic recording materials are ideal candidates for implementing narrow-band notch filters based on Bragg diffraction gratings,[7,8] often used for Rayleigh line suppression in Raman spectroscopy.[9–11] For the development of high-performance filters with a narrow stop-band and a high extinction (central wavelength rejection) ratio, a holographic medium with a high dynamic range, superior optical quality, and large thickness is required.[12]

Photopolymerizable materials have shown excellent performance in terms of dynamic range and optical quality.[13,14] However, organic polymeric binders used in holographic polymers are typically limited in thickness to less than a few hundred micrometers. Also, dimensional changes induced by light exposure (material shrinkage) or temperature variations can distort the hologram and alter the designed spectral response of the filter.

A new class of holographic material based on organically modified sol-gel glass was developed by Cheben *et al.*[15,16] The material is an organic-inorganic photosensitive glass comprising a silicate sol-gel matrix which incorporates monomeric and photoinitiator species. When exposed to an interference pattern at an actinic wavelength, the photoinitiator is activated and the polymerization of the free monomers takes place. Additionally, a diffusion of monomer takes place from the dark towards the illuminated regions where the monomer concentration is depleted.[15] The refractive index modulation Δn of up to 5.6×10^{-3} and diffraction efficiencies close to 100% were reported for this type of material.[16] The refractive index modulation was subsequently enhanced to ~0.01 by incorporating a zirconium-based high refractive index species (HRIS) to the photopolymerizable glass.[17] Zirconium isopropoxide $Zr(O^iPr)_4$ high index species was introduced at a molecular level to minimize scattering loss. The incorporation of ZrO_2 nanoparticles to polymeric films has also been demonstrated to increase material dynamic rage.[18] Photopolymerizable glasses have also proven to withstand a high pulsed laser energy without degradation of the recorded diffraction gratings.[19] The high dynamic range and optical quality of photopolymerizable glasses make them candidates for volume holographic recoding.[20–22] However, in order to implement holographic filters with high spectral selectivity, a photopolymerizable holographic recording material with thickness of the order of 500 μm or more is required.

In this paper, we present a new formulation and synthesis method for a photopolymerizable glass incorporating HRIS that allows the fabrication of samples with typical thickness of about 500 μm, as required for applications in holographic filters with high spectral selectivity. The dependence of the photomaterial performance on sample thickness is analyzed, including the angular selectivity, dark diffusion, scattering, and optical quality. A narrowband notch filter implemented in a 500-μm-thick photopolymerizable glass is presented.

The paper is organized as follows: Sec. II presents the novel formulation and synthesis procedure for preparation of samples with increased thickness. Section III is dedicated to the experimental characterization of the fabricated samples. In particular, characteristics of samples with thickness ranging from 50 to 500 μm are compared and the relation between sample thickness and holographic performance is analyzed. In Sec. IV, we present a notch filter implemented in a 500-μm-thick photopolymerizable glass. Discussions and conclusions are presented in Sec. V.

II. SAMPLES PREPARATION

In order to overcome the thickness limitation of the photopolymerizable glass samples with HRIS, some modifications were introduced to the synthesis method previously disclosed.[17] Here, we summarize the modified method, with more details described in the Appendix. First, the concentration of HRIS in the samples was reduced compared to Ref. 17 to minimize tendency of cracking in thick samples.

In order to minimize the consequential decrease in dynamic range (Δn) and prolonged gelation times, we chose the following molarity of $Zr(O^iPr)_4 \cdot {}^iPrOH$: 0.75 mmol and MA: 3.5 mmol, while maintaining the other component concentrations as disclosed in Ref. 17.

Second, instead of the microscope slides, we used Petri dishes to contain an increased amount of the sol-gel solution. Once the solution was cast on the dish, each sample was individually sealed using wax paper and stored in an oven with a controlled temperature of 40 °C and a relative humidity of 25%. Samples with thicknesses ranging from 50 to 500 μm were prepared. The process lasted up to 14 days for the thickest samples. As the gelation evolved, oxygen flow was progressive allowed to the sample by making additional small holes in the wax paper sealing, in order to avoid abrupt changes in the environmental conditions which could result in cracking and surface deterioration.

III. SAMPLES HOLOGRAPHIC CHARACTERIZATION

A. Holographic recording and characterization setup

Transmission volume phase holographic gratings (VPHG) were recorded in the photopolymerizable glass samples by interference of two coherent *s*-polarized beams using a Mach-Zehnder interferometer with a single-frequency solid state laser at a wavelength of 532 nm (Oxxius 532 S). Beams with equal intensities of 7.5 mW/cm^2 were used for maximal visibility of the interference fringes. A spatial frequency of 500 lines/mm was obtained using incidence angles of ±7.9° from the sample normal. Samples were stabilized by exposure to incoherent light after the holographic gratings recording.

A non-actinic probe beam from a He-Ne laser at 632.8 nm wavelength with an output power of 0.5 mW (Newport ULMTILT) was used for real-time monitoring of the evolution of the grating formation. Angular selectivity of the recorded gratings was characterized by placing the sample on a high-precision rotation platform and measuring the 1st Bragg diffraction order using the He-Ne laser. Refractive index modulation values were obtained by fitting the measured angular selectivity curve to the theoretical expression from Kogelnik's coupled wave theory for light diffraction by dielectric transmission volume gratings[23]

$$\Delta n = 2\, n_0\, Cos\,(\vartheta_0)\, Sin(\vartheta_0)\, T \frac{ArcSin(\sqrt{\eta})}{\sqrt{\pi^2 - \left(ArcSin(\sqrt{\eta})\right)^2}}, \quad (1)$$

where n_o is the refractive index of the photomaterial prior to holographic exposure, θ_0 is the Bragg angle, T is the sample thickness, and η is the diffraction efficiency. The latter was calculated as $\eta = P_{-1}/P_0$, where P_{-1} is the power in the −1st diffraction order and P_0 is the power in the probe beam incident on the sample.

B. Diffraction efficiency and angular selectivity

Figure 1 shows the angular selectivity curves of three diffraction gratings with thicknesses 150 μm, 260 μm, and 500 μm. It can be observed that the angular selectivity curves fit well to the theoretical response near Bragg's angle, confirming that the gratings were efficiently recorded in the entire volume of the sample. The increase of angular selectivity with sample thickness is observed, as expected. For the 500 μm thick grating, a 50% (3 dB) roll-off is achieved for a 0.15° detuning from the Bragg angle (9.4° for the read-out laser at 632 nm). The ratio between the maximum diffraction efficiency and the intensity of secondary lobes is only 0.04 (−14 dB).

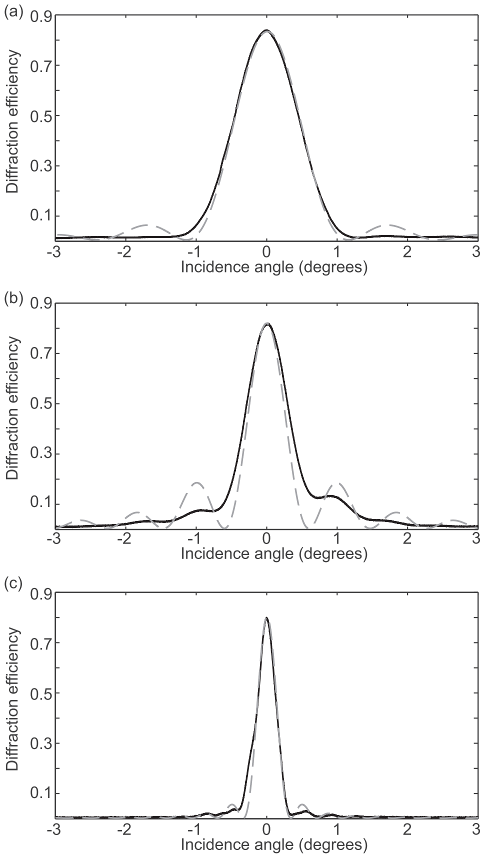

FIG. 1. Measured angular selectivity (solid) and theoretical fitting (dashed) of volume holographic gratings in a photopolymerizable glass of thickness: (a) 150 μm, (b) 260 μm, and (c) 500 μm. Grating of spatial frequency 500 lines/mm were recorded with a solid-state laser at 532 nm and monitored with a non-actinic He-Ne laser at 632 nm. Incidence angles are measured from the Bragg angle.

In Fig. 1, the angular selectivity curve for the 500 μm diffraction grating corresponds to a diffraction efficiency of 80% at Bragg's angle. This specific value is limited by the overexposure, and higher diffraction efficiency values close to 100% theoretical limit can be achieved. This is shown in Figure 2, where the evolution of the diffraction efficiency is plotted after the recording pulse with a maximum diffraction efficiency of 99% approximately 7 s following the recording pulse. As a result of the high dynamic range of the sample,

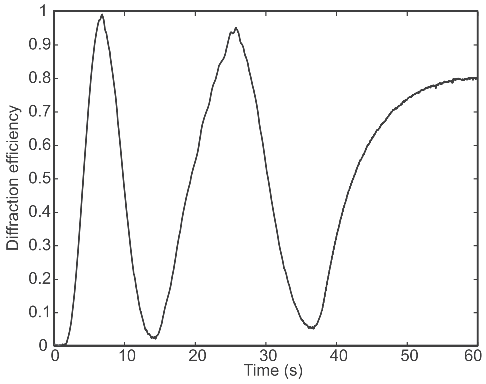

FIG. 2. Evolution of the diffraction efficiency at Bragg's angle of a 500 μm thick holographic grating after a single recording pulse of 15 mJ/cm^2 at 532 nm wavelength. Grating evolution is monitored with a non-actinic beam from a He-Ne laser of 632 nm wavelength.

the refractive index modulation keeps increasing after this point, resulting in the overmodulation and a corresponding decrease in diffraction efficiency. The evolution of the grating formation is further discussed in Sec. III C.

Since diffraction efficiencies close to 100% can be readily obtained, and given the high thickness and dynamic range of the synthesized samples, highly selective holographic filters, both angularly and spectrally, can be implemented in our photopolymerizable glass. Additionally, the recording of gratings with spatial frequencies exceeding 4000 lines/mm was demonstrated in our material.[24] This provides an additional degree of freedom to further increase the spectral and angular selectivity of our grating filters, if demanded by specific applications.

C. Dark diffusion and sensitivity

As a result of the polymerization of the monomer species in the illuminated regions, spatial nonuniformities in the distribution of the monomer and HRIS are induced during the exposure in our material. These concentration gradients trigger a migration of the monomer and HRIS from monomer/HRIS rich (dark fringes) regions to monomer/HRIS depleted regions (bright fringes) of the interference pattern. As the diffused species are polymerized, the refractive index modulation of the grating is further increased. The diffusion, which occurs in the absence of light, and the subsequent Δn evolution, is referred to as "dark diffusion," and stops when the composition reaches its chemical equilibrium. In the case of the photopolymerizable glass with HRIS, dark diffusion mechanism can be modeled using the weighted sum of two exponential functions[25,26]

$$\Delta n(t) = C_M[1 - \exp(-t/\tau_M)] + C_{Zr}[1 - \exp(-t/\tau_{Zr})], \quad (2)$$

where exponential weight factors, C_M and C_{Zr}, account for the partial contributions of monomer and Zr-based HRIS components, respectively, to the overall Δn value. The diffusion time constants τ_M and τ_{Zr}, account for the different diffusion speeds of the two respective species, namely $\tau_M < \tau_Z$.

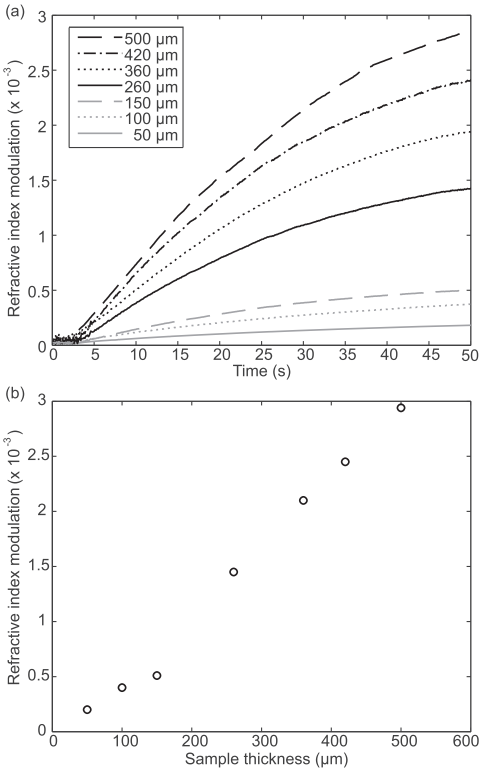

FIG. 3. (a) Measurement of dark diffusion of monomer and HRIS species for sample of different thicknesses. 1 s pulse at 532 nm and 15 mW/cm^2 flux was used for the recording of gratings with spatial frequency of 500 lines/mm. Δn was measured with a He-Ne laser at 632 nm. (b) Measured refractive index modulation corresponding to a 1 s recording pulse of 15 mW/cm^2.

This double-exponential behaviour is observed in Fig. 3(a), which shows the temporal evolution of Δn after a recording pulse for several gratings with thicknesses ranging from 50 to 500 μm. The samples show a high sensitivity, which allows diffraction gratings to be recorded with a single pulse of 1 s and 15 mW/cm^2. An induction period of 2 to 3 s with a comparatively slow response is followed by a fast evolution with Δn increasing as in Eq. (2). The curves slopes are proportional to the Δn resulting from a single exposure at a given energy. This parameter increases progressively with the thickness of the sample, allowing to reach high refractive index modulations with low exposure light powers, as it is shown in Fig. 3(b).

Time constants τ_M and τ_{Zr} are found to be similar for the analyzed samples, as the speed of the diffusion is determined by the composition of the glass matrix with little influence of the sample thickness. By fitting the experimental curves to Eq. (2), average values of $\tau_M = 5.1 \pm 0.8$ s and $\tau_{Zr} = 25.7 \pm 1.2$ s were obtained, showing a stable dark diffusion behavior in the analyzed thickness range (50 to 500 μm). The measured diffusion time values are also in good agreement with previously published results for photopolymerizable glasses incorporating HRIS.[25,26]

D. Scattering and optical quality

The samples under investigation presented a high optical quality with low scattering. Residual noise grating formation angular selectivity measurements are presented in Fig. 4, with a negligible scattering penalty as the sample thickness increases. In these measurements, the build-up of a noise grating would be shown as a dip in diffraction efficiency near Bragg resonance, but no such dip is observed for our samples, indicating high optical quality and low scattering. Furthermore, diffraction efficiency variations in the analysed angular range are within a 1% range, even for the thickest samples, demonstrating the low scattering of the samples.

Figure 5 shows the He-Ne readout beam intensity distribution in (a) free space, (b) transmitted through a 500 μm thick unexposed photopolymerizable glass; (c) transmitted through the same 500 μm thick photopolymerizable glass after exposure to 15 mW/cm^2 1-s pulse. Strong speckle is initially observed (Fig. 5(c)), caused by light scattering at sample surface irregularities. We mitigated the surface scattering by using a refractive index matching liquid (Norland Index Matching Liquid 150, $n = 1.52$), as it is shown in Fig. 5(d), achieving a good beam quality.

IV. HOLOGRAPHIC NOTCH FILTER

The available thickness range of our photopolymerizable glasses allows the implementation of high-quality filters for various applications. As an example, a holographic notch filter was implemented in a 510-μm-thick sample, which is the upper thickness limit that was achieved with the described synthesis method without resulting in fractures or uneven gelation. Samples with thickness in the 0.5–1 cm range could likely be achieved by judiciously tailoring the preparation process and by reducing their HRIS concentration. The filter was recorded by interference of two coherent *s*-polarized beams from a solid-state laser at 532 nm with an incidence angle of 48.1°, yielding a grating spatial frequency of 2800 lines/mm. A single pulse exposure (3 mJ/cm^2 flux, 1 s duration) was used to achieve maximal diffraction efficiency and a high quality grating. Figure 6 shows the experimental measurement of the spectral response of the filter, characterized using a He-Ne laser at 632.8 nm with incidence angles centred at the Bragg angle of 62.3°. A −3 dB bandwidth of 0.3 nm is achieved, with a maximum suppression of −27.5 dB and a flat response for off-Bragg wavelengths with minimal ripple (<−0.1 dB). The central wavelength of the device can be readily tuned either by modifying the operational angle of incidence or by adjusting the inter-beam during the recording of the filter.

It is obvious that the same device can also be used as a passband filter for the diffracted beam, with the same bandwidth as the notch filter for the transmitted beam. An

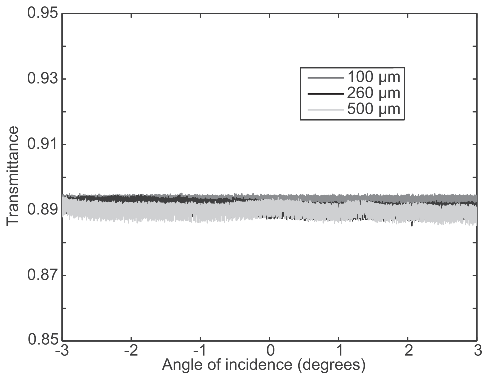

FIG. 4. Noise grating angular selectivity measurements for samples of different thicknesses. The samples were exposed to a coherent *s*-polarized single beam of 532 nm wavelength and 15 mW/cm^2 flux for 1 s and read-out by a non-actinic He-Ne laser at 632 nm.

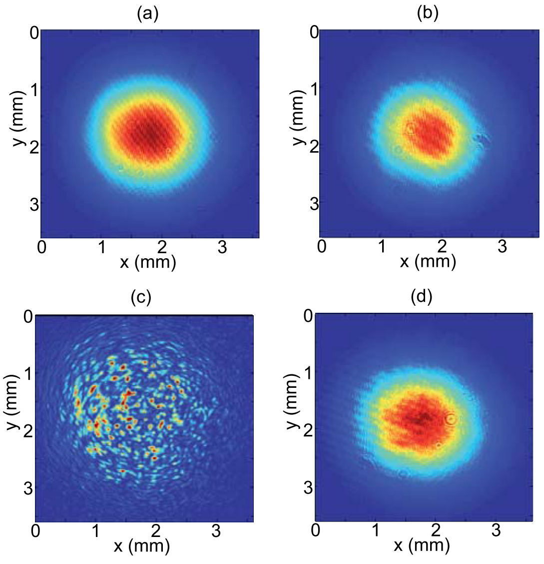

FIG. 5. Beam profiles of a He-Ne laser at 632 nm (a) in free space; (b) transmitted through a 500 μm thick unexposed photopolymerizable glass; (c) transmitted through the same 500 μm thick photopolymerizable glass after exposure to 15 mW/cm^2 1-s pulse; (d) as in (c) but after applying a refractive index matching liquid to mitigate surface scattering. All images were taken with a Spiricon digital camera (Ophir) with a pixel size of 4.4 μm × 4.4 μm.

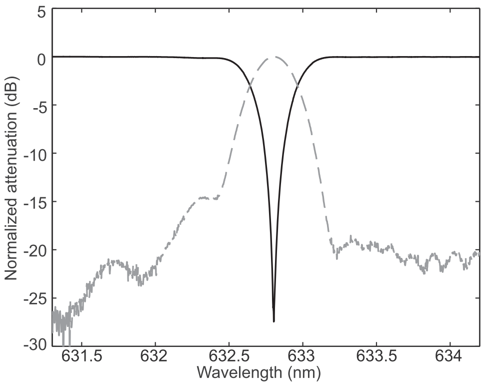

FIG. 6. Holographic filter spectral response for the transmitted beam (black, notch filter) and the diffracted beam (dashed grey, bandpass filter).

extinction ratio exceeding −20 dB is achieved, with sidelobes level of −15 dB (Fig. 6, grey dashed curve). The limiting factor which determines this sidelobe level is the theoretical angular selectivity curve of a diffraction grating recorded by interference of two plane wavefronts, as defined by Kogelnik's expression.[23] Sidelobe level could be potentially optimized by judiciously tailoring the shape of the recording beams with a spatial modulator. Absorption losses are negligible, with the main loss factor being reflections at the facets of the device (∼4% per facet for normal incidence), which if required can be compensated using an antireflective coating. Overall, the filter presents a very good optical quality and low scattering for both transmitted and diffracted beams, similar to those shown in Sec. III.

V. CONCLUSIONS

We reported a modified composition and method for developing photopolymerizable glasses incorporating HRIS with large thickness (∼500 μm). Fabricated samples have shown low scattering, and high diffraction efficiency and dynamic range, allowing to tailor holographic filters with high optical quality and selectivity, both angularly and spectrally. The high sensitivity of the photomaterial with HRIS and enhanced thickness allows to record the filter with a single short light pulse. The grating is formed after exposure by internal diffusion of the monomeric species and HRIS inside the glass matrix, thus preventing surface roughness to be transmitted to the grating by subsequent light pulses and reducing the resulting scattering. A high-quality narrowband notch filter has been fabricated with the disclosed method, demonstrating the potential applications of these photopolymerizable glasses for various purposes such as as spectrometry, microscopy, and optical instrumentation, including high power instrumentation due to their high laser damage threshold.

ACKNOWLEDGMENTS

We are indebted to F. Del Monte (Institute for Materials Science, Spanish Research Council) for helpful discussions. Financial support from the Spanish Ministry of Science and Innovation (MICINN) under Grant Nos. TEC2008-04105 and TEC2011-23629 is acknowledged.

APPENDIX: SAMPLE PREPARATION

The chemical procedure for the synthesis of the photopolymerizable glass incorporating HRIS was reported in detail in Ref. 17; here we summarize the basic steps.

The silica sol is prepared by acid hydrolysis of glycidoxypropyltrimethoxysilane (GPTMS) and tetraethylorthosilicate (TEOS). The molar ratio between GPTMS and TEOS is selected to minimize the shrinkage of the photopolymerizable glasses after light exposure.[27] Molarities of the hydrochloric acid solution are also selected to ensure all water is consumed during the hydrolysis. After 10 min of vigorous stirring, a solution of IRGAGURE-784 photosensitizer in Phenoxyethyl acrylate (POEA) is added. A solution of zirconium isopropoxide isopropanol complex in methacrylic acid is added to the mixture after an additional 10 min. The resulting solution is filtered with a 0.2 μm millipore filter.

Films of thickness up to 500 μm were obtained by casting the filtered solution on glass Petri dishes. Samples were sealed with wax paper and left to dry in the dark at a controlled temperature of 40 °C for 14 days prior to hologram recording. Oxygen flow to the sample was progressively increased by performing small holes in the wax paper sealing. A stable relative humidity of 25% was maintained during the gelation process.

[1] G. Barbastathis, M. Balberg, and D. J. Brady, Opt. Lett. **24**, 811 (1999).
[2] H. Fujii, S. P. Almeida, and J. E. Dowling, Appl. Opt. **19**, 1190 (1980).
[3] M. Fleisher, U. Mahlab, and J. Shamir, Appl. Opt. **29**, 2091 (1990).
[4] M. Quintanilla and A. M. de Frutos, Appl. Opt. **20**, 879 (1981).
[5] L. Cao and C. Gu, Appl. Opt. **48**, 6973 (2009).
[6] G. A. Rakuljic and V. Leyva, Opt. Lett. **18**, 459 (1993).
[7] C. L. Schoen, S. K. Sharma, C. E. Helsley, and H. Owen, Appl. Spectrosc. **47**, 305 (1993).
[8] C. Moser and F. Havermeyer, Appl. Phys. B **95**, 597 (2009).
[9] C. Xie, M. A. Dinno, and Y. Li, Opt. Lett. **27**, 249 (2002).
[10] M. M. Carrabba, K. M. Spencer, C. Rich, and D. Rauh, Appl. Spectrosc. **44**, 1558 (1990).
[11] M. J. Pelletier and R. C. Reeder, Appl. Spectrosc. **45**, 765 (1991).
[12] B. Karsten, F. Havermeyer, L. Wenhai, M. Christophe, and D. Psaltis, "Holographic filtres," in *Photorefractive Materials and Their Applications 3*, edited by P. Günter and J.-P. Huignard (Springer, Berlin, 2007), pp. 295–319.
[13] G. T. Sincerbox, *Current Trends in Optics*, edited by J. C. Dainty (Academic, London, 1994), Chap. 14, Vol. 2.
[14] R. A. Lessard and G. Manivannan, Proc. SPIE **2405**, 2 (1995).
[15] P. Cheben, T. Belenguer, A. Nuñez, F. del Monte, and D. Levy, Opt. Lett. **21**, 1857 (1996).
[16] P. Cheben and M. L. Calvo, Appl. Phys. Lett. **78**, 1490 (2001).
[17] F. Del Monte, O. Martínez-Matos, J. A. Rodrigo, M. L. Calvo, and P. Cheben, Adv. Mater. **18**, 2014 (2006).
[18] K. Omura and Y. Tomita, J. Appl. Phys. **107**, 023107 (2010).
[19] M. P. Hernández-Garay, O. Martínez-Matos, J. G. Izquierdo, M. L. Calvo, P. Vaveliuk, P. Cheben, and L. Bañares, Opt. Express **19**, 1516 (2011).
[20] M. Haw, Nature **422**, 556 (2003).
[21] D. Psaltis and F. Mok, Sci. Am. **273**, 70 (1995).
[22] F. Mok, G. Zhou, and D. Psaltis, "Holographic read-only memory," in *Holographic Data Storage*, edited by H. J. Coufal, D. Psaltis, and G. T. Sincerbox (Springer, Berlin, 2000), pp. 399–407.
[23] H. Kogelnik, Bell Syst. Tech. J. **48**, 2909 (1969).
[24] O. Martínez-Matos, J. A. Rodrigo, M. L. Calvo, V. Hevia-Martín, and P. Cheben, Opt. Mem. Neural Networks **18**, 21 (2009).
[25] O. Martínez-Matos, M. L. Calvo, J. A. Rodrigo, P. Cheben, and F. del Monte, Appl. Phys. Lett. **91**, 14115 (2007).
[26] A. V. Velasco, M. P. Hernández-Garay, M. L. Calvo, P. Cheben, and F. Del Monte, J. Appl. Phys. **109**, 053106 (2011).
[27] G. Ramos, A. Alvarez-Herrero, T. Belenguer, F. del Monte, and D. Levy, Appl. Opt. **43**, 4018 (2004).

JOURNAL OF APPLIED PHYSICS **109**, 053106 (2011)

Photopolymerizable glasses incorporating high refractive index species and ionic liquid: A comparative study

A. V. Velasco,[1,a)] M. P. Hernández-Garay,[1] M. L. Calvo,[1] P. Cheben,[2] and F. del Monte[3]
[1]*Department of Optics, Faculty of Physics, Complutense University of Madrid, 28040 Madrid, Spain*
[2]*Institute for Microstructural Sciences, National Research Council Canada, Ottawa, Ontario K1A 0R6, Canada*
[3]*Institute for Materials Science, Spanish Research Council, 28049 Cantoblanco, Spain*

(Received 10 November 2010; accepted 6 January 2011; published online 8 March 2011)

Three different holographic photomaterials belonging to the class of photopolymerizable glasses have been synthesized using sol-gel techniques, and characterized with the purpose of a comparative study. Their behavior is analyzed in terms of achieved refractive index modulation, dark diffusion mechanism, diffraction efficiency and optical quality; in order to determine their suitability for different holographic applications. © *2011 American Institute of Physics*. [doi:10.1063/1.3553840]

I. INTRODUCTION

The requirements of synthesis, characterization and development of recording materials exhibiting high dynamic range, high photosensitivity, and excellent optical quality, is still a challenging achievement in the field of photomaterials[1,2] and within the holographic data storage techniques.[3–7] The fulfillment of these requirements shown by photopolymerizable materials has generated an important focus of attention on this family of holographic composites.[8–10] As a result of the investigation in these materials, the so named photopolymerizable glasses developed with sol-gel techniques were first introduced in 1996.[11]

These hybrid organic-inorganic photosensitive glasses incorporate monomeric and photoinitiator species in a silicate matrix. When exposed to an interference pattern at an appropriate wavelength, the photoinitiator is activated and the polymerization of the free monomers takes place. The size increase of the resulting polymeric chains eventually hinders their diffusion within the glass matrix, thus making this distribution permanent after the recording. Additionally, after the polymerization, in regions of the interference pattern exposed to a higher light intensity distribution, the monomer concentration is depleted, resulting in a diffusion of the remaining monomer from the darker fringes to the illuminated ones.

As a result of this combined process of polymerization and diffusion, refractive index differences Δn up to 5.6×10^{-3} between dark and illuminated regions of the interference pattern have been achieved.[12]

These results have been further improved by incorporating in the photopolymerizable glass High Refractive Index Species (HRIS).[12,13] In order to minimize scattering, zirconium isopropoxide $Zr(O^iPr)_4$ was introduced at a molecular level to act as the HRIS, using methacrylic acid as a chelating agent to slow its hydrolysis. With the addition of the HRIS, refractive index modulations (Δn) up to 10^{-2} are achieved. The relation between the incorporation of ZrO_2 nanoparticles to polymeric films and the resulting recording sensitivity and gelation point have also been demonstrated[14] as well as the aforementioned Δn increase.

In another aspect of the investigation in photomaterials, and given the hazardous nature of some of the involved components, such as the monomer and sol-gel precursors, the introduction of nonvolatile substances in the design, synthesis and applications, is having a primary interest for introducing sustainable chemical processes. In particular, Ionic liquids (ILs) have recently focused great attention, also as an alternative to solvents in chemical reactions.[15,16] ILs are organic salts having an ionic structure (hence the name) and which are liquid at ambient temperature and exhibit hydrophilic behavior. Moreover, although ILs may be hazardous for the environment in some cases (in particular in aquatic environments), their extreme low nonvolatility prevents the evaporation of toxic substances which is typical of other solvents. Additionally, ionic liquids have shown to improve polymerization rates,[17–19] an advantage which has already been exploited in holographic materials based on photopolymers.[20] In the preliminary studies done by Lin *et al.*, the incorporation of IL to a photosensitive polymerizable material resulted in an increase of the sensitivity, spatial resolution and refractive index modulation. The strong diffusion mechanism which follows the light exposure, enhanced by the presence of IL, allowed to reach diffraction efficiencies up to 34% for a thin hologram (Raman-Nath regime,[21] 10 μm grating thickness). Holographic materials incorporating IL have also been used in the development of optical diffusers[22] as the concentration of IL can be varied to regulate their light diffusion property.

In this paper, and encouraged by the previous mentioned results, we present a comparative study among three alternative formula for the composition of a photopolymerizable glass: (1) the formula that contains HRIS, already studied by us,[23–26] (2) incorporation of IL to the previous formula, and (3) exclusion of the HRIS in the composition while maintaining the IL as a component. A comparative study of the various physical performances obtained is presented.

The paper is organized as follows: Section II presents the results obtained with the photopolymerizable glass containing the HRIS. In particular, the angular selectivity and

---

[a)] Electronic mail: avillafr@pdi.ucm.es refractive index modulation are studied along with an analysis of the structure of the holographic gratings with Scanning Electron Microscope (SEM). The dark diffusion mechanism is also discussed. Section III is dedicated to the results obtained for the new formula of the photopolymerizable glass incorporating IL. In Sec. IV we present the results for the new formula incorporating both the HRIS and the IL and with studies that provides comparative analysis with the results presented in previous sections. Discussions and conclusions are presented in Sec. V.

II. PHOTOPOLYMERIZABLE GLASS INCORPORATING HIGH REFRACTIVE INDEX SPECIES

A. Synthesis

In previous publications,[13] we have disclosed both the synthesis and the characterization analysis of the photopolymerizable glass incorporating HRIS. As an antecedent, this material has already shown strong performances, reaching Δn of up to 10^{-2} and diffraction efficiencies close to 100% with a good optical quality. In particular, the applications for the implementation of transmission volume phase holographic gratings (VPHG) with the aim to operate as holographic optical elements (HOE) for various purposes and experiments, have demonstrated their flexibility for maintaining the high performance under a wide range of spatial frequencies and laser sources conditions for the recording and readout.[23–26]

However, in order to perform the comparative study with the photopolymerizable glasses incorporating IL, these analyses were revisited by using in the subsequent characterization samples synthesized at the same time than those with IL, and thus ensuring the same synthesis conditions for all the photopolymerizable glasses of the present study.

Photopolymerizable glass samples incorporating HRIS were synthesized according to the previously disclosed process[13] (also described in the Appendix), with thicknesses ranging from 18 to 84 μm. Gelation was performed with a thermal treatment at a controlled temperature of 40 °C during a period of 14 hs. As expected, and following the already well established characteristics, photopolymerizable glass samples incorporating HRIS showed an excellent surface quality and homogeneity, with very low scattering.

B. Grating recording and characterization

Volume phase holographic gratings (VPHG) were recorded in the photopolymerizable glass samples by interference of two mutually coherent s-polarized beams of equal intensities using a Mach-Zehnder type interferometer illuminated with a solid state laser beam centered at a wavelength of 532 nm (Oxxius 532S). An output power of 50mW was equally divided between the two beams, which were incident on the sample at an angle of 7.9° from the sample normal. The resulting interference fringes had a spatial frequency of 500 lines/mm. These conditions correspond to the Bragg diffraction regime.

The gratings were recorded shortly after the synthesis of the photopolymerizable glasses, with storage times prior to the recordings of up to 8 hs.

The evolution of the grating formation was monitored during the recording by a nonactinic probe beam from a He-Ne laser at 632.8 nm with an output power of 0.5 mW (Newport ULM-TILT). Angular selectivity of the recorded gratings was monitored by measuring the first Bragg diffracted order with the same He-Ne laser and the sample placed on a high-precision rotation platform. Δn values were obtained by fitting the resulting angular selectivity curve to the theoretical expression derived from Kogelnik's scalar first-order approximation for light diffraction by dielectric volume holographic gratings[10]:

$$\Delta n = 2\, n_0 \,\mathrm{Cos}\,(\vartheta_0)\, \mathrm{Sin}(\vartheta_0)\, T \frac{\mathrm{ArcSin}(\sqrt{\eta})}{\sqrt{\pi^2 - \left(\mathrm{ArcSin}(\sqrt{\eta})\right)^2}}, \quad (1)$$

where n_o is the refractive index of the photomaterial prior to modulation; θ_0 is the Bragg angle; T is the sample thickness; and η is the diffraction efficiency. The latter was calculated as $\eta = P_{-1}/P_0$, where P_{-1} is the power in the –1st diffraction order and P_0 is the power in the probe beam incident on the sample.

C. Grating refractive index modulation and diffraction efficiency

Figure 1 shows the obtained Δn values for six different volume holographic gratings implemented in photopolymerizable glass samples containing HRIS, with a spatial frequency of 500 lines/mm. As mentioned before, note that refractive index modulations up to 1.0×10^{-2} were achieved in earlier experiments with the same formula.[13]

Photopolymerizable glasses incorporating HRIS show a very good repeatability for refractive index modulation values among gratings implemented within the same synthesis procedure, and reaching, in this case, $\Delta n = 8.7 \times 10^{-3}$.

Δn is observed to remain constant in average versus the sample thickness. The high achieved values are a consequence of the efficient diffusion mechanism of the HRIS, as in the recording process the HRIS migrates from the dark fringes of the recording interference pattern to the

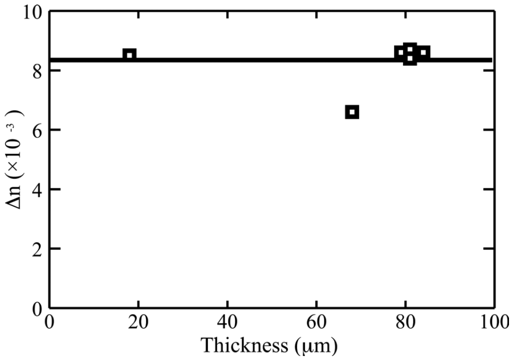

FIG. 1. Refractive index modulation vs holographic grating thickness in a photopolymerizable glass with HRIS. Spatial frequency 500 lines/mm. Volume gratings recorded with a solid-state laser at 532 nm and read with a He-Ne laser at 632 nm in photopolymerizable glasses incorporating HRIS. Straight line: Δn average value.

illuminated regions, thereby increasing the refractive index in the latter.[13]

Within the mentioned Δn limits, diffraction efficiencies close to 100% can readily be achieved, as well as overmodulation regimes, as shown in Fig. 2.

D. Dark diffusion mechanism

After completion of the holographic exposure at the time of recording a diffraction grating, Δn evolves under dark conditions. As a result of the polymerization of the monomeric species in the illuminated regions, the distribution of the monomer inside the glass matrix is not uniform, thus generating migrations of the monomer from the low refractive index regions to the high refractive index ones. The migrated monomer species may also become part of the polymer chains. This monomer diffusion process, which takes place in the absence of additional photon flux, is known as "dark diffusion", and stops when the composition reaches its chemical equilibrium.

In the case of the photopolymerizable glass with HRIS, the temporal evolution of Δn after the holographic recording can be modeled using the weighted sum of two exponential functions[20]:

$$\Delta n(t) = C_M[1 - \exp(-t/\tau_M)] + C_{Zr}[1 - \exp(-t/\tau_{Zr})] \quad (2)$$

The two exponentials account for the contribution to Δn temporal evolution of the monomer and the Zr-based HRIS, respectively, with diffusion time constants $\tau_M < \tau_{Zr}$. The exponential weight factors, C_M and C_{Zr}, account for the contribution of monomer and HRIS components, respectively, to the overall refractive index modulation. Figure 3 shows an example of the fitting of an experimental recording of Δn temporal evolution to Eq. (2). It is appreciated the excellent fitting with the experimental results, and the low noise of the curve.

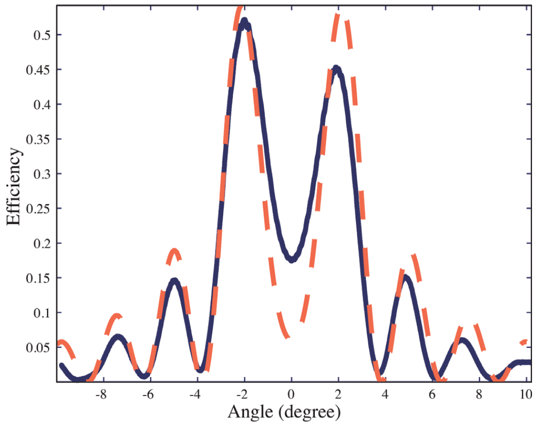

FIG. 2. (Color online) Experimental results (solid) and theoretical fitting (dashed) of the angular selectivity of an overmodulated volume grating recorded in photopolymerizable glass incorporating HRIS. Sample thickness is 80 μm in the measured region. Refractive index modulation $\Delta n = 8.6 \times 10^{-3}$ for a 500 lines/mm grating recorded with a solid-state laser at 532 nm and read with a nonactinic He-Ne laser at 632 nm.

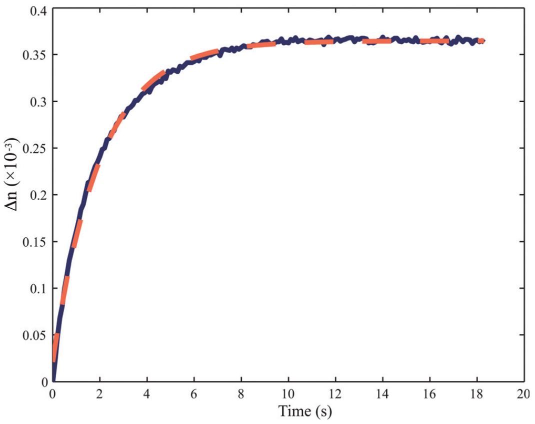

FIG. 3. (Color online) Experimental measurement (solid) and theoretical fitting (dash) of dark diffusion after a 2 s recording pulse at 532 nm. The theoretical fitting corresponds to Eq. (2). Grating spatial frequency 500 lines/mm. Δn was measured with a He-Ne laser at 632nm. Sample thickness 79 μm.

For a particular photopolymerizable glass sample, the four parameters that describe dark diffusion after a recording pulse (C_M, τ_M, C_{Zr}, τ_{Zr}) vary depending on the number of recording pulses already applied to the material, as shown in Fig. 4.

After each pulse, two distinct diffusion processes appear: a fast diffusion associated to the monomeric species, with diffusion time constants on the order of 1s; and a slower diffusion associated with the HRIS, with diffusion time constants ranging from 2 to 6 seconds. The contribution of HRIS to the refractive index modulation is greater than the one of the monomeric species, with $C_{Zr} > C_M$ for all cases. Also, as the number of pulses increases, the presence of polymeric chains in the glass matrix makes high-index species diffusion more difficult, resulting in larger diffusion time constants.

Figure 5 shows the ranges of the diffusion time constant among recording pulses applied to each particular grating, for four different samples of photopolymerizable glasses with HRIS. In all the gratings, the two-exponential behavior and its associated values are consistent with the described results.

The light scattering in the grating samples was analyzed in previous papers[13] and in which it was demonstrated the very low scattering level and the high quality of the diffracted beam profile.

III. PHOTOPOLYMERIZABLE GLASS INCORPORATING IONIC LIQUID: A COMPOSITION WITHOUT HRIS

A. Synthesis

Photopolymerizable glasses with two different IL concentrations (6% and 4% of the total mass, respectively) were synthesized following a process similar to that of the glasses with HRIS (see the Appendix). The IL used in our composition was 1-butyl-3-methylimidazolium tetrafluoroborate ([bmim]BF4), from SIGMA-Aldrich. After casting the sol-gel solution, the samples were heated at 40 °C during sixty hours up to the complete gelation of the photopolymerizable

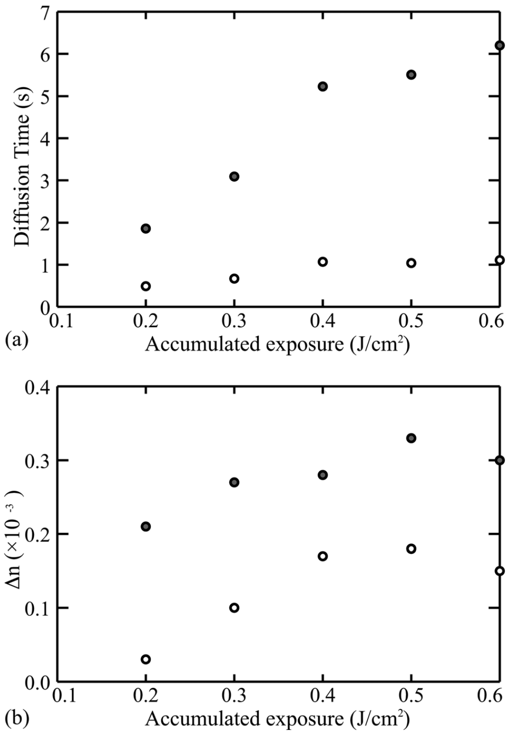

FIG. 4. (a) Diffusion time constants τ_M (open circles) and τ_{Zr} (solid circles); and (b) refractive index modulations C_M (open circles), and C_{Zr} (solid circles) for fitting to Eq. (2), as a function of accumulated exposure during the recording process. An 81 μm thick sample incorporating HRIS. The duration of each recording pulse is 2 s. The first pulse is not shown as it did not yield a measurable refractive index modulation. Maximum value of Δn achieved is 8.6×10^{-2} for a 500 lines/mm grating, recorded with a solid state laser at 532 nm and measured with a He-Ne laser at 632 nm.

glass samples. Samples were prepared with thicknesses ranging from 45 to 165 μm. At a first visual inspection, samples incorporating IL showed a good surface optical quality prior to the recording of VPHGs.

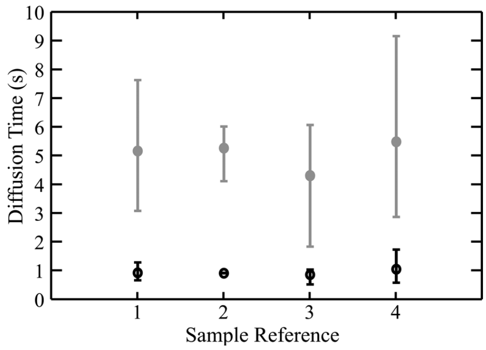

FIG. 5. Diffusion time constants τ_M (open circle) and τ_{Zr} (solid circle) for fitting to Eq. (2) of four samples of photopolymerizable glass incorporating HRIS. Sample 1: thickness 84 μm, $\Delta n = 8.6 \times 10^{-3}$. Sample 2: thickness 79 μm, $\Delta n = 8.6 \times 10^{-3}$. Sample 3: thickness 81 μm, $\Delta n = 8.7 \times 10^{-3}$. Sample 4: thickness 81 μm, $\Delta n = 8.5 \times 10^{-3}$. 500 lines/mm VPHG were recorded with a solid state laser at 532 nm and measured with a He-Ne laser beam at 632 nm.

B. Grating recording and characterization

Following an identical experimental procedure as in Sec. II B., Bragg gratings of spatial frequency 500 lines/mm were recorded in the samples.

C. Grating refractive index modulation and diffraction efficiency

The achieved refractive index modulation for gratings with 500 lines/mm recorded in photopolymerizable glasses incorporating IL are shown in Fig. 6. The maximum refractive index modulation $\Delta n = 5 \times 10^{-3}$, is found for a VPHG implemented in a glass sample synthesized with 6% of IL. The average value of Δn obtained with this concentration (3.35×10^{-3}) is also slightly higher than the one achieved with the 4% concentration (2.95×10^{-3}). However, the VPHGs recorded in the material with the higher concentration of IL (6%) also show a larger variability, with a higher range of resulting Δn values (from 2×10^{-3} for a 45 μm thickness sample to 5×10^{-3} for a 110 μm thickness sample). Therefore, for the sake of a comparative study, the 4% concentration samples exhibit a more stable behavior.

In all studied cases, VPHGs recorded in photopolymerizable glasses incorporating IL show lower Δn values than those disclosed in Sec. II for the photopolymerizable glasses incorporating HRIS. This is expected since HRIS is known to contribute significantly to the overall refractive index modulation. These results are also within the range usually found for the original formula of photopolymerizable glasses which do not incorporate neither IL nor HRIS.[11] Thus, no relevant increase in Δn results with the incorporation of IL in the composition, although other properties of the material related to dark diffusion mechanism and light scattering are indeed affected as shown in Secs. III D and III E.

Notwithstanding reduce Δn values compared to those obtained for VPHGs recorded in photopolymerizable glasses incorporating only HRIS, overmodulation regimes can also be reached. An example of overmodulated VPHG is shown

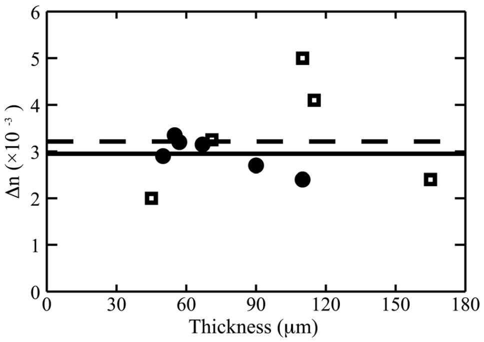

FIG. 6. Refractive index modulation vs holographic grating thickness. Spatial frequency 500 lines/mm. VPHG recorded with a solid-state laser at 532 nm and read with a nonactinic He-Ne laser beam at 632 nm in photopolymerizable glasses incorporating IL. Solid circle: 6% IL (Δn average value: dashed line). Open square: 4% IL (Δn average value: straight line).

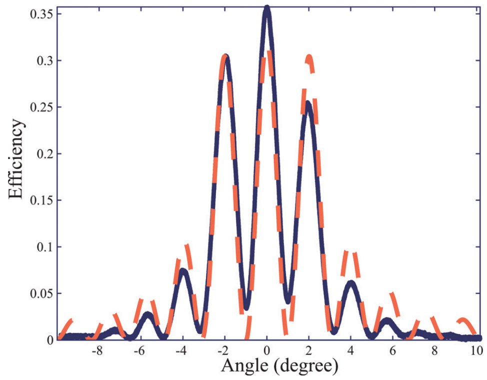

FIG. 7. (Color online) Experimental results (solid) and theoretical fitting (dashed) of the angular selectivity of an overmodulated volume grating recorded in photopolymerizable glass incorporating 6% IL. Sample thickness is 100 μm in the measured region. Refractive index modulation $\Delta n = 5 \times 10^{-3}$ for a 500 lines/mm grating recorded with a solid-state laser beam at 532 nm and read with a nonactinic He-Ne laser at 632 nm.

in Fig. 7 by means of its angular selectivity, which shows three strong peaks near the Bragg angle.

Diffraction efficiencies close to 100% can also be reached with an appropriate exposure by preventing the overmodulation of the VPHGs.

D. Dark diffusion mechanism

Unlike the case of photopolymerizable glass incorporating HRIS, the dark diffusion mechanism shown by glass samples incorporating IL can be fitted to a single exponential function, Eq. (3). In this case, obviously only the contribution of the monomer diffusion (first term to the rhs of Eq. (2)) operates. A good precision for this fitting can be observed in Fig. 8, although, as the Δn obtained is lower than in Fig. 3, the curve presents a lower signal-to-noise ratio. As a consequence, the ripple in Fig. 8 appears to be greater than in Fig. 3, as the amplitude of the curve is smaller, although the absolute amount of noise is similar in both cases.

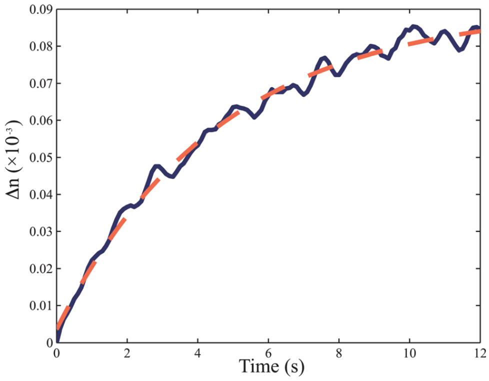

FIG. 8. (Color online) Experimental measurement (solid) and theoretical fitting (dashed) of dark diffusion after a 2 second recording pulse at 532 nm for a photopolymerizable glass incorporating IL. The theoretical fitting corresponds to Eq. (2). Grating spatial frequency 500 lines/mm. Δn was measured with a nonactinic He-Ne laser at 632 nm. Sample thickness is 110 μm.

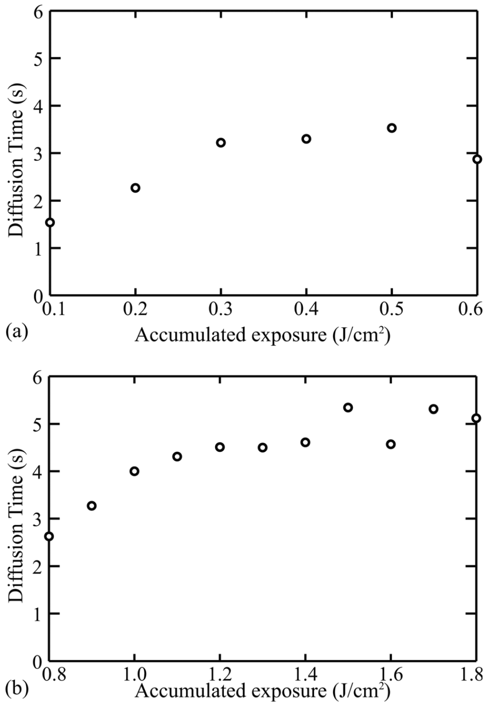

FIG. 9. (a) Diffusion time constants τ_M for fitting to Eq. (3) as a function of accumulated exposure during the recording process. Thickness 110 μm. IL concentration 6%. (b) Thickness 55 μm. IL concentration 4%. The duration of each recording pulse is 2 s. Pulses not shown did not yield a significant refractive index modulation. Final Δn achieved are 4.85×10^{-3} (a) and 3.5×10^{-3} (b) for a 500 lines/mm grating, recorded with a solid state laser at 532 nm and measured with a nonactinic He-Ne laser at 632 nm.

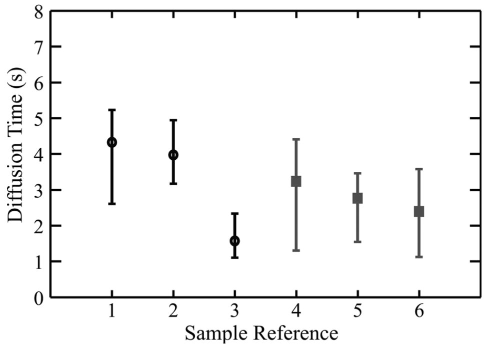

FIG. 10. Diffusion time constants τ_M for fitting to Eq. (3) of three samples of photopolymerizable glass incorporating 4% IL (open circle) and three samples incorporating 6% IL (solid square). Sample 1: thickness 55 μm, $\Delta n = 3.35 \times 10^{-3}$. Sample 2: thickness 50 μm, $\Delta n = 2.9 \times 10^{-3}$. Sample 3: thickness 57 μm, $\Delta n = 3.2 \times 10^{-3}$. Sample 4: thickness 110 μm, $\Delta n = 4.85 \times 10^{-3}$. Sample 5: thickness 115 μm, $\Delta n = 4.1 \times 10^{-3}$. Sample 6: thickness 165 μm, $\Delta n = 2.9 \times 10^{-3}$. 500 lines/mm VPHG were recorded with a solid state laser at 532 nm and measured with a nonactinic He-Ne laser beam at 632 nm.

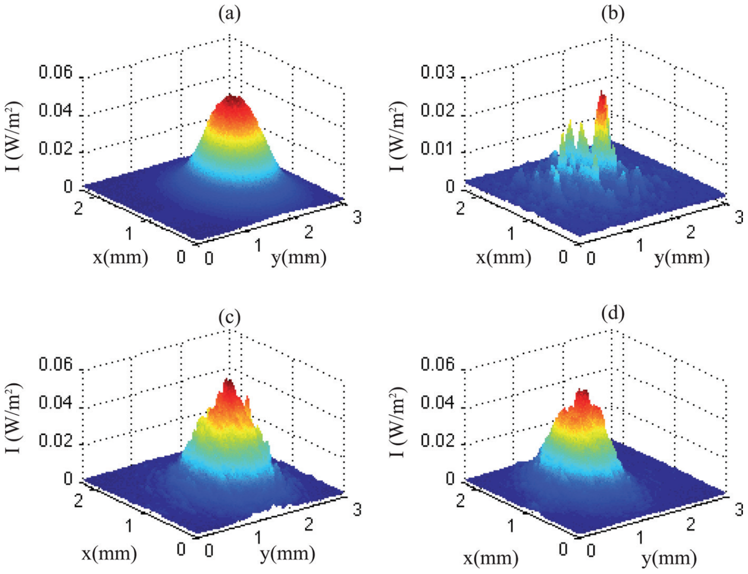

FIG. 11. (Color online) Incident beam (a), first-order diffracted beam without surface scattering compensation (b), zero-th order diffracted beam with surface scattering compensation (c) and first order diffracted beam with surface scattering compensation (d), for a 500 lines/mm grating implemented in a photopolymerizable glass incorporating a IL concentration of 6%. Measurements obtained with a nonactinic He-Ne laser at 632 nm.

$$\Delta n(t) = C_M[1 - \exp(-t/\tau_M)] \tag{3}$$

The absence of a second exponential term in the rhs of Eq. (3) confirms that the IL does not act as a photoactive element and it does not contribute in an independent manner to the refractive index modulation. However, as a direct consequence of the presence of the IL in the glass matrix, the diffusion time constants (τ_M) of the monomer dark diffusion present higher values, than those shown in Fig. 5. These values typically range between 1 and 5 seconds.

Figure 9 presents an example of the evolution of the diffusion time constant during a VPHG recording process. As in the results shown in Sec. II D, the diffusion time constant tends to increase with the temporal evolution of the recording process, as the presence of polymer chains inside the glass matrix hinder particle diffusion.

The aforementioned longer diffusion time constants compared to those obtained for the free monomer in the presence of HRIS, are common to all analyzed samples, of a total of six, that incorporate IL, as shown in Fig. 10.

E. Light scattering

The incorporation of IL to the photopolymerizable glass composition also has a direct impact on the light scattering and on the optical quality of the sample after the recording of the VPHG. Spherical cavities with typical diameters of 1–3 μm appear both on the surface and on the bulk of the glass matrix, increasing the light scattering and thus affecting the light diffracted intensity distribution. Further studies, performed by comparing the first-order diffracted beam before and after using a refractive index compensator (Norland Index Matching Liquid 150, $n = 1.52$) to minimize the effect of surface irregularities, show that most of the light scattering originates on the surface of the samples, and can thus be readily compensated for. An example of this comparison study can be found in Fig. 11.

It should be noted that, although the light scattering increases due to the presence of IL, and it is undesirable for data storage applications, it can be nevertheless taken advantage for other applications such as optical diffusers, specially since the amount of light scattering introduced by the photopolymerizable glass can be controlled by varying the amount of IL included in the sample.

F. SEM analysis

Figure 12 presents a SEM image (obtained with Zeiss DSM-950 instrument{PossibleAd}) of a 30 μm thickness photopolymerizable glass sample incorporating, in this case, 7.6% IL for an enhanced observation of the phenomena associated

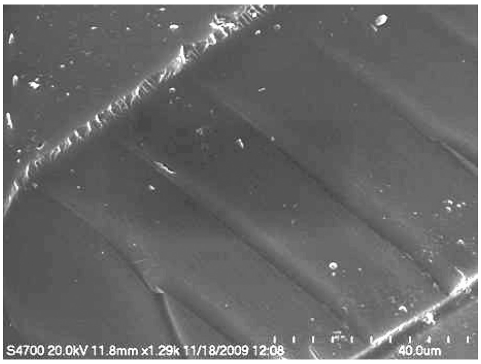

FIG. 12. SEM image of a VPHG implemented in a photopolymerizable glass incorporating IL. IL concentration is 7.6%. Sample thickness is 30 μm and grating period is 20 μm.

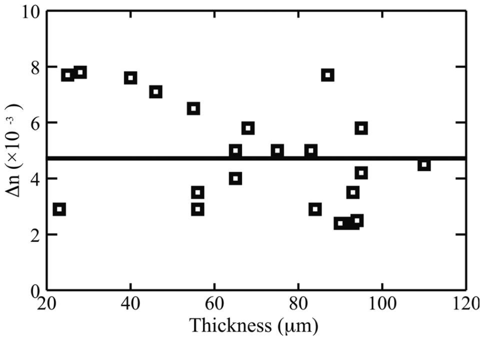

FIG. 13. Refractive index modulation vs holographic grating thickness. Spatial frequency 500 lines/mm. Volume gratings recorded with a solid-state laser at 532 nm and read with a nonactinic He-Ne laser at 632 nm in photopolymerizable glasses incorporating both HRIS and IL (concentration 3.2%). Straight line: Δn average value.

to the incorporation of IL to the sample. The presence of a 50 lines/mm grating is apparent, as well as the generation of the aforementioned cavities, with diameters of up to ~3 μm.

Although the period of the VPHG of the image ($\Lambda = 20\,\mu$m) is greater than the size of the cavities, in a VPHG with a higher spatial frequency (for example, 500 lines/mm and period $\Lambda = 20\,\mu$m), the size of the cavities would be similar to the period of the VPHG, thus interfering with its refractive index pattern.

IV. PHOTOPOLYMERIZABLE GLASSES INCORPORATING BOTH HRIS AND IONIC LIQUID

A. Synthesis

Photopolymerizable glasses incorporating both HRIS and IL were also synthesized following a similar process to those disclosed in Secs. II and III (see Appendix), obtaining samples ranging from 25 to 110 μm thickness. Glass samples exhibited a fast deterioration once gelated, presenting opaque areas on their surface. This phenomenon indicates instabilities in the coexistence of the IL and the HRIS within the glass matrix.

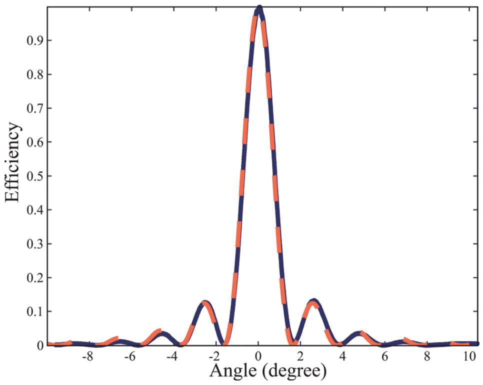

FIG. 14. (Color online) Experimental results (solid) and theoretical fitting (dashed) of the angular selectivity of VPHG recorded in a photopolymerizable glass incorporating HRIS and IL (concentration 3.2%). Sample thickness is 93 μm in the measured region. Refractive index modulation $\Delta n = 3.5 \times 10^{-3}$ for a 500 lines/mm grating recorded with a solid-state laser at 532 nm and read with a nonactinic He-Ne laser at 632 nm.

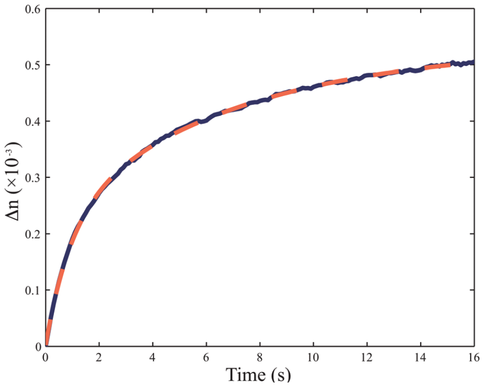

FIG. 15. (Color online) Experimental measurement (solid) and theoretical fitting (dashed) of dark diffusion after a 2 second recording pulse at 532 nm for a photopolymerizable glass incorporating both HRIS and IL (concentration 3.2%). The theoretical fitting corresponds to Eq. (2). Grating spatial frequency 500 lines/mm. Δn was measured with a nonactinic He-Ne laser at 632 nm. Sample thickness is 110 μm.

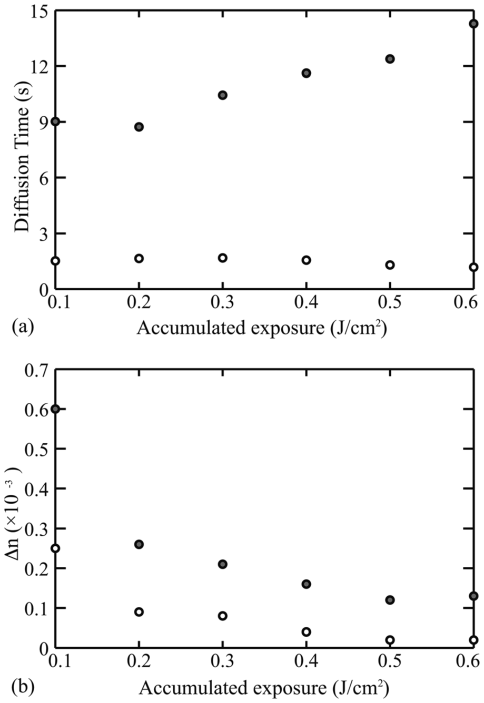

FIG. 16. (a) Diffusion time constants τ_M (open circle) and τ_{Zr} (solid circle); and (b) refractive index modulations C_M(open circle), and C_{Zr} (solid circle) for fitting to Eq. (2) as a function of accumulated exposure during the recording process, for a 94 μm thick photopolymerizable glass sample incorporating both HRIS and IL (IL concentration: 3.2%). The duration of each recording pulse is 2 s. Final Δn achieved is 2.5×10^{-3} for a 500 lines/mm grating, recorded with a solid state laser beam at 532 nm and measured with a nonactinic He-Ne laser beam at 632 nm.

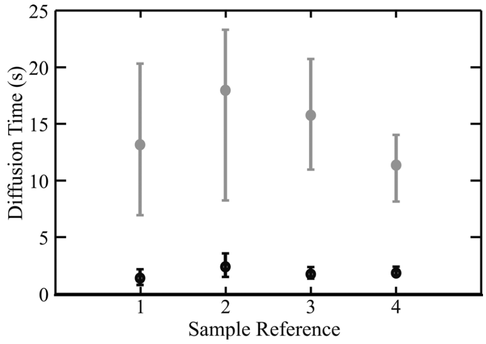

FIG. 17. Diffusion time constants τ_M (open circle) and τ_{Zr} (solid circle) for fitting to Eq. (2) of four samples of photopolymerizable glass incorporating HRIS and IL (concentration 3.2%). Sample 1: thickness 28 μm, $\Delta n = 7.8 \times 10^{-3}$. Sample 2: thickness 23 μm, $\Delta n = 2.9 \times 10^{-3}$. Sample 3: thickness 93 μm, $\Delta n = 3.5 \times 10^{-3}$. Sample 4: thickness 56 μm, $\Delta n = 5.8 \times 10^{-3}$. 500 lines/mm VPHG were recorded with a solid state laser at 532 nm and measured with a nonactinic He-Ne laser at 632 nm.

B. Grating recording and characterization

Bragg gratings of spatial frequency 500 lines/mm were recorded and characterized using the same method as disclosed in Sec. II B.

C. Grating refractive index modulation and diffraction efficiency

Figure 13 presents Δn reached for a set of 500 lines/mm gratings recorded in a photopolymerizable glass incorporating both HRIS and IL. Although values up to $\Delta n = 7.8 \times 10^{-3}$ were reached, results showed a poor repeatability, with Δn ranging from 7.8×10^{-3} to 2.5×10^{-3} under the same synthesis and recording conditions.

As a consequence of these results, although Δn values close to those obtained with photopolymerizable glasses incorporating only HRIS can be obtained, the instability of the mixture of HRIS and IL (possibly due to influence on hydrolysis of Zr precursor) results in an increased uncertainty in Δn achieved.

An example of an optimized angular selectivity of a VPHG recorded in a photopolymerizable glass incorporating both HRIS and IL is shown in Fig. 14, with a diffraction efficiency close to 100%.

D. Dark diffusion mechanism

The measured dark diffusion of photopolymerizable glasses incorporating both IL and HRIS presents a good fit to Eq. (2). As in the case of glasses incorporating only HRIS, two diffusion processes with different kinetics can be distinguished. The faster diffusion component corresponds to the monomeric species, while the slower one accounts for the migration of the HRIS. Figure 15 shows an excellent fit to the model.

As we discussed in Sec. III, IL does not directly modify the Δn value, but it does interact with the monomer and the HRIS inside the glass matrix, by increasing the diffusion time constants of the components. This effect can be seen in Fig. 16. In this case, HRIS shows a greater contribution to the Δn than the monomer, both decreasing with the number of recording pulses.

Figure 17 shows the range of diffusion time constants for a variety of photopolymerizable glass samples incorporating both HRIS and IL. The diffusion times for the monomer and the HRIS are shown to be maintained for a longer period of time in the presence of IL, compared to the case of the material incorporating only HRIS (see Sec. II D).

E. Light scattering

The optical quality and light scattering properties of a photopolymerizable glass incorporating both HRIS and IL present a great variability among samples, as a consequence

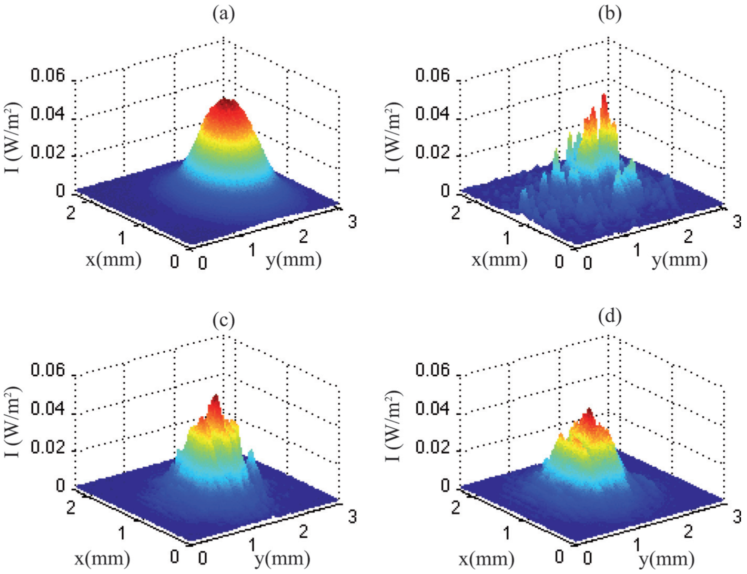

FIG. 18. (Color online) Incident beam (a), first-order diffracted beam without surface scattering compensation (b), zero-th order diffracted beam with surface scattering compensation (c) and first order diffracted beam with surface scattering compensation (d) for a 500 lines/mm grating implemented in a photopolymerizable glass incorporating HRIS and a IL concentration of 3.2%. Measurements obtained with a He-Ne laser at 632 nm.

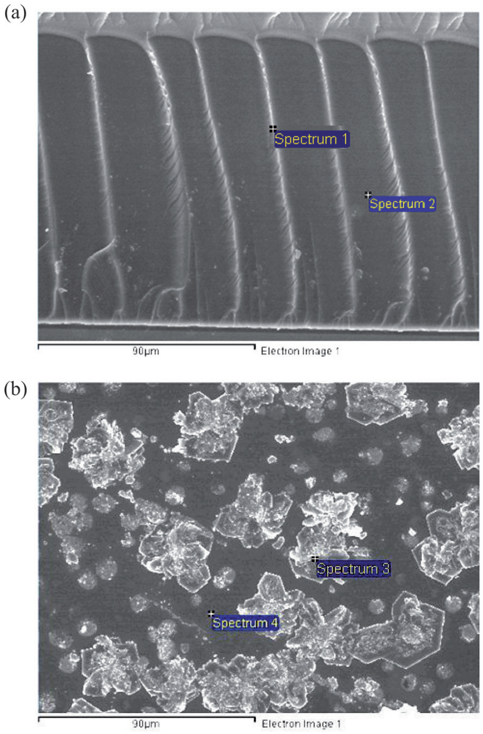

FIG. 19. (Color online) SEM images of the surface of a photopolymerizable glass incorporating both HRIS and IL (a), and of a volume grating formed in the glass matrix (b). Positions where spectral analysis was performed are also indicated.

of an apparently unstable coexistence of HRIS and IL inside the glass matrix. Samples prepared under similar conditions range from an acceptable optical quality to poor surfaces presenting certain irregularities and haze. An example is shown in Fig. 18.

F. SEM analysis

Figure 19 shows SEM images (obtained with a Zeiss DSM-950 instrument) in which the scattering aggregates are apparent. The percentage of zirconium concentration in different regions of a sample (see Table I) was determined by means of spectral analysis. Similar low amounts of zirconium were found in the dark and light fringes of a 50 lines/mm VPHG implemented in the glass. The surface of the glass (a) showed a markedly increased zirconium concentration compared to the grating region (b), especially in areas where the aggregates were formed. The HRIS appear to have been expelled from the glass matrix, then reducing or even annulling its contribution to the Δn of the VPHG. Obviously, the aggregations of HRIS on the surface of the photopolymerizable glass greatly reduces the optical quality of the affected samples.

TABLE I. Zirconium concentration of a photopolymerizable glass incorporating HRIS and IL.

Position	Zr concentration (%)
Spectrum 1	2.59
Spectrum 2	2.88
Spectrum 3	20.26
Spectrum 4	9.00

V. DISCUSSIONS AND CONCLUSIONS

Three types of photopolymerizable glasses have been presented and systematically characterized in terms of refractive index modulation, angular selectivity, dark diffusion mechanism and light scattering. The photomaterials were synthesized following similar procedure previously implemented in other studies.

The photopolymerizable glass incorporating HRIS, already disclosed in previous publications, exhibits very high diffraction efficiency (near 100%) and refractive index modulation (up to $\Delta n = 1.0 \times 10^{-2}$), as well as a very good optical quality, the parameters relevant for optical data storage applications.

The photopolymerizable glass incorporating ionic liquid, disclosed here for the first time, exhibits a lower refractive index modulation (up to $\Delta n = 5 \times 10^{-3}$), but still presents enough dynamic range to reach diffraction efficiencies close to 100% and overmodulation regimes. The presence of IL enhances the diffusion of the monomeric species.

Finally, the photopolymerizable glass incorporating both HRIS and IL, also disclosed here for the first time, show comparatively high refractive index modulations (up to $\Delta n = 7.8 \times 10^{-3}$), although instabilities in the coexistence of HRIS and IL may result in precipitation of Zr-based components. This phenomenon implies a greater variability in achieved Δn values and optical qualities. Diffusion time constants of both HRIS and monomer are increased by the presence of IL.

APPENDIX: SAMPLES PREPARATION

The chemical procedure for the synthesis of the photopolymerizable glass incorporating HRIS was reported in detail in Ref. 13 here we summarize the basic steps:

The silica sol is prepared by acid hydrolysis of glycidoxypropyltrimethoxysilane (GPTMS) and tetraethylorthosilicate (TEOS). After 10 mins of stirring, a solution of IRGAGURE-784 photosensitizer in POEA is added. After further 10 mins of stirring, a solution of zirconium isopropoxide isopropanol complex in methacrylic acid is added to the mixture. The resulting sol is filtered with a 0.2 μm Millipore filter.

For the synthesis of the photopolymerizable glass incorporating IL we have used the analogous chemical formula but ZrO_2 was not included, being replaced by the IL (namely, 1-Butyl-3 methylimidazolium tetrafluorborate, ALDRICH). Two particular weights of IL were applied for two types of samples: 4% and 6% of the total mass.

For the synthesis of the photopolymerizable glass incorporating HRIS and IL a similar procedure as the previous one was followed but the HRIS was incorporated before adding the IL (weights: 9.5% HRIS and 3.2% IL, respectively, of the total mass).

ACKNOWLEDGMENTS

Financial support from the Spanish Ministry of Science and Innovation (MICINN) under grant TEC2008-04105 is acknowledged.

A.V.V. acknowledges a fellowship from MICINN and M.P.H.G. acknowledges a fellowship from the Spanish Ministry of External Affairs and CONACyT (Mexico).

We thank O. Martínez-Matos for helpful suggestions and discussions.

[1] M. L. Calvo, P. Cheben, *Advances in Information Optics and Photonics*, edited by Ari T. Friberg, R. Dändliker, (SPIE Press, Bellingham, 2008), Chap 15, Vol. 6.

[2] M. L. Calvo, P. Cheben, J. Opt. A: Pure Appl. Opt. **11**, 024009 (2009).

[3] M. Haw, Nature **422**, 556 (2003).

[4] D. Psaltis, F. Mok, Sci. Am. **273**, 70 (1995).

[5] F. Mok, G. Zhou, D. Psaltis, *Holographic Read-Only Memory* in Holographic Data Storage, edited by H. J Coufal, D. Psaltis, G.T. Sincerbox, (Springer, Berlin, 2000), pp. 399–407.

[6] L. Solymar, D. J. Cooke, *Volume Holography and Volume Gratings*, (Academic Press, London, 1981), Chap 10.

[7] W. Wilson, A. Hoskins, M. Ayres, A. Hill, K. Curtis, *Holographic Data Storage: From Theory to Practical Systems*, edited by K. Curtis, L. Dhar, A. Hill, W. Wilson, M. Ayres, (John Wiley and Sons, Ltd, Chichester, 2010), Chap. 2.

[8] G. T. Sincerbox, *Current Trends in Optics*, edited by J. C. Dainty, (Academic, London, 1994), Chap 14, Vol. 2.

[9] R. A. Lessard, G. Manivannan, Proc SPIE **2405**, 2 (1995).

[10] H. J. Coufal, D. Psaltis, G. T. Sincerbox, *Holographic Data Storage* (Springer, New York, 2000).

[11] P. Cheben, T. Belenguer, A. Nuñez, F. del Monte, D. Levy, Opt. Lett. **22**, 1857 (1996).

[12] F. Del Monte, O. Martínez-Matos, J. A. Rodrigo, M. L. Calvo, P. Cheben, Adv. Mater. **18**, 2014 (2006).

[13] P. Cheben, M. L. Calvo, Appl. Phys. Lett. **78**, 1490 (2001).

[14] K. Omura, Y. Tomita, J. Appl. Phys. **107**, 023107 (2010).

[15] P. Wasserscheid, T. Welton, *Ionic Liquids in Synthesis* (Wiley, Weinheim, 2003).

[16] M. A. Klingshirn, S. K. Spear, J. D. Holbrey, R. D. Rogers, J. Mater. Chem. **15**, 5174 (2005).

[17] A. J. Carmichael, D. M. Haddleton, S. A. F. Bon, K. R. Seddon, Chem. Commun. **14**, 1237 (2000).

[18] K. Hong, H. Zhang, J. M. Mays, A. E. Visser, C. S. Brazel, J. H. Holbrey, W. M. Reichert, R. D. Rogers, Chem. Commun. **13**, 1368 (2002).

[19] S. Harrisson, S. R. Mackenzie, D. M. Haddleton, Chem. Commun. **23**, 2850 (2002).

[20] H. Lin, P. W. Oliveira, M. Veith, Appl. Phys. Lett. **93**, 141101 (2008).

[21] H. Kogelnik, Bell. Syst. Tech. J. **48**, 2909 (1969).

[22] H. Lin, P. W. Oliveira, M. Veith, M. Gros, I. Grobelsek, Opt. Lett. **34**, 1150 (2009).

[23] M. L. Calvo, P. Cheben, O. Martínez-Matos, F. del Monte, J. A. Rodrigo, Phys. Rev. Lett. **97**, 084801 (2006).

[24] O. Martínez-Matos, M. L. Calvo, A. Rodrigo, Appl. Phys. Lett. **91**, 14115 (2007).

[25] O. Martínez-Matos, J. A. Rodrigo, M. L. Calvo, V. Hevia-Martín, P. Cheben, Inf. Opt. **18**, 21 (2009).

[26] O. Martínez-Matos, J. A. Rodrigo, M. P. Hernández-Garay, J. G. Izquierdo, R. Weigand, M. L. Calvo, P. Cheben, P. Vaveliuk, L. Bañares, Opt. Lett. **35**, 652 (2010).

V

Published results on silicon based photonic devices

This chapter presents the results of this thesis on the development of photonic devices for the silicon-on-insulator platform, as published in the following peer reviewed journal papers:

5.1. High resolution Fourier-transform spectrometer chip with microphotonic silicon spiral waveguides (Optics Letters).

5.2. Ultracompact polarization converter with a dual subwavelength trench built in a silicon-on-insulator waveguide (Optics Letters).

5.3. Demonstration of a curved sidewall grating demultiplexer on silicon (Optics Express).

5.4. Bandpass filter implemented with blazed waveguide sidewall gratings in silicon-on-insulator (Electronic Letters).

706 OPTICS LETTERS / Vol. 38, No. 5 / March 1, 2013

High-resolution Fourier-transform spectrometer chip with microphotonic silicon spiral waveguides

Aitor V. Velasco,[1,3] Pavel Cheben,[2,*] Przemek J. Bock,[2] André Delâge,[2] Jens H. Schmid,[2] Jean Lapointe,[2] Siegfried Janz,[2] María L. Calvo,[1] Dan-Xia Xu,[2] Mirosław Florjańczyk,[2] and Martin Vachon[2]

[1]*Departamento de Óptica, Facultad de Ciencias Físicas, Universidad Complutense de Madrid, Madrid 28040, Spain*

[2]*National Research Council Canada, Ottawa, Ontario K1A 0R6, Canada*

[3]*e-mail: avillafr@pdi.ucm.es*

**Corresponding author: pavel.cheben@nrc.ca*

Received December 21, 2012; revised January 25, 2013; accepted January 25, 2013;
posted January 29, 2013 (Doc. ID 182206); published February 25, 2013

We report a stationary Fourier-transform spectrometer chip implemented in silicon microphotonic waveguides. The device comprises an array of 32 Mach–Zehnder interferometers (MZIs) with linearly increasing optical path delays between the MZI arms across the array. The optical delays are achieved by using Si-wire waveguides arranged in tightly coiled spirals with a compact device footprint of 12 mm^2. Spectral retrieval is demonstrated in a single measurement of the stationary spatial interferogram formed at the output waveguides of the array, with a wavelength resolution of 40 pm within a free spectral range of 0.75 nm. The phase and amplitude errors arising from fabrication imperfections are compensated using a transformation matrix spectral retrieval algorithm. © 2013 Optical Society of America

OCIS codes: 130.3120, 300.6300.

Compact spectral filters with a small footprint are required for a wide range of applications, including wavelength-division-multiplexed communications, optical interconnects, biological and environmental sensing, and space instrumentation [1]. Planar waveguide devices such as arrayed waveguide gratings (AWGs) [2], echelle gratings [3,4], lattice filters [5], ring resonators [6], and sidewall grating filters [7,8] can achieve a high spectral resolution for a small device footprint, but their optical throughput (étendue) is largely limited by the requirement of a single-mode input waveguide. Étendue is of critical importance for spectroscopy applications, especially when spatially extended and incoherent sources are analyzed. This limitation can be overcome with planar waveguide Fourier-transform (FT) spectrometers [9,10] based on the principle of spatial heterodyne spectroscopy (SHS) [11]. SHS benefits from the intrinsically large étendue of the Michelson interferometer [12] and replaces the moving mirrors by stationary diffraction gratings [11]. In a planar waveguide SHS FT spectrometer, all the outputs of the device, corresponding to different optical path lengths of the interferometer array, are monitored simultaneously in a single measurement of the output spatial interferogram [9,10]. The source spectrum can be retrieved by mathematical analysis of the interferogram.

In a typical configuration, a waveguide array of Mach–Zehnder interferometers (MZIs) with increasing path differences are used to implement the SHS concept [9,10]. For such a geometry, the source power spectrum and the output interferogram are related by the cosine FT. A similar MZI array geometry, including phase-correction circuits using independent heaters for each MZI, has also been demonstrated [13]. However, when long optical path delays are required for high spectral resolution, similar configurations yield prohibitively large devices.

In this Letter, we present a compact FT spectrometer chip, in which a high spectral resolution of 40 pm with a compact device size is achieved by using tightly coiled spiral waveguide structures in an MZI array. Furthermore, a spectral retrieval algorithm with phase and amplitude error compensations is demonstrated for the first time to the best of our knowledge, obviating the need for dedicated phase correction circuits. The FT spectrometer is implemented as an array of N MZIs in silicon-on-insulator (SOI) waveguides (Fig. 1). Each MZI comprises a reference arm of constant length and a delay arm with a spiral waveguide. The length of the delay arm, i.e., spiral length, linearly increases by ΔL across the array. The high refractive index contrast of the SOI platform and the waveguide bend radius of ~5 μm readily allows the making of spirals with geometrical lengths of over a centimeter within an area only a few hundred micrometers in diameter.

For a given input spectral distribution, the dispersive property of the MZI array results in a wavelength-dependent spatial interferogram at the outputs of the array. The relation between the input spectral distribution and the interferogram $I(x_i)$ is unambiguous within

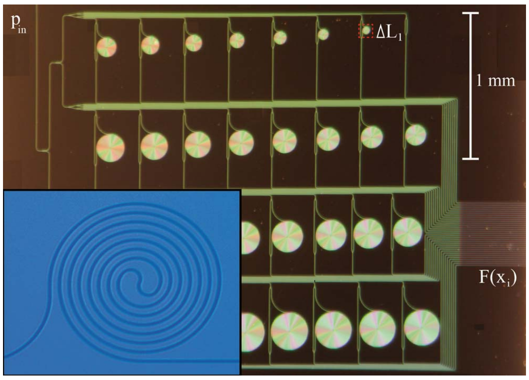

Fig. 1. (Color online) Optical micrograph of the fabricated spatial heterodyne FT spectrometer chip with spiral Si-wire waveguides. Inset: magnified view of the spiral structure.

0146-9592/13/050706-03$15.00/0

the free spectral range (FSR) of an ideal device without phase errors:

$$I(x_i) = \int_0^{\mathrm{FSR}} B(\bar{\sigma}) \cos 2\pi\bar{\sigma}x_i \mathrm{d}\bar{\sigma}, \tag{1}$$

where B is the incident spectral density, x_i is the path delay of the ith MZI, and $\bar{\sigma} = \sigma - \sigma_L$ is the shifted wavenumber, relative to the Littrow wavenumber σ_L, at which a monochromatic input produces a constant spatial power distribution at the outputs of the MZI array [10]. The input spectrum can be calculated from the discretized output interferogram using a discrete cosine transform.

The wavelength resolution ($\delta\lambda$) and the FSR of the device are determined by the maximum path difference and the number of interferometers [10,13], respectively:

$$\delta\lambda = \frac{\lambda_0^2}{\Delta L_{\max} n_g}, \tag{2}$$

$$\mathrm{FSR} = \delta\lambda \frac{N}{2}, \tag{3}$$

where λ_0 is the device operational central wavelength and n_g is the waveguide group index. The FSR of the device is half the period of the least unbalanced MZI, due to the symmetry of the interferograms.

The FT spectrometer was designed with 32 MZIs and with spiral lengths increasing across the array by $\Delta L =$ 365 μm up to $\Delta L_{\max} = 1.13$ cm for the most unbalanced interferometer. The longest spiral occupies an area with a diameter of 270 μm. 450 nm wide Si-wire waveguides ensure monomode operation and minimize bend losses, with a minimum bend radius of 5 μm at the turning point of the spirals. The waveguides were nominally designed for TM polarization, with an effective index of 2.12 at the central wavelength of 1.55 μm. Our device can be implemented in a layout with N independent input waveguides at a chip facet feeding into the MZI array, for an étendue N times larger than the throughput of a single input waveguide [10]. However, to simplify optical measurements and use conventional telecom waveguide characterization equipment, we used a modified layout with a single input waveguide at the facet followed by cascaded y-couplers. The operational principles and spectral retrieval techniques of both layouts are identical.

Devices were fabricated on SOI with 0.26 μm thick silicon and 2 μm thick buried oxide. Si-wire waveguide structures were defined in a single patterning step by electron beam lithography using hydrogen silsesquioxane (HSQ) resist. Inductively coupled plasma reactive ion etching was used to transfer the resist pattern into the silicon layer.

The fabricated device was characterized using a high-resolution tunable semiconductor laser over the spectral range of 1550–1552 nm, with a wavelength step of 0.1 pm. Efficient subwavelength grating couplers [14] were included at the input and output facets of the chip for optimized fiber coupling, while at the same time reducing the Fabry–Perot effect due to the reflectivity at the facets. A Peltier stage was used for thermal stabilization of the chip, and a polarization controller was used to select the TM-polarized input field. Output light from all the MZIs was collected in a single shot with a high-sensitivity IR CCD camera.

Figure 2 shows the output interferogram of the 32 MZIs for the measured wavelength range. Detailed inspection of the interferogram reveals two main effects causing deviations from the theoretical performance given by Eq. (1). First, waveguide insertion loss increases with the path difference of the interferometers, resulting in a reduction of the visibility of the MZI transmittance function:

$$V = \frac{I_{\max} - I_{\min}}{I_{\max} + I_{\min}} = \frac{2\sqrt{I_1 I_2}}{I_1 + I_2}, \tag{4}$$

where $I_{\max}$ and $I_{\min}$ are the maximum and minimum output intensities of the MZI and I_1 and I_2 are the intensities at the outputs of its two arms. Propagation losses of −4 dB/cm were measured, with bending losses of −1.7 dB/cm in the spiral sections. This effect can be readily compensated by dividing the output pattern by the visibility function [Eq. (4)] of each MZI, measured in a calibration wavelength scan. Second, deviations in the effective index and optical path errors arising from fabrication imperfections result in phase errors that distort the interferogram. In particular, a mean group index of 4.38 was measured, with variations of <1% in the periodicity of the MZI transmittance across the array from the theoretical (cosine) function. As a consequence of these random variations, the outputs of the MZI interferometers in the array are misaligned in phase and a Littrow wavenumber σ_L is not found within the analyzed wavelength range. This is a consequence of nonorthogonality of the base of the cosine transform in the presence of phase errors. A solution to incorporate this effect to the model of the discrete Fourier cosine transform was proposed [15]; however, it required phase correction circuits and multiple measurements at varying temperatures.

Here we report a spectral retrieval method that does not require multiple measurements for phase error corrections and also obviates the need for phase tuning. Instead of using the cosine transform, our spectral retrieval algorithm is based on a system of linear equations. The transmittance function of each MZI was sampled at M

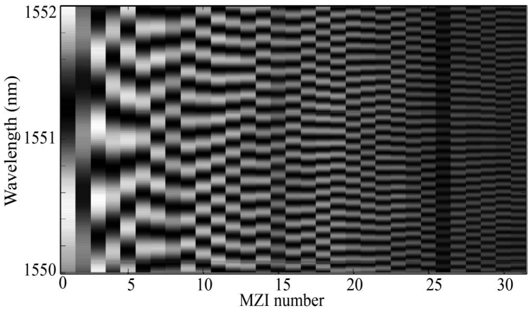

Fig. 2. Experimental measurement of the output power distribution of the 32 MZIs for a 2 nm wavelength scan near 1.55 μm wavelength.

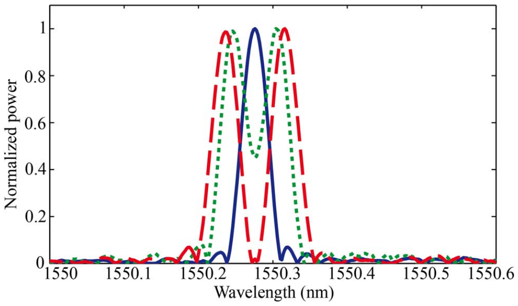

Fig. 3. (Color online) Spectra of a narrowband laser source (solid curve) and two doublets of two monochromatic lines separated by 56 pm (dotted curve) and 80 pm (dashed curve), experimentally retrieved with the spatial heterodyne FT spectrometer chip.

equidistant wavelengths within the FSR of the device. An $N \times M$ transformation matrix T was defined such that $I(x_i) = B \times T$. The source power spectrum B is retrieved by multiplying the spatial interferogram $I(x_i)$ by T^+, which is a pseudoinverse of the transformation matrix T. The pseudoinverse matrix is computed by single value decomposition [16]. In this procedure, the influence of phase and amplitude errors is compensated, since the actual MZI transmittance functions (as measured in the calibration step) are used instead of an ideal cosine function. This yields a robust result compared to the conventional cosine transform technique, which requires an active compensation of the phase errors [15].

Figure 3 shows signal spectra, experimentally retrieved using our device and algorithm, for a single monochromatic source (solid curve), a doublet of two monochromatic lines separated by 56 pm (dotted curve), and a doublet of two monochromatic lines separated by 80 pm (dashed curve). The spectral resolution is 42 pm (measured at FWHM), and the FSR is 0.75 nm. Truncation ripple is reduced by applying an apodization window [17]. Because the matrix T^+ is designed to compensate phase errors of the system, and consequently does not perform an FT of an ideal apodization function without said phase errors, the apodization window is applied directly as a convolution in the spectral domain instead of a multiplication of the interferogram.

It is an important advantage of our device that deviations from the ideal design appear as systematic measurable errors in the interferograms. Once the waveguide device has been fabricated and characterized, the errors can simply be corrected using the spectral retrieval algorithm. This cannot be achieved in devices, such as AWGs, with no direct physical access to the arrayed waveguide output aperture, which makes measuring and correcting phase errors of an AWG a formidable task. Unlike in an AWG, our device provides physical access to each of the arrayed interferometer outputs, where both phase and amplitude errors can be readily measured as part of the spectrometer calibration procedure and compensated in the spectral retrieval algorithm.

We have demonstrated a compact FT spatial heterodyne spectrometer consisting of an array of MZIs with linearly increasing optical path delays. The optical delays are achieved by using Si-wire waveguides arranged in tightly coiled spirals. Spectral retrieval is demonstrated with a wavelength resolution of 40 pm and a FSR of 0.75 nm. The phase and amplitude errors are compensated using a transformation matrix spectral retrieval algorithm. The advantage of software compensation of fabrication errors, along with the high resolution and small footprint of the device, are important practical benefits of this FT spectrometer. Its potential applications include biological and environmental sensing, handheld spectroscopic instrumentation, wavelength-division multiplexing optical channel monitoring, and spectroscopic sensing using space exploration probes or microsatellite platforms.

Financial support from the Spanish Ministry of Economy is acknowledged under grants TEC2008-04105 and TEC2011-23629.

References

1. P. Cheben, "Wavelength dispersive planar waveguide devices: echelle gratings and arrayed waveguide gratings," in *Optical Waveguides: from Theory to Applied Technologies*, M. L. Calvo and V. Laksminarayanan, eds. (CRC, 2007), pp. 173–230.
2. P. Cheben, J. H. Schmid, A. Delâge, A. Densmore, S. Janz, B. Lamontagne, J. Lapointe, E. Post, P. Waldron, and D.-X. Xu, Opt. Express **15**, 2299 (2007).
3. S. Janz, A. Balakrishnan, S. Charbonneau, P. Cheben, M. Cloutier, A. Delâge, K. Dossou, L. Erickson, M. Gao, P. A. Krug, B. Lamontagne, M. Packirisamy, M. Pearson, and D.-X. Xu, IEEE Photon. Technol. Lett. **16**, 503 (2004).
4. J. Brouckaert, W. Bogaerts, P. Dumon, D. Thourhout, and R. Baets, J. Lightwave Technol. **25**, 1269 (2007).
5. T. Mizuno, M. Oguma, T. Kitoh, Y. Inoue, and H. Takahasi, IEEE Photon. Technol. Lett. **18**, 1570 (2006).
6. F. Xia, M. Rooks, L. Sekaric, and Y. Vlasov, Opt. Express **15**, 11934 (2007).
7. P. Bock, P. Cheben, J. Schmid, A. V. Velasco, A. Delâge, S. Janz, D.-X. Xu, J. Lapointe, T. J. Hall, and M. L. Calvo, Opt. Express **20**, 19882 (2012).
8. A. V. Velasco, P. J. Bock, P. Cheben, M. L. Calvo, J. H. Schmid, J. Lapointe, D.-X. Xu, S. Janz, and A. Delâge, Electron. Lett. **48**, 715 (2012).
9. P. Cheben, I. Powell, S. Janz, and D.-X. Xu, Opt. Lett. **30**, 1824 (2005).
10. M. Florjańczyk, P. Cheben, S. Janz, A. Scott, B. Solheim, and D.-X. Xu, Opt. Express **15**, 18176 (2007).
11. J. M. Harlander, F. L. Roesler, J. G. Cardon, C. R. Englert, and R. R. Conway, Appl. Opt. **41**, 1343 (2002).
12. P. Jacquinot, J. Opt. Soc. Am. **44**, 761 (1954).
13. K. Okamoto, H. Aoyagi, and K. Takada, Opt. Lett. **35**, 2103 (2010).
14. P. Cheben, P. J. Bock, J. H. Schmid, J. Lapointe, S. Janz, D.-X. Xu, A. Densmore, A. Delâge, B. Lamontagne, and T. J. Hall, Opt. Lett. **35**, 2526 (2010).
15. K. Takada, H. Aoyagi, and K. Okamoto, Opt. Lett. **36**, 1044 (2011).
16. G. H. Golub and C. Reinsch, Numer. Math. **14**, 403 (1970).
17. A. S. Filler, J. Opt. Soc. Am. **54**, 762 (1964).

February 1, 2012 / Vol. 37, No. 3 / OPTICS LETTERS 365

Ultracompact polarization converter with a dual subwavelength trench built in a silicon-on-insulator waveguide

Aitor V. Velasco[2,4], **María L. Calvo**[2], **Pavel Cheben**[1,5], **Alejandro Ortega-Moñux**[3], **Jens H. Schmid**[1], **Carlos Alonso Ramos**[3], **Íñigo Molina Fernandez**[3], **Jean Lapointe**[1], **Martin Vachon**[1], **Siegfried Janz**[1], **and Dan-Xia Xu**[1]

[1] *Institute for Microstructural Sciences, National Research Council Canada, Ottawa, Ontario K1A 0R6, Canada*

[2] *Departamento de Optica, Facultad de Ciencias Fisicas, Universidad Complutense de Madrid, 28040 Madrid, Spain*

[3] *ETSI Telecomunicación, Universidad de Málaga, 29071 Málaga, Spain*

[4] *e-mail: avillafr@pdi.ucm.es*

[5] *e-mail: pavel.cheben@nrc.ca*

Received October 24, 2011; revised December 1, 2011; accepted December 5, 2011;
posted December 7, 2011 (Doc. ID 156835); published January 20, 2012

The design and fabrication of an ultracompact silicon-on-insulator polarization converter is reported. The polarization conversion with an extinction ratio of 16 dB is achieved for a conversion length of only 10 μm. Polarization rotation is achieved by inducing a vertical asymmetry by forming in the waveguide core two subwavelength trenches of different depths. By taking advantage of the calibrated reactive ion etch lag, the two depths are implemented using a single mask and etching process. The measured converter loss is –0.7 dB and the 3 dB bandwidth is 26 nm. © 2012 Optical Society of America

OCIS codes: 130.3120, 130.5440, 230.7380.

Recent developments in integrated silicon photonic devices have demonstrated the remarkable capabilities of the silicon-on-insulator (SOI) platform to implement a wide range of applications, such as optical interconnects [1], nonlinear photonics [2], biological sensors [3], and microspectrometers [4]. However, while the high refractive index contrast of the SOI platform is advantageous for high-density photonics integration, it comes with a drawback of largely disparate propagation characteristics for the TE- and TM-like modes. As a result, most of the photonic devices in SOI have been designed for a single mode and a single polarization, typically TE. To mimic polarization independent operation, polarization diversity schemes are typically used with the polarization splitters and rotators as the key components.

Recently, several SOI polarization rotators (also known as mode converters) have been proposed, including designs based on triangular waveguides [5], asymmetric waveguides with two etch depths [6], coupling via an intermediate multimode waveguide [7], waveguides with vertical and sloped sidewalls [8], and a combination of horizontal and vertical waveguides [9]. However, fabrication of these devices is often complex, with multiple patterning and etching steps involved. Some single-etch devices have also been reported, such as a polarization rotator based on an adiabatic taper and an asymmetrical directional coupler [10] (conversion length 100 μm), and a mode converter based on the cross-polarization coupling effect [11] (conversion length 44 μm). Additionally, mode converters with single [12] or multiple [13] trenches etched to create an asymmetric waveguide have been implemented in gallium arsenide (GaAs) waveguides, reaching a 96% mode conversion within a device of 150 μm. Some numerical simulations have also been performed in an attempt to extend the single-trench design to silicon waveguides [14].

In this Letter, we report the design and fabrication of an ultracompact dual-trench polarization rotator in SOI, with a conversion length as short as 10 μm, for a wavelength of 1.5 μm. The converter schematic is shown in Fig. 1. The converter exploits the asymmetry induced by two adjacent subwavelength trenches, resulting in two orthogonal hybrid modes (Fig. 1, inset) with optical axes rotated 45° with respect to the x and y axes, that is, hybrid modes consisting of 50% TE and 50% TM polarization. This geometry allows both hybrid modes to be excited with equal efficiency by a TE (or TM) polarized input. The two hybrid modes propagate with different propagation constants along the device, resulting in a 90° polarization rotation at each half-beat length $L_{1/2}$:

$$L_{1/2} = \frac{\pi}{\Delta\beta}, \tag{1}$$

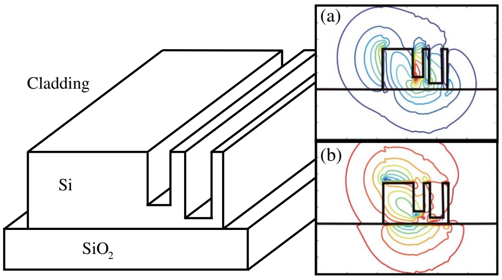

Fig. 1. (Color online) Schematic structure of the proposed polarization converter. (Inset, color online) Simulated contour plot of the (a) X and (b) Y components of the field of the first hybrid mode for a dual-trench structure with trench widths 60 nm and 85 nm and trench depths 210 nm and 235 nm, respectively.

0146-9592/12/030365-03$15.00/0

where $\Delta\beta = \beta_1 - \beta_2$ is the difference between the propagation constants of the two hybrid modes, β_1 and β_2, respectively. Additionally, in order to reach conversion efficiency values close to 100%, the power distributions of the two hybrid modes should efficiently overlap, and the higher order mode conversion needs to be minimized. Indeed, the operation mechanism of the converter ensures reciprocity between TE-TM and TM-TE mode conversion. The dual-trench structure is chosen, as opposed to a single-trench design, in order to optimize mode conversion and dramatically reduce device length.

To design the polarization rotator, we define a dual-trench subwavelength structure in the waveguide with variable depths and widths, and we perform two-dimensional (2D) mode computation with a commercial software (FIMMWAVE, Photon Design, UK). The full width of the Si-wire waveguide was chosen as 450 nm, for single mode operation near 1.5 μm wavelength. The Figure 1 inset shows the calculated hybrid mode profiles for this geometry. 2 μm-long linear inverse taper mode adaptation sections were included at both ends of the polarization rotator to ensure a smooth transition between the wire waveguide and the dual-trench waveguide, and to generate equal excitation of the two hybrid modes.

Insofar as the width and depth of the two trenches are considered independent design parameters, modes with a 45° offset can be obtained for many combinations of these parameters (Fig. 2(a)). For a given wavelength, greater trench widths require shallower trench depths and result in shorter conversion lengths (Fig. 2(b)). Also, a greater disparity in the depths of the two trenches results in greater conversion lengths (Fig. 2(c)). Simulations predict that if the width and depth of one of the trenches are increased, the size of the other trench has to be reduced to achieve maximum conversion efficiency, and conversion length is altered. The problem to minimize the device size and/or to maximize the conversion efficiency can be solved numerically. However, only a restricted set of solutions is suitable for device fabrication. In order to fabricate two narrow trenches of different depths using a single-etch step, we take advantage of the reactive ion etch (RIE) lag effect, i.e., the etch depth dependence on the trench width for small feature sizes.

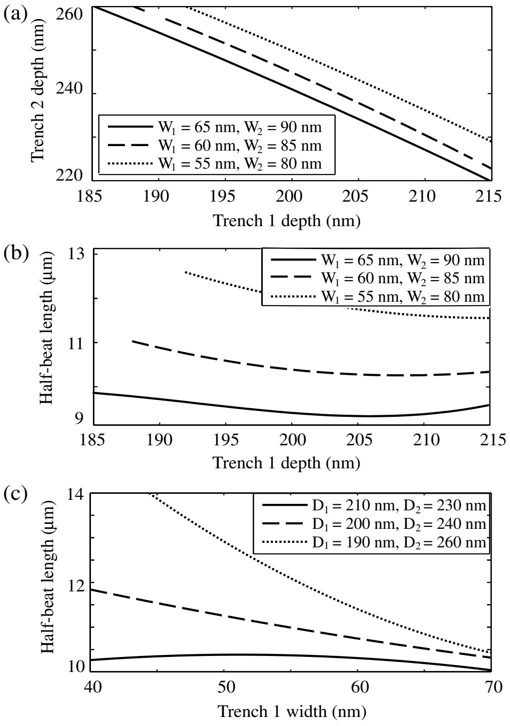

Fig. 2. (a) Combinations of trench depths (D_1, D_2) that yield hybrid modes with 45° offset, for different combinations of trench widths (W_1, W_2). (b) $L_{1/2}$ versus depth of the first trench and (c) $L_{1/2}$ versus width of the first trench, for parameter combinations yielding hybrid modes with 45° offset.

For our fabrication process, a reduced etched depth is observed for a feature size smaller than ~140 nm. We calibrated the RIE lag effect using scanning electron microscopy (SEM) measurements on a set of reference trenches of varying width, obtaining the calibration curves shown in inset of Fig. 3. By applying the calibration curve to the set of theoretical solutions for trench widths and depths yielding hybrid modes with 45° offset, we found the optimized values for the two trench widths of 60 nm and 85 nm and trench depths of 210 nm and 230 nm, respectively. This structure yields a final device length of 10.3 μm. Parameter combinations that result in shorter conversion lengths cannot be fabricated, as they do not match the RIE lag calibration curve, and resulting trench depths would be too shallow.

The operation wavelength can be increased by increasing the trench width and depth and/or the overall device length. According to our dimension tolerance study, a 13 nm shift of the design central wavelength is predicted for fabrication errors of 9 nm in the depths of the trenches or 5 nm in the widths of the trenches. Our calculations show that the design can be optimized for 1550 nm wavelength by enlarging the outer trench to a width of 90 nm and a depth of 240 nm. For that wavelength and topology, conversion length is increased to 12.74 μm.

Samples were fabricated using SOI substrates with a 0.26 μm thick silicon and a 2 μm thick buried oxide layer. Waveguides with the polarization rotator structure were defined in a single patterning step by electron beam lithography with high contrast hydrogen silsesquioxane (HSQ) resist. Inductively coupled plasma reactive ion

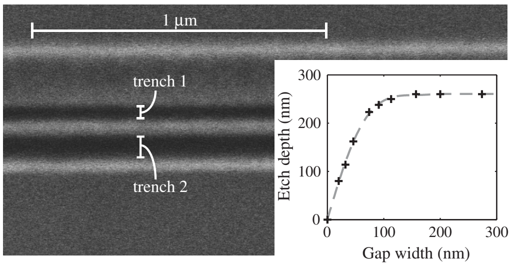

Fig. 3. SEM of the fabricated dual-trench polarization converter. (Inset) Etch depth versus gap width due to RIE lag effect.

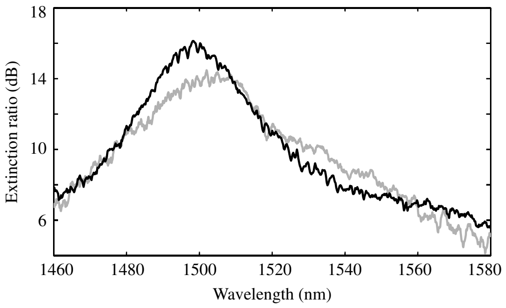

Fig. 4. Measured ER versus wavelength of the fabricated device for TE to TM (black) and TM to TE (gray) mode conversion.

etching (ICP-RIE) was used to transfer the resist pattern into the silicon layer. Figure 3 shows a SEM image of the fabricated device.

The polarization rotator was characterized using a tunable laser over a wavelength range of 1460–1580 nm, with polarization control optics. The light was coupled both at the input and the output of the chip using lens fibers facing the chip facets terminated at both sides with subwavelength grating mode converters [15]. The output signal was separated into the TE and TM components with a polarizing beam splitter, and both polarization components were measured independently.

The measured extinction ratio (Eq. (2)) is shown in Fig. 4.

$$\mathrm{ER}_{\text{TE-TM}} = 10 \cdot \log \frac{P_{\mathrm{TM}}}{P_{\mathrm{TE}}}, \tag{2}$$

where P_{TM} and P_{TE} are the output powers of the TM and TE polarized fundamental modes. Measured extinction ratio was corrected by calibrating polarization dependent loss in the 60 μm-long strip waveguide between the device and the chip facet (0.4 dB/cm excess loss for TE polarization). Furthermore, the polarization dependence of the output coupling efficiency between the subwavelength grating mode converter and the lensed fiber of the light collecting system was compensated (0.3 dB excess loss for TM polarization). Polarization conversion effects in the subwavelength grating mode converter were calibrated by performing polarization-resolved measurements of a bare waveguide with the mode transformers, showing that polarization was maintained with an extinction ratio exceeding 35 dB. Polarization conversion effects in the adaptation stages were characterized by measuring the polarization rotation angle for a set of test devices with different lengths, showing a rotation in the adaptation stage of 2°, which was corrected by a 0.22 μm reduction in the length of the rotator. Trench depths measurements of the adaptation section, determined by RIE lag effect, confirmed shallow trenches during most of the adaptation stage.

The peak extinction ratio for TE-TM conversion is 16 dB (97.5% conversion efficiency, defined as $\eta_{\text{TE-TM}} = P_{\mathrm{TM}}/[P_{\mathrm{TM}} + P_{\mathrm{TE}}] \times 100\%$) at the nominal wavelength of 1500 nm. A peak extinction ratio of 14 dB is observed for TM-TE conversion, showing a slight drop due to polarization dependent losses in the device and to fabrication imperfections. The measured extinction ratio 3 dB bandwidth is 26 nm, while a conversion efficiency over 90% is reached within a bandwidth of 47 nm. Polarization converter loss was estimated by subtracting the insertion loss of a reference waveguide without a polarization converter, to compensate for the fiber-chip coupling losses and the loss of the Si-wire interconnecting waveguide. The measured polarization converter excess loss is −0.7 dB, with an adaptation stage excess loss of −0.4 dB.

In conclusion, we have demonstrated the design and fabrication of an ultracompact and efficient polarization rotator using a dual subwavelength trench in an Si-wire waveguide. The device is implemented in a single-etch step standard fabrication process. Extinction ratios up to 16 dB were reached for an ultrashort conversion length of 10 μm, opening promising prospects for device applications for efficient polarization management in integrated optoelectronic circuits.

Financial support from the Spanish Ministry of Science and Innovation (MICINN) is acknowledged under grants TEC2008-04105 and TEC2009-10152.

References

1. A. Liu, L. Liao, Y. Chetrit, J. Basak, H. Nguyen, D. Rubin, and M. Paniccia, in *Proceedings of the Fifth International Conference on Group IV Photonics* (2008), pp. 368–370.
2. M. A. Foster, A. C. Turner, J. E. Sharping, B. S. Schmidt, M. Lipson, and A. L. Gaeta, Nature **441**, 960 (2006).
3. A. Densmore, D.-X. Xu, P. Waldron, S. Janz, P. Cheben, J. Lapointe, A. Delâge, B. Lamontagne, J. H. Schmid, and E. Post, IEEE Photon. Technol. Lett. **18**, 2520 (2006).
4. P. Cheben, J. H. Schmid, A. Delâge, A. Densmore, S. Janz, B. Lamontagne, J. Lapointe, E. Post, P. Waldron, and D.-X. Xu, Opt. Express **15**, 2299 (2007).
5. J. Yamauchi, M. Yamanoue, and H. Nakano, J. Lightwave Technol. **26**, 1708 (2008).
6. D. Vermeulen, S. Selvaraja, W. Bogaerts, and G. Roelkens, presented at the Seventh International Conference on Group IV Photonics, Beijing, China, 2010, paper WC6
7. Y. Yue, L. Zhang, M. Song, R. G. Beausoleil, and A. E. Willner, Opt. Express **17**, 20694 (2009).
8. C. Brooks, P. E. Jessop, H. Deng, D. O. Yevick, and G. Tarr, Opt. Eng. **45**, 044603 (2006).
9. J. Zhang, T. Y. Liow, M. Yu, G. Q. Lo, and D. L. Kwong, Opt. Express **18**, 25264 (2010).
10. D. Dai and J. E. Bowers, Opt. Express **19**, 10940 (2011).
11. L. Liu, Y. Ding, K. Yvind, and J. M. Hvam, Opt. Lett. **36**, 1059 (2011).
12. S. H. Kim, R. Takei, Y. Shoji, and T. Mizumoto, Opt. Express **17**, 11267 (2009).
13. B. M. Holmes and D. C. Hutchings, IEEE Photon. Technol. Lett. **18**, 43 (2006).
14. D. M. H. Leung, B. M. A. Rahman, and K. T. V. Grattan, IEEE Photon. J. **3**, 381 (2011).
15. P. Cheben, P. J. Bock, J. H. Schmid, J. Lapointe, S. Janz, D.-X. Xu, A. Densmore, A. Delâge, B. Lamontagne, and T. J. Hall, Opt. Lett. **35**, 2526 (2010).

Demonstration of a curved sidewall grating demultiplexer on silicon

Przemek J. Bock,[1,*] Pavel Cheben,[1] Jens H. Schmid,[1] Aitor V. Velasco,[2] André Delâge,[1] Siegfried Janz,[1] Dan-Xia Xu,[1] Jean Lapointe,[1] Trevor J. Hall,[3] and María L. Calvo[2]

[1]Institute for Microstructural Sciences, National Research Council Canada, Ottawa, Canada
[2]Complutense University of Madrid, Madrid, Spain
[3]Centre for Research in Photonics, University of Ottawa, Ottawa, Canada
[*]przemek.bock@sympatico.ca

Abstract: We experimentally demonstrate a new type of waveguide multiplexer device designed for silicon photonics, with a crosstalk level as low as −35 dB and an operational wavelength range of 300 nm. A compact device footprint of only 100 × 160 μm^2 offers an excellent potential for integration with other silicon nanophotonic circuits.

OCIS codes: (130.3120) Integrated optics devices; (050.1950) Diffraction gratings; (050.6624) Subwavelength structures.

References and links

1. C. R. Doerr and K. Okamoto, “Advances in silica planar lightwave circuits,” J. Lightwave Technol. **24**(12), 4763–4789 (2006).
2. P. Cheben, “Wavelength dispersive planar waveguide devices: echelle gratings and arrayed waveguide gratings,” *Optical waveguides: from theory to applied technologies*, M. L. Calvo and V. Lakshminarayanan, Eds. (CRC Press, 2007), 173–230.
3. A. Alduino and M. Paniccia, “Interconnects: wiring electronics with light,” Nat. Photonics **1**(3), 153–155 (2007).
4. B. Jalali, “Teaching silicon new tricks,” Nat. Photonics **1**(4), 193–195 (2007).
5. R. Kirchain and L. Kimerling, “A roadmap for nanophotonics,” Nat. Photonics **1**(6), 303–305 (2007).
6. P. Cheben, J. H. Schmid, A. Delâge, A. Densmore, S. Janz, B. Lamontagne, J. Lapointe, E. Post, P. Waldron, and D.-X. Xu, “A high-resolution silicon-on-insulator arrayed waveguide grating microspectrometer with sub-micrometer aperture waveguides,” Opt. Express **15**(5), 2299–2306 (2007).
7. F. Xia, L. Sekaric, and Y. Vlasov, “Ultracompact optical buffers on a silicon chip,” Nat. Photonics **1**(1), 65–71 (2007).
8. J. S. Levy, A. Gondarenko, M. A. Foster, A. C. Turner-Foster, A. L. Gaeta, and M. Lipson, “CMOS-compatible multiple-wavelength oscillator for on-chip optical interconnects,” Nat. Photonics **4**(1), 37–40 (2010).
9. H. A. Rowland, “Preliminary notice of results accomplished on the manufacture and theory of gratings for optical purposes,” Phil. Mag. Suppl. **13**(84), 469–474 (1882).
10. R. Nagarajan, M. Kato, J. Pleumeekers, P. Evans, S. Corzine, S. Hurtt, A. Dentai, S. Murthy, M. Missey, R. Muthiah, R. A. Salvatore, C. Joyner, R. Schneider, M. Ziari, F. Kish, and D. Welch, “InP Photonic Integrated Circuits,” IEEE J. Sel. Top. Quantum Electron. **16**(5), 1113–1125 (2010).
11. X. Leijtens and M. Smit, “Miniaturization of Passive Devices for Photonic Integration,” Proc. SPIE **6020**, 60201Q (2005).
12. M. R. T. Pearson, A. Bezinger, A. Delâge, J. W. Fraser, S. Janz, P. E. Jessop, and D.-X. Xu, “Arrayed waveguide grating demultiplexers in silicon-on-insulator,” Proc. SPIE **3953**, 11–18 (2000).
13. F. Ohno, K. Sasaki, A. Motegi, and T. Baba, “Reduction in Sidelobe Level in Ultracompact Arrayed Waveguide Grating Demultiplexer Based on Si Wire Waveguide,” Jpn. J. Appl. Phys. **45**(8A), 6126–6131 (2006).
14. P. Dumon, W. Bogaerts, D. Van Thourhout, D. Taillaert, R. Baets, J. Wouters, S. Beckx, and P. Jaenen, “Compact wavelength router based on a Silicon-on-insulator arrayed waveguide grating pigtailed to a fiber array,” Opt. Express **14**(2), 664–669 (2006).
15. X. Liu, I. Hsieh, X. Chen, M. Takekoshi, J. I. Dadap, N. C. Panoiu, R. M. Osgood Jr., W. M. Green, F. Xia, and Y. A. Vlasov, “Design and fabrication of an ultra-compact silicon on insulator demultiplexer based on arrayed waveguide gratings,” CLEO 2008, paper CTuNN1.
16. S. Pathak, E. Lambert, P. Dumon, D. Thourhout, and W. Bogaerts, “Compact SOI-Based AWG With Flattened Spectral Response Using a MMI,” 8th International Conference in Group IV Photonics 2011, paper WC2.
17. S. Janz, A. Balakrishnan, S. Charbonneau, P. Cheben, M. Cloutier, A. Delâge, K. Dossou, L. Erickson, M. Gao, P. A. Krug, B. Lamontagne, M. Packirisamy, M. Pearson, and D.-X. Xu, “Planar waveguide echelle gratings in silica-on-silicon,” IEEE Photon. Technol. Lett. **16**(2), 503–505 (2004).
18. S. Bidnyk, D. Feng, A. Balakrishnan, M. Pearson, M. Gao, H. Liang, W. Qian, C.-C. Kung, J. Fong, J. Yin, and M.

#167409 - $15.00 USD Received 27 Apr 2012; revised 24 Jul 2012; accepted 30 Jul 2012; published 15 Aug 2012

Asghari, "Silicon-on-insulator-based planar circuit for passive optical network applications," IEEE Photon. Technol. Lett. **18**(22), 2392–2394 (2006).
19. J. Brouckaert, W. Bogaerts, P. Dumon, D. Thourhout, and R. Baets, "Planar concave grating demultiplexer fabricated on a nanophotonic silicon-on-insulator platform," J. Lightwave Technol. **25**(5), 1269–1275 (2007).
20. D. Feng, N.-N. Feng, C.-C. Kung, H. Liang, W. Qian, J. Fong, B. J. Luff, and M. Asghari, "Compact single-chip VMUX/DEMUX on the silicon-on-insulator platform," Opt. Express **19**(7), 6125–6130 (2011).
21. K. Okamoto, "Fundamentals of optical waveguides," Elsevier Inc., 2006.
22. R. Soref, "Reconfigurable integrated optoelectronics," Adv. Optoelectron. **2011**, 1–15 (2011), doi:10.1155/2011/627802.
23. F. Xia, M. Rooks, L. Sekaric, and Y. Vlasov, "Ultra-compact high order ring resonator filters using submicron silicon photonic wires for on-chip optical interconnects," Opt. Express **15**(19), 11934–11941 (2007).
24. N. Han-Yong, R. W. Michael, L. Daqun, W. Xuan, M. Jose, R. P. Roberto, and P. Kachesh, "4 x 4 wavelength reconfigurable photonic switch based on thermally tuned silicon microring resonators," Opt. Eng. **47**(4), 0446011–0666018 (2008).
25. N. Sherwood-Droz, H. Wang, L. Chen, B. G. Lee, A. Biberman, K. Bergman, and M. Lipson, "Optical 4x4 hitless slicon router for optical networks-on-chip (NoC)," Opt. Express **16**(20), 15915–15922 (2008).
26. X. Zheng, I. Shubin, G. Li, T. Pinguet, A. Mekis, J. Yao, H. Thacker, Y. Luo, J. Costa, K. Raj, J. E. Cunningham, and A. V. Krishnamoorthy, "A tunable 1x4 silicon CMOS photonic wavelength multiplexer/demultiplexer for dense optical interconnects," Opt. Express **18**(5), 5151–5160 (2010).
27. Y. H. Wen, O. Kuzucu, T. Hou, M. Lipson, and A. L. Gaeta, "All-optical switching of a single resonance in silicon ring resonators," Opt. Lett. **36**(8), 1413–1415 (2011).
28. C. K. Madsen, J. Wagener, T. A. Strasser, D. Muehlner, M. A. Milbrodt, E. J. Laskowski, and J. DeMarco, "Planar waveguide optical spectrum analyzer using a UV-induced grating," IEEE J. Sel. Top. Quantum Electron. **4**(6), 925–929 (1998).
29. Y. Hao, Y. Wu, J. Yang, X. Jiang, and M. Wang, "Novel dispersive and focusing device configuration based on curved waveguide grating (CWG)," Opt. Express **14**(19), 8630–8637 (2006).
30. P. J. Bock, P. Cheben, A. Delâge, J. H. Schmid, D.-X. Xu, S. Janz, and T. J. Hall, "Demultiplexer with blazed waveguide sidewall grating and sub-wavelength grating structure," Opt. Express **16**(22), 17616–17625 (2008).
31. C. F. R. Mateus, M. C. Y. Huang, L. Chen, C. J. Chang-Hasnain, and Y. Suzuki, "Broad-band mirror (1.12-1.62 um) using a subwavelength grating," IEEE Photon. Technol. Lett. **16**(7), 1676–1678 (2004).
32. P. Cheben, D.-X. Xu, S. Janz, and A. Densmore, "Subwavelength waveguide grating for mode conversion and light coupling in integrated optics," Opt. Express **14**(11), 4695–4702 (2006).
33. P. Cheben, P. J. Bock, J. H. Schmid, J. Lapointe, S. Janz, D.-X. Xu, A. Densmore, A. Delâge, B. Lamontagne, and T. J. Hall, "Refractive index engineering with subwavelength gratings for efficient microphotonic couplers and planar waveguide multiplexers," Opt. Lett. **35**(15), 2526–2528 (2010).
34. R. Halir, P. Cheben, J. H. Schmid, R. Ma, D. Bedard, S. Janz, D.-X. Xu, A. Densmore, J. Lapointe, and I. Molina-Fernández, "Continuously apodized fiber-to-chip surface grating coupler with refractive index engineered subwavelength structure," Opt. Lett. **35**(19), 3243–3245 (2010).
35. U. Levy, M. Abashin, K. Ikeda, A. Krishnamoorthy, J. Cunningham, and Y. Fainman, "Inhomogenous Dielectric Metamaterials with Space-Variant Polarizability," Phys. Rev. Lett. **98**(24), 243901 (2007).
36. J. H. Schmid, P. Cheben, S. Janz, J. Lapointe, E. Post, and D.-X. Xu, "Gradient-index antireflective subwavelength structures for planar waveguide facets," Opt. Lett. **32**(13), 1794–1796 (2007).
37. F. Horst, W. M. Green, B. J. Offrein, and Y. Vlasov, "Echelle grating WDM (de-)multiplexer in SOI technology, based on a design with two stigmatic points," Proc. SPIE **6996**, 69960R, (2008).

1. Introduction

Presently, two types of passive waveguide multiplexer and router technologies, namely array waveguide gratings and echelle gratings, are used as fundamental building blocks for wavelength division multiplexed communications [1,2]. Although remarkable progress has been achieved in these complex integrated optical circuits, with applications recently extending from telecom to optical interconnects [3–5] and spectroscopy [6], the best performance is still achieved using conventional glass waveguide technology. While multiplexer optical quality remains unrivalled in silica glass waveguides, such devices are several orders of magnitude larger than multiplexers based on silicon nanophotonic waveguides. With advanced silicon nanophotonic components rapidly emerging, including optical memories, buffers [7] and light sources [8], small footprint multiplexers are a key component in the commercial realization of silicon photonic circuit technology.

Planar waveguide multiplexers use a wavelength dispersive element to spatially separate different spectral bands. Such a dispersive element is implemented in a focusing geometry to collect the light of different wavelengths by an array of receiver waveguides located along the focal curve, constructed according to a geometry which minimizes wavefront aberrations,

#167409 - $15.00 USD Received 27 Apr 2012; revised 24 Jul 2012; accepted 30 Jul 2012; published 15 Aug 2012

discovered by Henry Rowland in the late 19th century [9]. The wavelength dispersive element used in an array waveguide grating (AWG) is the waveguide phased array, with a linearly increasing waveguide length across adjacent arms of the array. The waveguide array is often the single largest component of an AWG multiplexer and its phase errors limit the device performance in terms of crosstalk between different wavelength channels. A crosstalk level of −35 dB or less can be achieved in a glass AWG. Nevertheless, the large minimum bend radius of glass waveguides inevitably leads to large devices, on the order of several centimetres in size, not suitable for integration. Complex photonic integrated circuits with AWGs [10,11] were successfully built and commercialized for telecom applications using the InP waveguide platform, but no similar integration level has yet been achieved in silicon waveguides. Recently, several ultra-compact AWG multiplexers have been reported using the silicon-on-insulator high refractive index contrast (Δn ~2) material platform [12–16]. However, in such high-index-contrast waveguides, the light intensity at the core-cladding boundary is substantially increased. Normal manufacturing variations will interact with this field, resulting in an overall phase error accumulation, ultimately limiting the crosstalk performance. Conversely, the dispersive element in an echelle multiplexer is the etched waveguide grating [2,17]. Several echelle grating multiplexers have been recently reported using silicon photonic waveguides [18–20]. Operating in reflection, the efficiency and bandwidth of these devices are restricted by limited reflectivity of the etched grating facets. Furthermore, the facet reflectivity cannot be controlled (apodized) along the grating without incurring additional loss, while such apodization capability is required for advanced multiplexers with controlled passband and chromatic dispersion.

A great deal of research has been done in developing both passive and reconfigurable integrated filters [21,22]. Here we propose a new type of passive wavelength multiplexer for silicon. Silicon photonic devices have many advantages including possible low cost fabrication due to the potential compatibility with the microelectronics fabrication infrastructure, high integration potential and fabrication yield. Besides AWGs and Echelle gratings, cascaded Mach-Zehnder interferometers and ring resonator filters have been proposed [23]; however, both require exact optical path lengths and are highly sensitive to fabrication tolerance. Reconfigurable ring filters do not have this limitation, but do require an active tuning element [24–27]. Another alternative is channel waveguide gratings, which were first implemented in straight waveguides using UV induced gratings as the dispersive element while either chirping the grating [28] or curving the waveguide [29] provides the focusing property.

2. Demultiplexer operating principle

In this letter we experimentally demonstrate a new type of passive multiplexer device, which has been specifically designed for course wavelength division multiplexing (CWDM) on the silicon-on-insulator (SOI) material platform. In our demultiplexer, the dispersive element is the waveguide sidewall grating, where the light in the input waveguide is preferentially diffracted towards the focal curve by 45° blazed grating teeth. Conceptually, the light is being reflected by total internal reflection at the grating facet, where each grating tooth behaves like a small prism, thereby increasing grating diffraction efficiency into the −1st order compared to the 1st order. As the light propagates along the waveguide, each tooth acts as a Huygens wavelet source, partially dispersing the light.

The device properties can be estimated using the relationship between the grating tooth spacing and the incident and diffractive angle - the well-known grating equation. In our case, it simplifies to $\Lambda(1 + \sin\varphi_d) = m\ \lambda/n_{eff}$, where $\Lambda = |m\lambda_o/n_{eff}|$ is the grating pitch, λ_o is the center wavelength, n_{eff} is the effective index of the waveguide grating and φ_d is the diffraction angle relative to the grating. The angular dispersion is then $\Delta\varphi_d/\Delta\lambda = -m/(n_{eff}d\cos\varphi_d)$ and at $\varphi_d = 0$, becomes $\Delta\varphi_d/\Delta\lambda = 1/\lambda_o$. Likewise, the free spectral range (FSR) is $\Delta\varphi_d/\Delta m = \lambda/(n_{eff}d\cos\varphi_d)$ and at $\varphi_d = 0$ becomes $\Delta\varphi_d/\Delta m = 1/m$. Note that unlike an AWG or echelle grating, the dispersion is

#167409 - $15.00 USD Received 27 Apr 2012; revised 24 Jul 2012; accepted 30 Jul 2012; published 15 Aug 2012

independent of the order (pitch) of the grating. Therefore, to design a version of this device for dense wavelength division multiplexing (DWDM), the Rowland radius would need to be scaled accordingly to accommodate more receiver waveguides along the focal curve.

These properties are confirmed by using a 2D Kirchhoff-Huygens diffraction integral to model the device as shown in Eq. (1), where the far-field $\Psi(x', y')$ at coordinates x' and y' along the focal curve (the Rowland circle of radius R) is calculated by integrating the near-field along the curved grating path C(x,y).

$$\Psi(x', y') = \int_C \frac{\psi(x, y)\exp[-i(\phi_w + \phi_s)]}{\sqrt{\lambda d}} G dC \qquad (1)$$

The near-field profile is defined as $\psi(x, y)$ at coordinates x and y along the grating, The phase accumulated in the grating waveguide and in the slab region by the Huygens wavelet is φ_w, φ_s. In Eq. (1), λ is the wavelength, $d = [(x' - x)^2 + (y' - y)^2]^{½}$ is the distance between a grating facet (at x,y) and a given position along the focal curve (at x', y'), and the geometry factor is $G = (\cos\alpha + \cos\gamma)/2$, where α and γ are the angles between the normal of the grating facet and the incoming and outgoing light wavevector respectively. In Eq. (1) each grating facet is represented as a wavelet source, and the relative phase between sources is fixed. The facets shape the profile of the electromagnetic field near the grating, while the curvature of the waveguide focuses the wavefront onto the focal curve, where the light is intercepted by the receiver waveguides. For our device, the discretized Kirchhoff-Huygens diffraction integral, i.e. sum of light contribution from all facets j = 1,2, …, N was used in our preview study to model the device [30]. This model is summarized in Fig. 1, where the near-field along the N facets of the grating is integrated at each point along the focal curve.

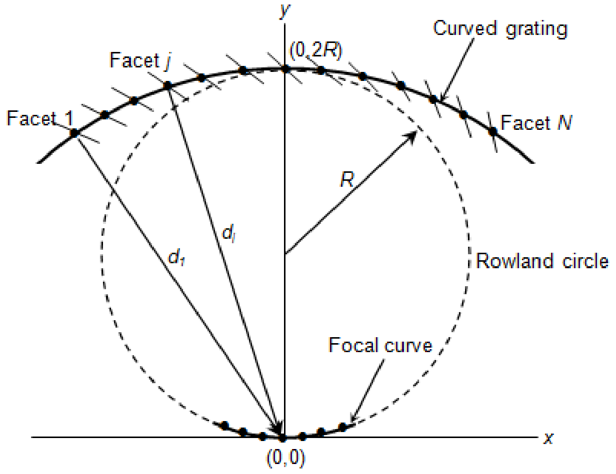

Fig. 1. Schematic of the discretized Kirchhoff-Huygens model of the sidewall grating spectrometer with N facets having a Roland radius of R. Coordinates x, y are relative to the focal curve.

Conventional passive multiplexers including AWGs (and echelle gratings) use a split-path approach, dividing the light between the array waveguides (gratings). For a given split-path, a particular array waveguide in an AWG for example, the light accumulates phase errors independent of other array waveguides. This leads to a large phase error accumulation relative to an adjacent array waveguide, even though the length different between adjacent array waveguides is only the order spacing. A key element of our design is the light propagates along the common-path of the curved sidewall grating. Therefore, unlike the split-path approach, the common-path approach results in a dependent phase error accumulation between adjacent grating facets. For example, the phase error accumulation between facet j and facet $j + 1$ only includes the order spacing between adjacent facets as the phase error accumulated up to facet j is common to both facet j and facet $j + 1$. The schematic in Fig. 2(a) shows the conventional split-path multiplexing approach used in an AWG where φ_1, φ_j, φ_{j+1} and φ_N are the phase errors accumulated along the first, j^{th}, $j^{\text{th}} + 1$ and N^{th} array waveguide (N is the total number of array waveguides). The relative phase error between the j^{th} and the $j^{\text{th}} + 1$ array waveguide is $\Delta\varphi = \varphi_{j+1} - \varphi_j$, since phase error is accumulated independently between the different array waveguides. Figure 2(b) shows a schematic of the common-path multiplexing approach used in the sidewall grating. Since the light propagates along a common path, the relative phase error between adjacent facets is $\Delta\varphi = \varphi_{j+1} - \varphi_j = (\Delta\varphi_{j,j+1} + \varphi_j) - \varphi_j = \Delta\varphi_{j,j+1}$, where $\Delta\varphi_{j,j+1}$ is the phase error accumulation between facet j and facet $j + 1$. This is theoretically a significant advantage because the phase error accumulation between adjacent facets is limited to only a single order spacing.

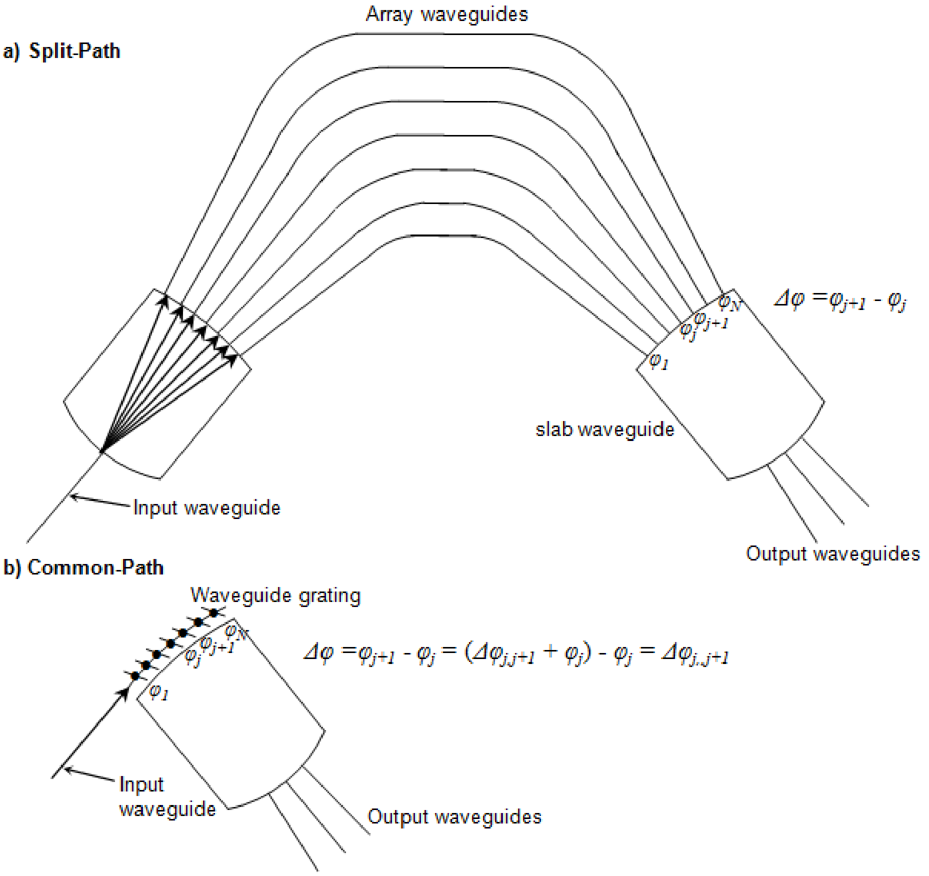

Fig. 2. a) Schematic of the conventional split-path multiplexing approach used in an AWG where φ_1, φ_j, φ_{j+1} and φ_N are the phase errors accumulated along the first, j^{th}, $j^{\text{th}} + 1$ and N^{th} array waveguide (N is the total number of array waveguides). The relative phase error between the j^{th} and the $j^{\text{th}} + 1$ array waveguide is $\Delta\varphi = \varphi_{j+1} - \varphi_j$, since phase error is accumulated independently between the different array waveguides. b) Schematic of the common-path multiplexing approach used in the sidewall grating. Since the light propagates along a common path, the relative phase error between adjacent facets will be $\Delta\varphi = \varphi_{j+1} - \varphi_j = (\Delta\varphi_{j,j+1} + \varphi_j) - \varphi_j = \Delta\varphi_{j,j+1}$, where $\Delta\varphi_{j,j+1}$ is the phase error accumulation between facet j and facet $j + 1$.

3. Design and fabrication

The geometry of the Rowland configuration was determined as follows. At the Rowland circle, the receiver waveguide width and pitch of 1.4 µm and 2.4 µm respectively, were chosen to ensure compact size yet avoid mode delocalization and minimize receiver-limited crosstalk. For such a receiver waveguide, the numerical aperture angular full width is 40.1° from 3D FDTD simulations, measured at $1/e^2$ irradiance asymptotes. For a L = 100 µm long curved sidewall grating, 40.1° angular width corresponds to a focal length of f = 140 µm, thus a Rowland circle radius of R = 70 µm. This geometry ensures that the numerical aperture of the receiver waveguides is matched to the numerical aperture of the curved waveguide grating equivalent lens.

For the 21-channel device, the sidewall grating pitch is $\Lambda = |m\lambda_o/n_{\mathrm{eff}}| = 0.512$ µm, where $m = -1$ is the grating order, $\lambda_0 = 1.44$ µm is the center wavelength and $n_{\mathrm{eff}} = 2.81$ is the effective index of the curved waveguide for TE polarization. For the two-pass filter created by cascading two 11-channel devices, the sidewall grating pitch is $\Lambda = |m\lambda_o/n_{\mathrm{eff}}| = 0.561$ µm, where $m = -1$, $\lambda_0 = 1.55$ µm and $n_{\mathrm{eff}} = 2.76$. Effective index was determined by using a FDTD mode solver for a 0.6 µm × 0.26 µm silicon waveguide ($n_{\mathrm{Si}} = 3.476$) on a silica substrate ($n_{\mathrm{SiO2}} = 1.444$) with an SU-8 cladding ($n_{\mathrm{SU\text{-}8}} = 1.58$). The apodized grating has an initial modulation depth of 0.03 µm, which increases to the maximum depth of 0.3 µm over the first 70 µm of the grating. The apodization function is $d = d_0\exp(-x^2/2\sigma^2)$, where d_0 is twice the maximum modulation depth, x is the position along the grating and σ = 60 µm is the variance of the Gaussian function. Maximum grating depth (0.3 µm) is used for the remaining 30 µm of grating length. The grating pitch varies according to the modulation depth by $\delta\Lambda = d^2(n_{\mathrm{Si}} - n_{\mathrm{SU8}})/2wn_{\mathrm{Si}}$, where $\delta\Lambda$ is the required change in pitch, d is the modulation depth, w = 0.6 µm is the waveguide width and n_{Si}, n_{SU8} are the refractive indices of silicon and SU-8 polymer. These parameters result in a curved waveguide with 183 blazed grating teeth. Triangular subwavelength grating nanostructure with a 1 µm width and a 0.25 µm pitch was used as a transition between the waveguide grating and the slab waveguide, resulting in a total of 400 subwavelength grating periods.

We used commercially available SOI substrates with 0.26-µm-thick silicon and 2-µm-thick buried oxide (BOX) layers. Electron beam lithography was used to define the waveguide layout in high contrast hydrogen silsesquioxane (HSQ) resist, which formed SiO_2 upon electron beam exposure. We used inductively coupled plasma reactive ion etching (ICP-RIE) to transfer the waveguide layout onto the silicon layer. Samples were coated with a 2 µm thick polymer (SU-8, $n_{\mathrm{SU\text{-}8}} \sim 1.58$ at $\lambda = 1.55$ µm), then cleaved into separate chips and facets polished. Chips were approximately 6.1 mm long. Figure 3(a) shows an optical microscope image of the fabricated 21-channel spectrometer, while Fig. 3(b) shows a scanning electron microscope close-up of the grating detail. Scanning electron microscope images showed a 50 nm offset from the desired dimensions, which we attribute to insufficient correction of the proximity effect.

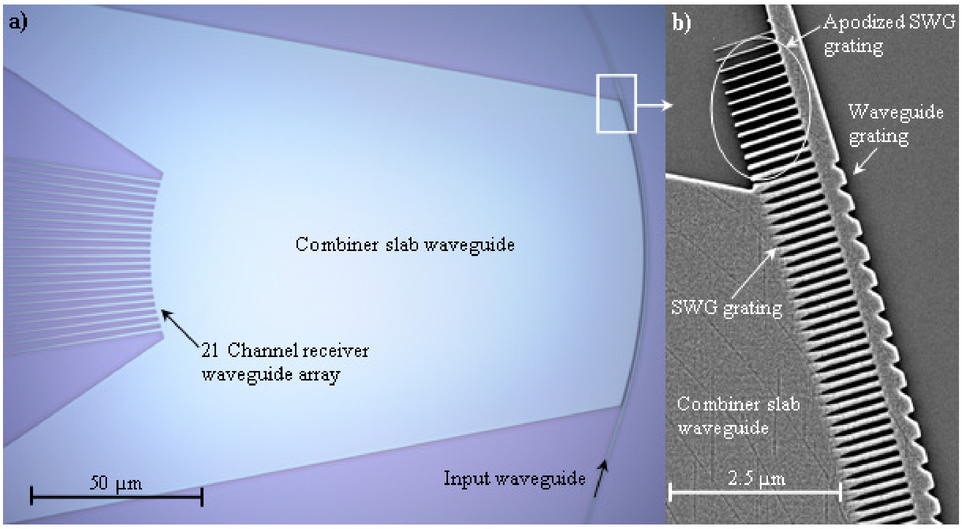

Fig. 3. a) Optical image of the sidewall grating spectrometer showing the input waveguide and the 21-channel output receiver waveguide array. b) Scanning electron microscope image close-up of the blazed waveguide grating and subwavelength grating (SWG) nanostructure detail.

4. Experimental results

A polarization controller with a broadband tunable external cavity semiconductor laser (Santec) was used to measure transmission spectra (λ = 1.23 – 1.63 µm). To couple the light into the chip, we used a lensed fiber resulting in a Gaussian beam waist of ~2 µm and an on-chip subwavelength grating fiber-chip coupler. Light is coupled out of the chip using an identical subwavelength grating coupler and subsequently focused by a microscope objective lens onto an InGaAs photodetector. The intrinsic loss of the device was measured with test multiplexers designed to calibrate out waveguide propagation loss and input/output coupling loss in the intrinsic loss measurement.

For efficient coupling to the receiver waveguides, the field distribution at the focal curve must match the modal field of the output receiver waveguide. Since the mode profile of a waveguide is nearly Gaussian, a Gaussian distribution in the grating near-field is required to ensure the far-field matching condition at the focal curve. This is achieved by apodizing the depth of the sidewall grating teeth to reshape an exponential diffracted near-field into a Gaussian diffraction profile, while simultaneously minimizing back-reflections by creating a smooth transition from the waveguide to the waveguide grating. The apodization function used is $d = d_0\exp(-x^2/2\sigma^2)$, where d_0 is the maximum grating modulation depth, x is the position along the grating and σ is the variance of the Gaussian function. Once the maximum grating modulation depth is reached, a constant grating modulation depth interacts with the diminished waveguide mode intensity to create the tail of the field profile diffracted near the end of the grating. Figure 4(a) shows a comparison of the spectra between the nominal apodized spectrometer (grey curves), and a test spectrometer (coloured curves) without the apodization for a constant grating modulation depth of 300 nm, indicating significantly reduced loss and crosstalk for the nominal design.

#167409 - $15.00 USD Received 27 Apr 2012; revised 24 Jul 2012; accepted 30 Jul 2012; published 15 Aug 2012

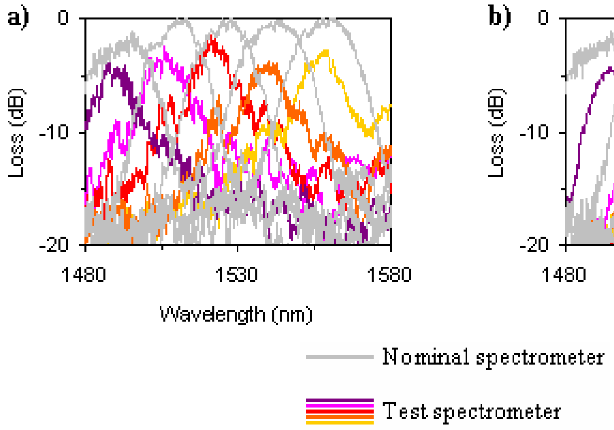

Fig. 4. Comparison of the transmission spectra for TE polarization between a nominal (apodized and chirped) spectrometer (grey) and a test spectrometer (colored) a) without apodization for a constant modulation depth of 300 nm, indicating poor crosstalk performance and b) without the subwavelength anti-reflective nanostructure, indicating a 4 dB loss penalty.

However, varying the modulation depth of the grating produces a corresponding change in the effective index of each grating segment, resulting in a phase-front distortion and a broadening of the far-field [30]. We eliminated the phase-front errors by chirping the grating to ensure a constant effective index for the entire length of the apodized grating. A simple geometric relation was used to calculate the required compensatory chirp for a given modulation depth, namely $\delta\Lambda = d^2(n_{\mathrm{Si}} - n_{\mathrm{SU8}})/2wn_{\mathrm{Si}}$ from the previous section. The validity of this relation was confirmed by finite-difference time-domain (FDTD) simulations [30]. The ability to use apodization and chirping to control both the amplitude and the phase of the near-field profile facilitates freedom in tailoring the device pass-band and chromatic dispersion [2]. In existing technologies like echelle gratings, no efficient method to control the field amplitude distribution is known (it would require varying the reflectivity of the echelle facets, leading to loss), while in an AWG this would demand either gain or attenuation in the waveguide phased array.

Fundamental to the operation of our sidewall grating multiplexer is a subwavelength nanostructure between the sidewall grating waveguide and the slab waveguide. Such a nanostructure provides confinement to ensure the channel waveguide with the sidewall grating supports a fundamental transverse mode, while simultaneously acting as a transparent waveguide boundary in the direction normal to the channel waveguide, which results in efficient coupling to the slab waveguide. Subwavelength high-index contrast gratings were first proposed as high-reflectivity mirrors [31] fiber-chip couplers [32–34] and lenses [35]. While subwavelength gratings have been used as a cladding in silicon waveguides, anti-reflective structures [36,37] and planar waveguides, this is the first demonstration of their threefold use: acting simultaneously as a waveguide cladding, an anti-reflective boundary and a slab waveguide. Our device uses 400 periods of the subwavelength nanostructure between the grating waveguide and the combiner slab waveguide. The effect of the subwavelength nanostructure is shown in Fig. 4(b) by comparing the spectral response of the nominal spectrometer (with the nanostructure) to a test spectrometer with a 1-µm-wide trench between the waveguide grating and the slab waveguide. By using the subwavelength grating, there is a remarkable 4 dB loss reduction indicating that this nanostructure facilitates efficient transitions between very different waveguide geometries, even in a high refractive index contrast material platform such as SOI. Our subwavelength nanostructures were apodized on both ends of the blazed sidewall grating to prevent Fresnel reflections as the mode couples from the input waveguide to the waveguide grating section, as shown in Fig. 3(b).

The spectral response of the multiplexer is shown in Fig. 5 indicating a crosstalk of 20-25 dB with a channel spacing of $\Delta\lambda = 15$ nm over a wavelength range of $\lambda = 1330 - 1630$ nm. Using specifically designed test multiplexers, an intrinsic device loss (including diffraction loss, coupling loss from the waveguide grating to the slab waveguide and excess loss due to field mismatch at receiver waveguides) is measured to be 3-4 dB. Reduction in performance at short wavelengths is a result of approaching the band gap of our subwavelength grating fiber-chip coupler [33]. Compared to other microphotonic multiplexers [13–16], our device has better crosstalk performance (compared with 13 dB [13], 12 dB [14], 5-10 dB [15], and 17 dB crosstalk [16]) and a far broader operational bandwidth of 300 nm (compared with 140 nm [13], 30 nm [14], 1.5 nm [15], and 40 nm bandwidth [16]). The device footprint is only 100 × 160 μm^2 making it one of the smallest wavelength multiplexers. Since the device is so small, it can easily be cascaded to form a two-pass wavelength filter as shown in the optical image in Fig. 6.

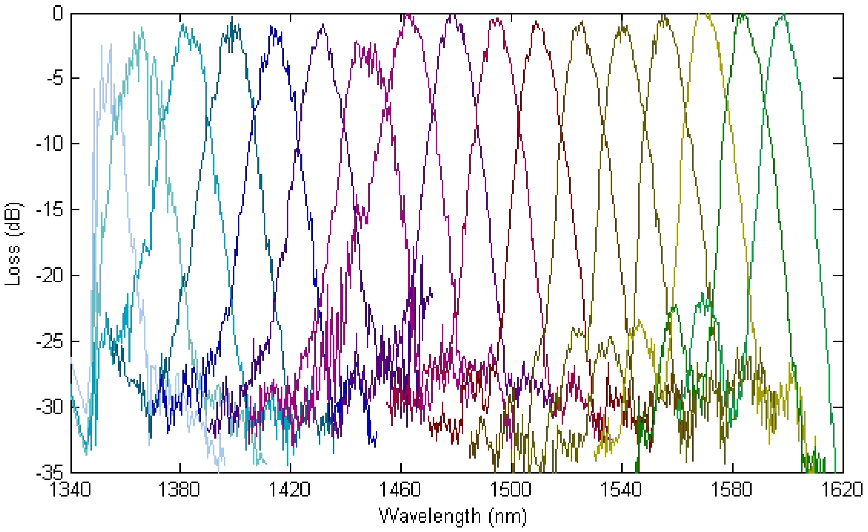

Fig. 5. Transmission spectrum of the nominal spectrometer for TE polarization for a wavelength range of $\lambda = 1340 - 1620$ nm.

#167409 - $15.00 USD Received 27 Apr 2012; revised 24 Jul 2012; accepted 30 Jul 2012; published 15 Aug 2012

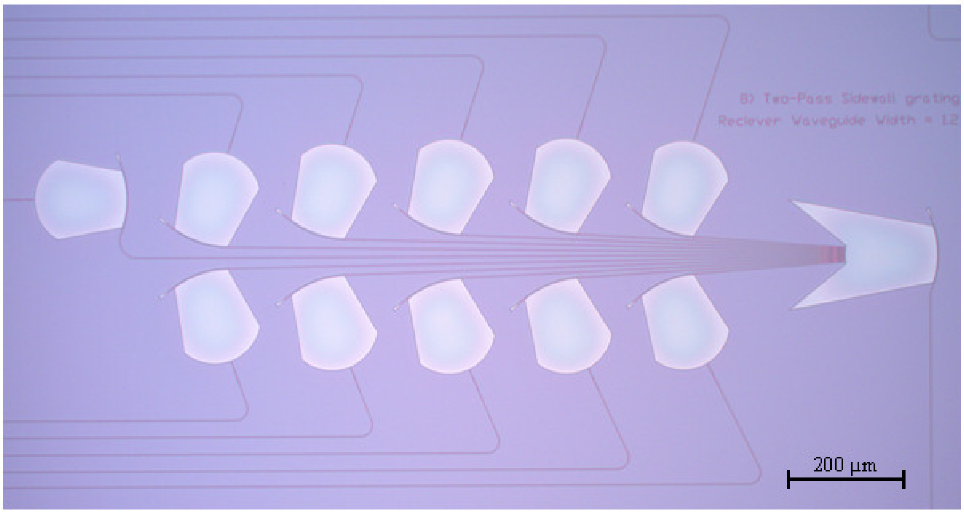

Fig. 6. Optical image of the two-pass spectral filter formed by cascading two 11 channel sidewall grating spectrometers.

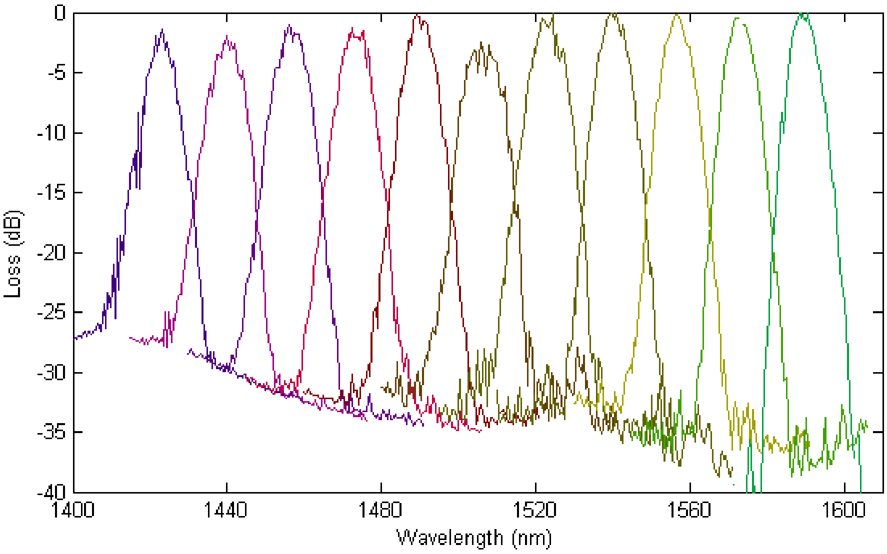

Fig. 7. Transmission spectrum of the two-pass spectrometer for a wavelength range of λ = 1400 – 1600 nm (TE polarization).

The input light is first spectrally filtered by an 11 channel multiplexer and subsequently passes through another identical device with a single receiver waveguide for the specific wavelength channel. To minimize connectivity complexity, we terminated the multiplexer blazed grating waveguides with a taper (width 0.6 μm to 5 μm) to expand the waveguide mode into a SWG anti-reflection structure, to divert any residual light away from the output facet of the chip. Figure 7 shows the spectral response of the two-pass multiplexer indicating an excellent crosstalk performance reaching −35 dB at longer wavelengths (1560 – 1600 nm). Some increase in the noise floor at short wavelengths appears to be caused by approaching the fiber-to-chip SWG coupler band gap [19]. This can be avoided by selecting a shorter periodicity for SWG coupler to move its band gap outside the short wavelength range of the sidewall grating spectrometer.

Our multiplexer channel spacing is targeting course wavelength division for interconnect applications. To accommodate the dense wavelength division of telecommunication applications, our device would need to be upscaled by a factor of $\Delta\lambda/\Delta\lambda_{DWDM}$ ~19 for a spacing of 100 GHz.

5. Conclusion

These results suggest that the sidewall grating multiplexer can achieve comparable performance to established technologies such as AWGs and echelle gratings. In particular the very small size, the low crosstalk, the broadband operation and the freedom in pass-band tailoring lend themselves well to promising applications in optical interconnects. Specifically, the small footprint combined with the large operation bandwidth is a possible solution for coarse wavelength division multiplexing. Theoretically, our device minimizes phase error accumulation by implementing a common-path approach.

These results also suggest that subwavelength nanostructures can be advantageously used in demultiplexing planar waveguide circuits to simultaneously provide multiple functions including anti-reflection, coupling from grating waveguide to slab waveguide and confinement of the waveguide grating mode. The subwavelength nanostructures provide an excellent means to engineer materials with different effective refractive indexes not limited to those typically used in silicon-based microfabrication process, simply by changing the nanostructure geometry.

#167409 - $15.00 USD Received 27 Apr 2012; revised 24 Jul 2012; accepted 30 Jul 2012; published 15 Aug 2012

Bandpass filter implemented with blazed waveguide sidewall gratings in silicon-on-insulator

A.V. Velasco, P.J. Bock, P. Cheben, M.L. Calvo,
J.H. Schmid, J. Lapointe, D.-X. Xu, S. Janz and A. Delâge

The fabrication and experimental characterisation of a two-stage bandpass filter based on curved waveguide sidewall gratings is reported for the silicon-on-insulator platform. At each cascaded filtering stage, the spectral components of the input signal are dispersed by the diffraction grating formed in the sidewall of a silicon strip waveguide. Different wavelengths are focused onto different positions along the Rowland circle and the filter central wavelength is selected by a specific receiver waveguide. By using two consecutive filtering stages, both the filter passband profile and the stopband rejection ratio are substantially increased. The grating is apodised and chirped to ensure a constant effective index along the grating length to minimise phase distortions. Blazed geometry is used to maximise the diffraction efficiency to the −1st order. The device was fabricated with electron beam lithography and reactive ion etching using a single etch step. A bandwidth of 6.2 nm was measured near 1590 nm for the fabricated filter, with a roll-off of 4 dB/nm at the passband edge, and a stopband rejection of 40 dB.

Introduction: Silicon-on-insulator (SOI) high-index contrast waveguide technology enables the development of compact photonic devices with large integration densities, for applications including optical interconnects, telecommunications, biological sensing, nonlinear photonics and spectroscopy. These applications often require highly selective wavelength filtering with a small device footprint. Filters implemented with Bragg gratings [1] have been proposed, although multimode interference (MMI) couplers are required to extract the reflected signal. Ring resonators [2] exhibit a great wavelength selectivity, but their resonance conditions are highly dependent of fabrication errors and temperature variations. Other devices with larger footprints have also been implemented, such as arrayed waveguide gratings (AWGs) and echelle gratings [3], or Mach-Zehnder interferometer (MZI) lattice filters [4]. However, it remains a challenge to develop compact bandpass filters which operate in a transmission configuration and present a high stopband rejection.

The use of curved waveguides with UV induced gratings to achieve wavelength dispersion was theoretically proposed [5] to develop wavelength division multiplexing (WDM) systems more compact than AWGs and echelle gratings [3]. A new type of planar waveguide multiplexer has been proposed, based on a curved SOI sidewall waveguide grating with a blazed grating profile [6], having a simulated crosstalk of −30 dB, an operational range exceeding 370 nm and a layout size of only 90 × 140 µm. In this Letter, we adapt this sidewall waveguide grating wavelength multiplexer design [6] to achieve a highly selective bandpass filter with two cascaded stages.

Principle of operation and device design: At each stage of the bandpass filter, light is coupled into a curved silicon strip waveguide and diffracted by a sidewall grating. The diffracted light is coupled into a slab waveguide where different wavelengths are focused on different positions along the focal curve defined by the Rowland circle geometry. Light at the central wavelength $\lambda_0 = \Lambda/n_{eff}$ is collected by the receiver waveguide, where Λ is the grating pitch and n_{eff} is the effective index of the fundamental mode of the input waveguide. By judiciously designing the grating pitch and the position of the receiver waveguide, only a narrow wavelength band is transmitted. By cascading two filtering stages of the same characteristics, the resulting passband is narrowed and the stopband suppression is increased. The receiver waveguide of the first stage is coupled directly to the second stage waveguide sidewall grating, preserving a small footprint. The waveguide grating teeth are blazed in order to maximise the optical power diffracted towards the receiver waveguides of the −1st diffracted order.

At both filtering stages the blazed sidewall grating has a length of 100 µm and a width of 0.6 µm. The blazed diffraction grating is etched in the outer sidewall of the curved input waveguide, with a maximum modulation depth of 0.3 µm. Previous finite difference time domain (FDTD) simulations determined that over 99% of the optical power is diffracted from the input waveguide along the sidewall grating length of 100 µm. The diffracted light is coupled into the slab waveguide through a 1 µm-wide subwavelength antireflective (AR) grating boundary [7], which comprises a triangular-shaped impedance matching structure with a pitch of 0.3 µm. The receiver waveguide is 1.4 µm wide and is placed at a distance of 70 µm from the diffraction grating at the centre of the arc formed by the curved waveguide. These parameters ensure the matching of the numerical apertures of the receiver waveguide and the diffraction grating, as previously computed with FDTD simulations.

To suppress secondary diffraction peaks, and to obtain a near-field Gaussian profile, apodisation was applied over the first 70 µm of the diffraction grating following a Gaussian apodisation function $y = y_0 \exp(-x^2/2\sigma^2)$, where y_0 is the maximum modulation depth of 0.3 µm. A value of $\sigma = 60$ µm was determined from simulations. Phase errors were corrected by chirping the grating pitch along the waveguide, thus ensuring a constant effective index and phasefront tilt along the grating length. FDTD simulations were performed to determine the grating pitch required to obtain a far-field peak angle of 0° for each modulation depth. This dependency was fitted to a polynomial function, which was applied to the final grating design, resulting in a grating pitch ranging from 560 to 590 nm. Both the intensity and the phase distributions of the near-field profile can be controlled by using apodisation and chirping of the waveguide sidewall grating, thus allowing tailoring the shape of the filter passband. This is an important design advantage compared to AWGs and echelle gratings where altering the near-field intensity profile implies incurring a loss penalty [3].

Fabrication and characterisation: Samples were fabricated on SOI substrates with a 0.26 µm-thick silicon and 2 µm-thick buried oxide layer. A single patterning step by electron beam lithography with high contrast hydrogen silsesquioxane (HSQ) resist was used to define the structure of the device. The resist pattern was transferred into the silicon layer by inductively coupled plasma reactive ion etching (ICP-RIE). An optical micrograph image of the fabricated filter is shown in Fig. 1.

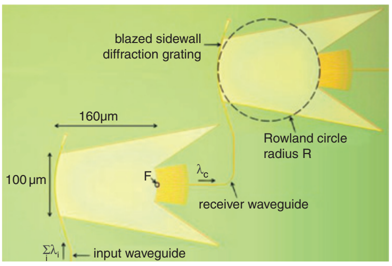

Fig. 1 *Optical micrograph image of fabricated two-stage filter*

Central wavelength λ_c focused in position F of Rowland circle and guided to the input of the second filtering stage

The spectral response of bandpass filters with designed central wavelengths ranging from 1520 to 1590 nm were characterised using a tunable laser with a wavelength range of 1500–1620 nm. Polarisation control optics were used to ensure transverse electric (TE) input polarisation. The device temperature was thermoelectrically stabilised using a Peltier module. A subwavelength grating mode transformer was included at the chip input and output facets for efficient light coupling with a lensed optical fibre.

Results: The normalised transmission spectrum of the fabricated device is shown in Fig. 2, for a device temperature of 23.5 °C. A near-Gaussian profile with no sidelobes is observed. A central wavelength of 1589.6 nm and −3 dB bandwidth of 6.2 nm are obtained. Both sides of the passband are followed by a steep slope with a 4 dB/nm roll-off that reaches a white background noise region with a stopband rejection ranging from −35 to −45 dB for wavelengths separated ≥12.5 nm from the central wavelength. The shape factor, defined as the ratio of the −40 dB bandwidth to the −3 dB bandwidth is 4.03, showing a high skirt selectivity. A 12 dB improvement in the stopband rejection is achieved compared with a single-stage filter of similar design, as well as a 30% reduction in the −3 dB bandwidth. Intrinsic losses of 3.5 dB were measured for each filtering stage at the central wavelength. The temperature dependence of the central wavelength for the measured temperatures, which corresponds to a variation of less than 1.6%. The robustness, small size, and excellent stopband rejection of the device are remarkable advantages compared to other state-of-the-art filters [1–4].

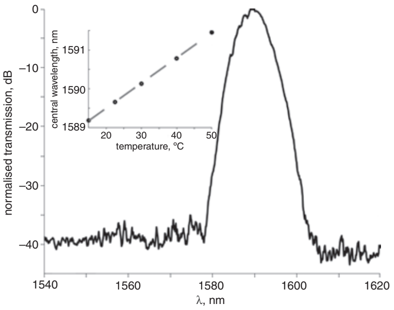

Fig. 2 *Optical micrograph image of fabricated two-stage filter*

Central wavelength λ_c focused in position F of Rowland circle and guided to the input of the second filtering stage

Additional filter designs with central wavelengths shifted down to 1520 nm were measured. A slight deterioration in the performance of the device was observed for shorter central wavelengths, owing to an increase in the losses of the coupling system and the device itself, as well as to limits in the operational range of the subwavelength AR structure. Nonetheless, for each 10 nm shift in central wavelength in the 1520–1590 nm range, the measured intrinsic loss and extinction ratio penalties were below 0.1 dB and 0.55 dB, respectively.

Conclusion: A two-stage bandpass filter with blazed waveguide sidewall gratings has been designed and fabricated, showing a −3 dB bandwidth of 6.2 nm at a central wavelength of 1590 nm and a stopband rejection of 40 dB, as well as a good temperature stability.

5 March 2012
doi: 10.1049/el.2012.0591
One or more of the Figures in this Letter are available in colour online.

A.V. Velasco and M.L. Calvo (*Dpto. de Optica, Facultad de Ciencias Fisicas, Universidad Complutense de Madrid, Madrid 28040, Spain*)

E-mail: avillafr@pdi.ucm.es

P.J. Bock, P. Cheben, J.H. Schmid, J. Lapointe, D.-X. Xu, S. Janz and A. Delâge (*Institute for Microstructural Sciences, National Research Council Canada, Ottawa, Ontario K1A 0R6, Canada*)

References

1 Zhu, L., Huang, Y., and Yariv, A.: ‘Integration of a multimode interference coupler with a corrugated sidewall Bragg grating in planar polymer waveguides’, *IEEE Photonics Technol. Lett.*, 2006, **18**, (6), pp. 740–742

2 Madsen, C.K.: ‘Efficient architectures for exactly realizing optical filters with optimum bandpass designs’, *IEEE Photonics Technol. Lett.*, 1998, **10**, (8), pp. 1136–1138

3 Cheben, P.: ‘Wavelength dispersive planar waveguide devices’ *in* ‘Optical waveguides: from theory to applied technologies’ (CRC Press, 2007), pp. 173–230

4 Mizuno, T., Oguma, M., Kitoh, T., Inoue, Y., and Takahashi, H.: ‘Lattice-form CWDM interleave filter using silica-based planar lightwave circuit’, *IEEE Photonics Technol. Lett.*, 2006, **18**, (15), pp. 1570–1572

5 Hao, Y., Wu, Y., Yang, J., Jiang, X., and Wang, M.: ‘Novel dispersive and focusing device configuration based on curved waveguide grating’, *Opt. Express*, 2006, **14**, (19), pp. 8630–8637

6 Bock, P.J., Cheben, P., Delâge, A., Schmid, J.H., Xu, D.-X., Janz, S., and Hall, T.J.: ‘Demultiplexer with blazed waveguide sidewall grating and sub-wavelength grating structure’, *Opt. Express*, 2008, **16**, (22), pp. 17616–17625

7 Schmid, J.H., Cheben, P., Janz, S., Lapointe, J., Post, E., and Xu, D.-X.: ‘Gradient-index antireflective subwavelength structures for planar waveguide facets’, *Opt. Lett.*, 2007, **32**, (13), pp. 1794–1796

VI

Conclusions

In this thesis, several original photonic devices have been presented, advantageously benefiting from specific strengths of two photonic platforms: holographic photopolymerizable glasses and silicon-on-insulator planar waveguides.

The following advances have been made in the field of holographic photonic devices, and in particular, in sol-gel photopolymerizable glasses:

- The application range of photopolymerizable glasses incorporating High Refractive Index Species (HRIS) was extended to holographic filtering. This was made possible by developing a novel chemical formulation and a synthesis procedure that increases the maximum thickness limit of this photomaterial while maintaining an excellent optical quality. In particular, samples with thicknesses up to 500 µm were prepared for the first time. Additionally, we investigated the dependence on the sample thickness of the fundamental holographic parameters: refractive index modulation, diffraction efficiency, angular selectivity, responsivity, dark diffusion and scattering. The analysis of these parameters confirmed a remarkable holographic performance of the samples with enhanced thickness, including a high optical quality and diffraction efficiencies near 100%.
- A holographic notch filter was implemented in a photopolymerizable glass with enhanced thickness (~500-µm). The increase in the thickness of the holographic medium, in combination with the high spatial resolution of the material, enabled

the recording of a diffraction grating with a spatial frequency of a 2800 lines/mm and a spectral bandwidth of only 0.3 nm. A maximum suppression of -27.5 dB was measured at the operational wavelength, showing a flat response in the passbands with residual ripple under 0.1 dB. Excellent optical quality, low scattering, and negligible absorption losses were also confirmed, opening promising prospects for the use of our photopolymerizable glasses for holographic filtering applications.

- The incorporation of ionic liquid to photopolymerizable glasses was studied for the first time, both in samples with and without HRIS. Although high refractive index modulations were achieved, occasional zirconium precipitation and cluster formation was observed. Ionic liquid was also shown to affect both HRIS and monomer diffusion inside the porous matrix. Additionally, the correlation between the concentration of ionic liquid and the scattering level was demonstrated, a phenomenon which could be used to develop efficient holographic diffusers.

Significant advances have also been made in the development of compact silicon photonic devices. Specifically, the following original silicon planar waveguide devices have been designed, fabricated and characterized:

- An ultra-compact polarization converter implemented for the first time with two asymmetrical subwavelength trenches in a silicon wire waveguide. A polarization mode conversion of 97.5% was measuerd for a converter length of only 10 µm, with insertion loss as low as -0.7 dB. The device was implemented in a single etch step by advantageously using the Reactive Ion Etch lag effect calibration data in the design of the trenches dimensions. This remarkable optical performance opens promising prospects for polarization handling in densely integrated optoelectronic devices. The corresponding scientific paper was recently published (February 2012) but has already received 20 citations in peer literature.

- A wide band integrated demultiplexer based on sidewall blazed gratings. A crosstalk level of 20 - 25 dB was measured in a 300 nm range spanning 21 output channels. The device footprint is only 100 µm × 160 µm, the smallest size yet reported for a device with a similar performance. The diffraction grating was chirped and apodized to optimize coupling to the receiver waveguides and minimize loss, phase errors and crosstalk. A second demultiplexer stage was included at the output of each channel, further reducing the crosstalk levels down to -35 dB, which is the lowest crosstalk yet reported for a microphotonic demultiplexer device.

- A microphotonic bandpass filter based on blazed sidewall gratings. By the curved waveguide sidewall grating configuration and restricting the output to a single silicon wire waveguide, a compact bandpass filters was implemented. In particular, two filtering stages were cascaded for enhanced suppression of the rejection bands. A rejection ratio up to -40 dB was achieved within a footprint of only 300 μm × 500 μm. A FWHM bandwidth of 6.2 nm was measured at a central wavelength of 1590 nm, with a 4 dB/m roll-off at the passband edges. Finally, the dependence of the device performance with temperature was characterized, showing a shift of 65 pm/ºC in the central wavelength of the filter.

- A spatial-heterodyne Fourier-transform spectrometer, comprising an array of Mach-Zehnder interferometers and optical delays implemented with microphotonic waveguide spirals. 32 archimidean spirals with lengths over 1 cm were implemented in a chip with a footprint of 12 mm^2, resulting in a wavelength resolution of 40 pm and a free spectral range of 0.75 nm. The spatial heterodyne configuration allows the simultaneous readout of the spatial interferogram from which the input spectrum is retrieved. This configuration also benefits from an increased *étendue* by allowing a multi-aperture input. Furthermore, an original spectral retrieval algorithm based on the inversion of the calibration matrix was demonstrated. Phase and amplitude errors were corrected for the first time in a waveguide spatial heterodyne spectrometer without active phase-shifting components.

The modifications in the composition and synthesis methods of sol-gel photopolymerizable glasses, and the resulting thickness enhancement, enable the synthesis of holographic notch filters high-performance for the first time in this photomaterial. The developed synthesis procedures and chemical compositions have already resulted in one spanish patent application (P201201084), and could lead to the development of commercially competitive filters. These advances also open the way to additional modification in the synthesis methods of photopolymerizable glasses, in order to potentially achieve even larger material thicknesses.

On the other hand, silicon-on-insulator has the advantage of nano fabrication methods available at commercial PIC foundries, facilitating the implementation of the demonstrated photonic devices to applications such as optical interconnects, biological and environmental analysis, airborne sensing, and spectroscopy. Albeit the performance of demonstrated devices is remarkable, further improvements can be envisioned. Advanced fabrication techniques, such as proximity error correction can be used to increase the extinction ratio of the polarization mode converter, by accurately controlling the trench dimensions. The short length of this polarization mode converter also lends to its integration in more complex polarization handling devices with active tuning, with extinction ratios exceeding 40 dB [Alonso-Ramos'12].

The performance of the curved sidewall grating filters and demultiplexers could also be further improved. New loss-reduction techniques for these devices are currently being explored at the NRC Canada. A low-loss demultiplexer device would enable the development of filters with several cascaded stages for crosstalks below -30 dB, which remains a significant challenge in silicon photonics planar waveguide devices.

Finally, spectral resolution of the Spatial Heterodyne Fourier-Transform (SHFT) spectrometer configuration could be further increased by incorporating ultra low-loss waveguides, which would enable to implement longer optical delays while still maintaining high interferometric fringe contrast. To this regard, integrated monolithic spiral waveguides with losses as low as 0.08 dB/m and an optical length of up to 39 meters have already been demonstrated [Lee'12], which for the proposed SHFT spectrometer concept corresponds to an unprecedented resolution of 5×10^{-5} cm^{-1} for a spectrometer chip.

In a broader perspective, regarding the future of the two photonic platforms used in the works of the present thesis, it is apparent that they are following diverging paths in terms of potential industrialisation and applications. Silicon photonics, due to the maturity and low cost of CMOS fabrication process and excellent integration potential, is becoming established as a leading integrated optics for mass-scale. Holographic photomaterials fabrication processes, and in particular those of photopolymerizable glasses, are less likely to be exploited in mass-scale microfabrication technologies and therefore widespread application. Nevertheless, their unmatched holographic performance and freedom of design make them ideal candidates for highly specialised niche applications, such as narrowband and beam-shaping elements.

Annex A

Methods

In this annex, the experimental methods used in the present work for the design, fabrication and characterization of the developed photonic devices are detailed.

A.1. Synthesis of photopolymerizable glasses
A.2. Photopolymerizable glass recording and characterization setup
A.3. Computational methods and design of integrated SOI devices
A.4. Fabrication of SOI devices
A.5. Characterization of SOI devices

A.1. Synthesis of photopolymerizable glasses

A.1.1. Samples of thickness under 200 µm

Photopolymerizable glasses were synthesized by gelation of a silica sol prepared by acid hydrolysis of glycidoxypropyltrimethoxysilane (GPTMS, IUPAC name trimethoxy-[3-(oxiran-2-ylmethoxy)propyl]silane; 11.8 mmol, from Aldrich) and tetraethylorthosilicate (TEOS; 1.8 mmol, from Aldrich). The hydrolysis was triggered by a solution of hydrochloric acid in water (21.3 mmol H_2O/HCl) at pH 2. This specific molar ratio between GPTMS and TEOS ensures minimal shrinkage of the glass matrix under actinic light exposure [Ramos'04] and complete water consumption before the addition of zirconium isopropoxide.

The photoinitiator, IRGACURE-784 (bis(.eta.5-2,4-cyclopentadien-1-yl)bis[2, 6-difluoro-3-(1H-pyrrol-1-yl)phenyl]titanium, 0.1 mmol, from Ciba-Geigy), was incorporated in a solution of phenoxyethyl acrylate (POEA, 3.1 mmol, from Aldrich). The high refractive index species (HRIS) was added to the mixture as a solution of zirconium isopropoxide isopropanol complex ($Zr(O^iPr)_4 \cdot {}^iPrOH$; 1.5 mmol, from Aldrich) chelated with methacrylic acid (MA; 7 mmol, from Aldrich).

The solution was vigorously and continuously stirred, and then filtered with a 0.2 µm Millipore filter and pipete casted on cleaned glass microscope slides. Samples with thicknesses from 20 µm up to 200 µm were prepared by callibrating the amount of sol casted on the slides. Gelation and curing was performed in a temperature-controlled environment at 40 ºC, with glass gelation times ranging from 12 hours to several days depending on the sample thickness.

For the synthesis of the photopolymerizable glass incorporating ionic liquid (IL) presented in section 4.2, 1-butyl-3-methylimidazolium tetrafluorborate (from Aldrich) was added to the sol prior to gelation, with other steps kept identical. In photopolymerizable glass samples without HRIS, two particular concentrations of IL were selected, namely, 4% and 6% of the total mass. In photopolymerizable glass samples incorporating both HRIS and IL weights, the concentrations were 9.5% (HRIS) and 3.2% (IL) of the total mass.

A.1.2. Samples of thickness above 200 µm

In order to overcome the maximum thickness limitations of the nominal sample preparation procedure (A.1.1), several modifications were made. First, the amount of zirconium isopropoxide and methacrylic acid in the samples was reduced to one half compared to the nominal formulation. Second, the silica sol was casted on glass Petri dishes instead of microscope slides, allowing the deposition of a greater amount of material. The flatness of the glass surface in the area of holographic exposure was ensured by microscopy measurements, to minimize distortion of optical beams. Samples were sealed with wax paper to prevent air flow in early gelation stages. After 24 hours, small holes were progressively made in the wax paper seal to progressively increase air circulation. A controlled environment with a temperature of 40ºC and a relative humidity of 25% was maintained, with a total gelation time of 14 days for the thickest samples (500 µm).

The holographic recording was performed with two collimated actinic beams, after which samples were exposed to natural light to consume the remaining photosensitizer species. A refractive index compensator liquid (Norland Index Matching Liquid 150, $n = 1.52$) was casted on the surface of the photopolymerizable glasses to minimize scattering effects of surface corrugations generated during the matrix formation. Finally, samples were sealed for protections with a thin glass cover.

A.2. Photopolymerizable glass recording and characterization setup

Holographic photonic devices were recorded by interference of two mutually coherent *s*-polarized actinic light beams using a setup shown in figure A.1. The beams were generated by a single diode-pumped solid-state laser, specifically a doubled neodymium-doped yttrium aluminum garnet (Nd:YAG) laser with a central wavelength of 532 nm and a nominal power of 50 mW (Oxxius 532 S). The laser output beam was spatially filtered and collimated by using a microscope objective, a pinhole and a collimating achromatic lens. Polarization optics was included to ensure *s*-polarization for maximal interference fringe visibility. The resulting beam was equally divided by a beamsplitter, and each beam was redirected with a mirror towards the photomaterial sample.

The grating period of the recorded volume phase diffraction holographic gratings (VPHG) is determined by the angle of incidence of the recording beams θ:

$$\Lambda = \frac{\lambda}{2\sin(\theta)} \tag{A.1}$$

where Λ is the grating period and λ is the wavelength of the incident recording beams. Diffraction gratings with spatial frequencies ranging from 500 lines/mm up to 2600 lines/mm were recorded using this setup.

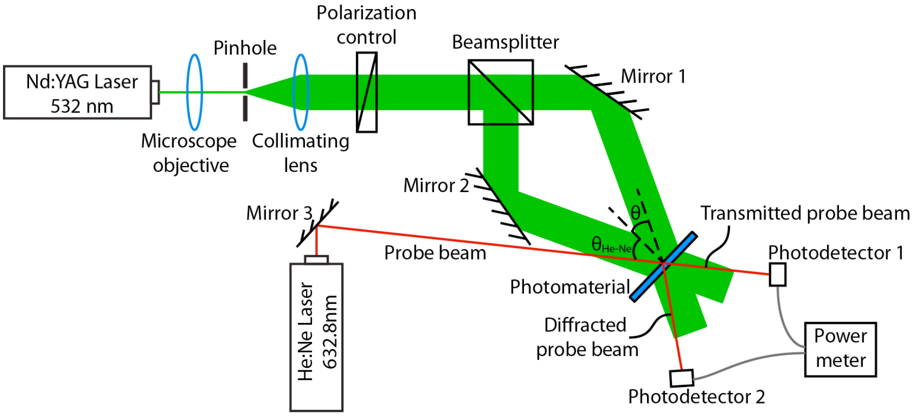

Figure A.1. *Schematic of the experimental setup for grating recording and real-time monitoring of holographic diffraction gratings. Gratings are recorded by two mutually coherent s-polarized light beams with equal power generated by a frequency-doubled Nd:YAG laser at the same solid-state laser source in a Mach-Zehnder configuration. The grating formation is monitored in real-time by measuring the diffracted and transmitted beams from a He-Ne laser.*

The grating formation was monitored in real time by a non-actinic probe beam generated by a He-Ne laser of wavelength $\lambda_{He\text{-}Ne}$ = 632.8 nm and a power of 0.5 mW (Newport ULM-TILT). The incidence angle of the laser probe $\theta_{He\text{-}Ne}$ was chosen as the Bragg's angle θ_B:

$$\sin(\theta_B) = \frac{\lambda_{He-Ne}}{2\Lambda} \tag{A.2}$$

The optical powers of the diffracted and transmitted beams were measured by two photodetectors. Photopolymerizable glass samples were mounted on a high-precision rotation platform for angularly-resolved measurements of the diffraction efficiency of the recorded gratings (angular selectivity curve). The optical quality of the samples was characterized by measuring the beam profiles of the transmitted and diffracted beams with a Spiricon digital camera (Ophir), with a pixel size of 4.4 µm × 4.4 µm.

A.3. Computational methods and design of integrated SOI devices

Silicon photonic devices were designed using various numerical simulation software tools. Both modal analysis and waveguide propagation simulations were used to optimize the design parameters of the devices. Convergence studies to determine the appropriate simulation time, layout area and meshing were performed prior to the modal and propagation analysis.

The software and computational methods used in the present thesis are briefly discussed in this section. An example of photonic design based on modal and propagation simulations is shown in figure A.2. In particular, some illustrating simulation results from the design of the polarization converter (section 5.2) are presented.

A.3.1. Waveguide propagation

A.3.1.1. Fimmprop (Photon Design, Ltd.)

Fimmprop implements an eigenmode expansion method (EME) [Gallagher'03] to numerically solve Maxwell's equations by defining the electromagnetic fields in terms of a basic set of local modes. In theory, when the number of local modes tends to infinity, the exact solution is obtained. In a practical implementation, the maximum number of modes is indeed limited, and determine a trade-off between numerical accuracy and computational load. The scattering matrix (S-matrix) technique is used for concatenation of waveguides sections and modeling of structures that vary along light propagation direction. The scattering matrix relates optical fields entering and leaving the waveguide sections at both ends, including reflections.

A.3.1.2. FDTD Solutions (Lumerical solutions, Inc.)

This software implements a Finite Difference Time Domain technique [Yee'66, Taflove'05], based on the discretization of time-dependent Maxwell's equations over a simulation grid which samples the dielectric permitivity and magnetic permeability of an arbitrary photonic structure. The precision of the method can be increased by reducing the grid size, at the expense of an increased computational load. By computing the temporal evolution of the propagating waves, the response of the system over a wide range of frequencies is obtained in a single simulation. Modal properties can be deduced by Fourier-transformation of the time-varying response of the system, with peaks in the transformed spectrum corresponding to eigenfrequencies. FDTD systems are typically limited by a heavy computational load, specially in three-dimensional simulations. Over 10 cells are typically required to accurately represent the field within the length of the minimum wavelength under analysis. A finer grid may be required for increased accuracy and to avoid the accumulation of numerical errors which increase proportionally to the propagation length.

A.3.2. Mode solvers

A.3.2.1. Fimmwave (Photon Design, Ltd)

Fimmwave is a fully vectorial photonic mode solver based on a mode matching method [Nguyen'01]. The optimization problem is defined by modeling an arbitrary waveguide as a set of vertical slices (figure A.2.b). Each vertical slice is uniform in the lateral direction, but is composed of a plurality of layers with different refractive indexes, including structures with complex refractive indexes such as metallic components or waveguides with gain. Once the waveguide has been defined in the described manner, the underlying algorithms compute the optical modes of each slice and search for the solution that optimizes the boundary matching conditions between adjacent slides. As a result of this approach, Fimmwave is particularly optimized for waveguide structures with rectangular boundaries.

A.3.2.2. MODE Solutions (Lumerical Solutions, Inc.)

MODE solutions provides fully vectorial finite-difference analysis [Xu'94], based on the discretization of any arbitrary waveguide geometry into a grid of refractive index values (figure A.2.c). As in the case of the FDTD waveguide propagation algorithms, precision is increased with the grid resolution, at the cost of a greater computational complexity. The software implements an efficient eigenvalue search algorithm, and supports any refractive index definition, such as dielectric, lossy, conductive Lorentz, Drude, Debye, Sellmeier, and anisotropic materials; as well as spatially-varying refractive index distributions. Modal analysis in frequency domain for both guided and leaky modes is included.

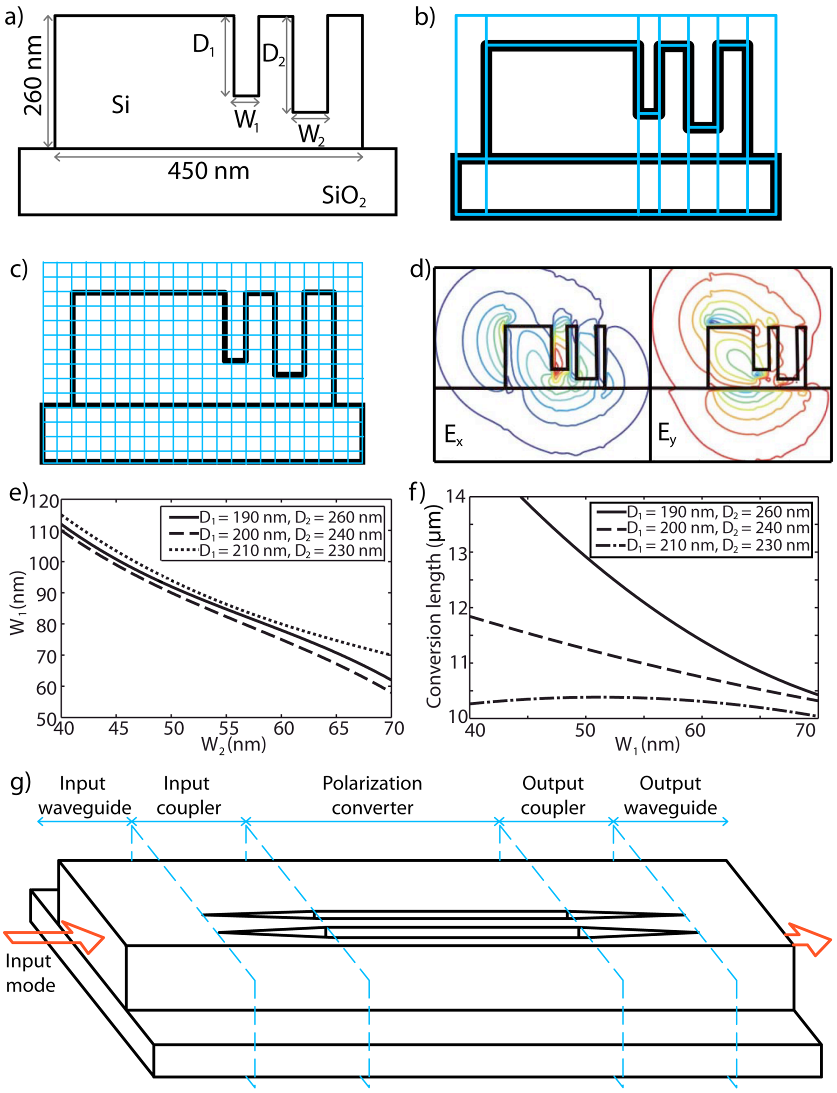

Figure A.2. *Example of polarization rotator photonic design based on numerical simulations.* ***a)*** *Structure of a polarization rotator waveguide with two asymmetrical subwavelength trenches with widths W_1 and W_2, and depths D_1 and D_2. The goal of the simulation is to determine the optimal trench dimensions to achieve hybrid modes with a minimal conversion length and maximum polarization conversion efficiency.* ***b)*** *Modeling of the polarization converter with the Fimmwave mode solver.* ***c)*** *Meshing of the Finite Difference Time Domain mode solver.* ***d)*** *Electric field components E_x and E_y of one of the hybrid modes of the polarization rotator structure.* ***e)*** *Combinations of design parameters yielding hybrid modes.* ***f)*** *Theoretical conversion lengths for the sets of parameters defined in (e).* ***g)*** *Schematic of the three-dimensional layout of the complete polarization rotator structure. The design is refined considering losses and polarization rotation effects in the coupling sections.*

A.4. Fabrication of SOI devices

The silicon photonic devices presented in this thesis were fabricated in SOI substrates with a 260-nm-thick silicon on a 2-µm-thick buried oxide layer. The waveguide structures were defined in high contrast hydrogen silsesquioxane (HSQ) resist by electron beam lithography. Inductively coupled plasma reactive ion etching (ICP-RIE) was used to transfer the resist pattern into the silicon layer. A 2 µm thick SU-8 polymer ($n_{\text{SU-8}} \sim 1.52$ at $\lambda = 1.5$ nm) layer was used as upper cladding. Samples were cleaved into separate chips and their facets were polished.

All the devices were designed for a single patterning and etching step, thereby obviating the need of complex alignment fabrication steps. As discussed in section 5.2, the fabrication of the polarization rotator requires etching trenches with different depths. This is achieved by using the RIE-lag effect, which manifests itself as a partial etch of the silicon layer for features sizes below a given threshold, while structures above the threshold are fully etched. Although this effect is usually considered as detrimental when fabricating microphotonic devices, here we advantageously use it to implement different etch depths a single etching step. This effect depends on the particular foundry in which the photonic circuits are fabricated, and it needs to be calibrated (fig A.3) before it can be used in the design flow.

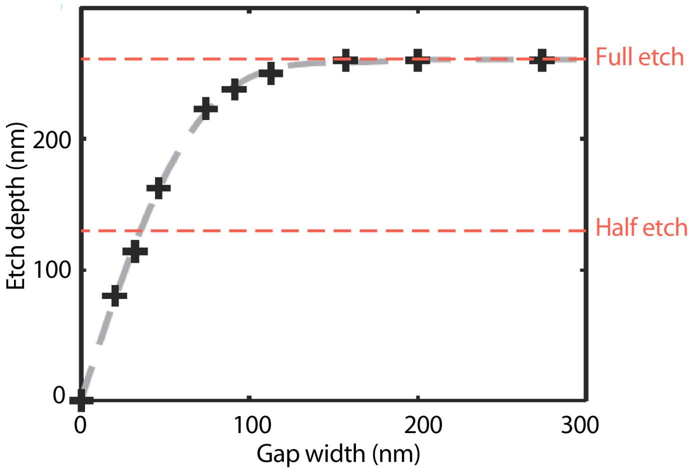

Figure A.3. *Calibration measurement of etch depth as a function of gap width of the lag effect in a reactive ion etch process. The experimental depth-width relation (grey curve) is subsequently used in the design of a photonic structure with varying etch depths in a single etch step process.*

A.5. Characterization of SOI devices

The fabricated devices were characterized with high-resolution tunable semiconductor lasers. Polarization control optics was used to select either TE or TM input polarization and a lensed polarization maintaining fiber was used to couple light in the input waveguide. A Peltier stage was used for thermal stabilization. Output light was collected by a microscope objective and focused onto an InGaAs photodetector. For the characterization of the spatial heterodyne Fourier-transform Spectrometer, the photodetector was replaced by a a high-sensitivity infrared photodetector array camera in order to capture all the outputs of the device in a single measurement. Various test structures were included on the chip to accurately characterize the coupling and propagation losses and separate them from other effects in the photonic device response.

Fiber coupling at the input facet of the chips was optimized with efficient subwavelength grating (SWG) edge couplers [Cheben'10]. The couplers were integrated on the chip to minimize Fabry-Perot at the facets. The SWG coupler is designed to adiabatically transform the waveguide mode to match the optical fiber at one end of the coupler and the Si-wire waveguide on the other end. Coupling losses of -0.9 dB for TE polarization and -1.2 dB for TM polarization have been demonstrated. A detailed description of the specific coupler structure used in the presented photonic devices can be found in [Cheben'10].

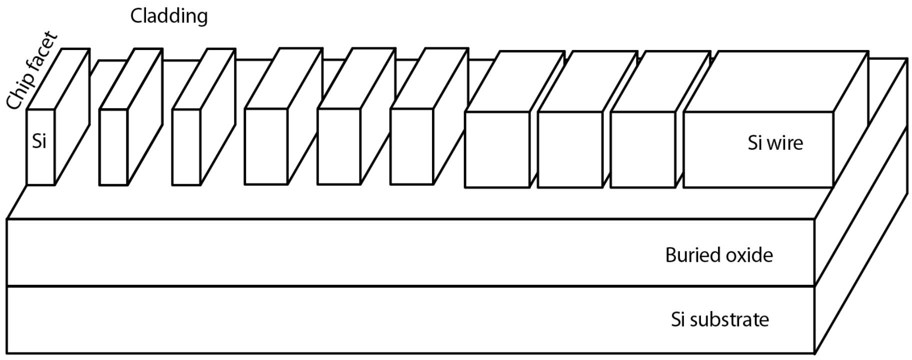

Figure A.4. *Schematic of a subwavelength grating fiber-to-chip coupler. The fill ratio of silicon is progressively increased towards Si-wire waveguide to gradually increase the mode confinement.*

References

[Abbott'04] A. P. Abbot, D. Boothby, G. Capper, D. L. Davies and R. K. Rasheed, "Deep eutectic solvents formed between choline chloride and carboxylic acids: versatile alternatives to ionic liquids," *J. Am. Chem. Soc.* **126**, 9142 (2004).

[Albert'11a] S. Albert, K. K. Albert and M. Quack, *Handbook of high-resolution spectroscopy* (Wiley, Chichester, 2011).

[Albert'11b] S. Albert, K. K. Albert, P. Lerch and M. Quack, "Synchrotron-based highest resolution Fourier transform infrared spectroscopy of naphthalene ($C_{10}H_8$) and indole (C_8H_7N) and its application to astrophysical problems," *Faraday Discuss.* **150**, 71 (2011).

[Alduino'07] A. Alduino and M. Paniccia, "Interconnects: wiring electronics with light," *Nat. Photonics* **1**, 153 (2007).

[Alonso-Ramos'12] C. Alonso-Ramos, R. Halir, A. Ortega-Moñux, P. Cheben, L. Vivien, Í. Molina-Fernández, D. Marris-Morini, S. Janz, D.-X. Xu, and J. Schmid, "Highly tolerant tunable waveguide polarization rotator scheme," *Opt. Lett.* **37**, 3534 (2012).

[Barbastathis'99] G. Barbastathis, M.Balberg, and D. J. Brady, "Confocal microscopy with a volume holographic filter," *Opt. Lett.* **24**, 811 (1999).

[Batterman'64]	B. W. Batterman and H. Cole, "Dynamical diffraction of X Rays by perfect crystals," *Rev. Mod. Phys.* **36**, 681 (1964).
[Becker'72]	E. D. Becker and T. C. Farrar, "Fourier transform spectroscopy," *Science* **178**, 361(1972).
[Berg'96]	R. Berg, S. Hvilsted and P. S. Ramanujan, "Peptide oligomers for holographic data storage," *Nature* **383**, 505 (1996).
[Blanche'10]	P. A. Blanche, A. Bablumian, R. Voorakaranam, C. Christenson, W. Lin, T. Gu, D. Flores, P. Wang, W.-Y. Hsieh, M. Kathaperumal, B. Rachwal, O. Siddiqui, J. Thomas, R. A. Norwood, M. Yamamoto and N. Peyghambarian, "Holographic three-dimensional telepresence using large-area photorefractive polymer," *Nature* **468**, 80 (2010).
[Bland'12]	J. Bland-Hawthorn and P. Kern, "Molding the flow of light: Photonics in astronomy," *Phys. Today* **65**, 31 (2012).
[Bidnyk'06]	S. Bidnyk, D. Feng, A. Balakrishnan, M. Pearson, M. Gao, H. Liang, W. Qian, C.-C. Kung, J. Fong, J. Yin, and M. Asghari, "Silicon-on-insulator-based planar circuit for passive optical network applications," *IEEE Photon. Technol. Lett.* **18**, 2392 (2006).
[Bjelkhagen'95]	H. I. Bjelkhagen, *Silver-halide recording materials for holography and their processing* (Springer, 1995)
[Bock'08]	P. J. Bock, P. Cheben, A. Delâge, J. H. Schmid, D.-X. Xu, S. Janz and T. J. Hall, "Demultiplexer with blazed waveguide sidewallgrating and sub-wavelength grating structure," *Opt. Express* **16**, 17616 (2008).
[Brady'92]	D.Brady, A. Chen, and G. Rodriguez, "Volume holographic pulse shaping," *Opt. Lett.* **17**, 610 (1992).
[Brooks'06]	C. Brooks, P. E. Jessop, H. Deng, D. O. Yevick, and G. Tarr, "Passive silicon-on-insulator polarization rotating waveguides," *Opt. Eng.* 45, 044603 (2006).
[Brouckaert'07a]	J. Brouckaert, G. Roelkens, D. Van Thourout and R. Baets, "Compact InAlAs–InGaAs Metal– Semiconductor– Metal Photodetectors Integrated on Silicon-on-Insulator Waveguides," *Phot. Tech. Lett.* **19**, 1484 (2007).
[Brouckaert'07b]	J. Brouckaert, W. Bogaerts, P. Dumon, D. Thourhout, and R. Baets, "Planar concave grating demultiplexer fabricated on a nanophotonic silicon-on-insulator platform," *J. Lightwave Technol.* **25**, 1269 (2007).

[Calvo’06]	M. L. Calvo, P. Cheben, Ó. Martínez-Matos, F. del Monte, and J. A. Rodrigo, “Experimental Detection of the Optical Pendellösung Effect,” *Phys. Rev. Lett.* **97**, 084801 (2006).
[Calvo’08]	M. L. Calvo and P. Cheben, “Fundamentals and advances in holographic materials for optical data storage” in *Advances in Information Optics and Photonics* (eds. Ari T. Friberg and R. Dändliker) (SPIE Press, Bellingham, USA, 2008).
[Calvo’09]	M. L. Calvo and P. Cheben, "Photopolymerizable sol–gel nanocomposites for holographic recording,” *J. Opt. A: Pure Appl. Opt.* **11**, 024009 (2009).
[Campenhout’08]	J. Van Campenhout, L. Liu, P. R. Romeo, D. Van Thourout, N. Y. Yorktown, P. Regreny, L. Di Cioccio, J. M. Fedeli and R. Baets, “A Compact SOI-Integrated Multiwavelength Laser Source Based on Cascaded InP Microdisks” *Phot. Tech. Lett.* **20**, 1345 (2008).
[Cao’09]	L. Cao and C. Gu, “Matched spectral filter based on reflection holograms for analyte identification,” *Appl. Opt.* **48**, 6973 (2009).
[Carmichael’00]	J. Carmichael, D. M. Haddleton, S. A. F. Bon, and K. R. Seddon, "Copper Mediated Living Radical Polymerisation in an Ionic Liquid,” *Chem. Commun.* **14**, 1237 (2000).
[Carrabba’90]	M. M. Carrabba, K. M. Spencer, C. Rich and D. Rauh, “The utilization of a holographic Bragg diffraction filter for Rayleight line rejection in Raman spectroscopy,” *Appl. Spectrosc.* **44**, 1558 (1990).
[Carretero’04]	L. Carretero, A. Murciano, S. Blaya, M. Ulibarrena and A. Fimia, “Acrylamide-N,N'-methylenebisacrylamide silica glass holographic recording material,” *Opt. Express* **12**, 1780 (2004).
[Cartledge’94]	J. C. Cartledge, C. Rolland, S. Lemerle and A. Solheim, “Theoretical performance of 10 Gb/s lightwave systems using a III-V semiconductor Mach-Zehnder modulator,” *Phot. Tech. Lett.* **6**, 282 (1994).
[Caulfield’79]	H. J. Caulfield, *Handbook of optical holography* (Academic Press, New York, 1979).
[Cheben’96]	P. Cheben, T. Belenguer, A. Nuñez, F. del Monte and D. Levy, “Holographic diffraction gratings recording in organically modified silica gels,” *Opt. Lett.* **22**, 1857 (1996).
[Cheben’01]	P. Cheben and M.L. Calvo, “A photopolymerizable glass with diffraction efficiency near 100% for holographic storage,” *Appl. Phys. Lett.* **78**, 1490 (2001).

[Cheben’03] P. Cheben, D. X. Xu, S. Janz and A. Delâge, “Scaling down photonic waveguide devices on the SOI platform,” *Proc. SPIE* **5117**, 147 (2003).

[Cheben’05] P. Cheben, I. Powell, S. Janz, and D.-X. Xu, “Wavelength-dispersive device based on a Fourier-transform Michelson-type arrayed waveguide grating,” *Opt. Lett.* **30**, 1824 (2005).

[Cheben’06] P. Cheben, D.-X. Xu, S. Janz, and A. Densmore, “Subwavelength waveguide grating for mode conversion and light coupling in integrated optics,” *Opt. Express* **14**, 4695 (2006).

[Cheben‘07a] P. Cheben, J. H. Schmid, A. Delâge, A. Densmore, S. Janz, B. Lamontagne, J. Lapointe, E. Post, P. Waldron, and D.-X. Xu, “A high-resolution silicon-on-insulator arrayed waveguide grating microspectrometer with submicrometer aperture waveguides,” *Opt. Express* **15**, 2299 (2007).

[Cheben‘07b] P. Cheben, "Wavelength dispersive planar waveguide devices: Echelle gratings and arrayed waveguide gratings,” in *Optical Waveguides: From Theory to Applied Technologies* (eds. M. L. Calvo and V. Lakshminaryanan) (CRC Press, London, 2007).

[Cheben’10] P. Cheben, P. J. Bock, J. H. Schmid, J. Lapointe, S. Janz, D.-X. Xu, A. Densmore, A. Delâge, B. Lamontagne, and T. J. Hall, “Refractive index engineering with subwavelength gratings for efficient microphotonic couplers and planar waveguide multiplexers” *Opt. Lett.* **35**, 2526 (2010).

[Chen’09] L. Chen and M. Lipson, “Ultra-low capacitance and high speed germanium photodetectors on silicon,” *Opt. Express* **17**, 7901 (2009).

[Cody’12] D. Cody, I. Naydenova and E. Mihaylova, “New non-toxic holographic photopolymer material,” *J. Opt.* **14**, 015601 (2012).

[Cohen’95] L. Cohen, *Time-Frequency Analysis* (Prentice-Hall, New York, 1995)

[Colburn’71] W. S. Colburn and K. A. Haines, “Volume Hologram Formation in Photopolymer Materials,” *Appl. Opt.* **10**, 1636 (1971).

[Collier’71] R. J. Collier, C. B. Burckhardt, and L. H. Lin, “Optical holography” (Academic Press, New York, 1971).

[Colthup’90] N. B. Colthup, L. H. Daly and S. E. Wiberley, *Introduction to infrared and Raman spectroscopy* (Lavoisier, Paris, 1990).

[Colvin’00] V. L. Colvin, A. L. Harris, H. E. Katz, and M. L. Schilling, “Holographic recording,” US 6,165,648 A1 (2000).

[Coufal'00] H. J. Coufal, D. Psaltis and G.T. Sincerbox, *Holographic Data Storage* (Springer-Verlag, New York, 2000).

[Curtis'94] K. Curtis and D. Psaltis, "Characterization of the DuPont photopolymer for three-dimensional holographic storage," *App. Opt.* **33**, 5396 (1994).

[Dai'05] D. Dai and S. He, "Analysis of the birefringence of a silicon-on-insulator rib waveguide," *App. Opt.* **43**, 1156 (2005).

[Dai'11] D. Dai and J. E. Bowers, "Novel concept for ultracompact polarization splitter-rotator based silicon nanowires," *Opt. Express* **19**, 10940 (2011).

[Dehlinger'04] G. Dehlinger, S. J. Koester, J. D. Schaub, J. O. Chu, Q. C. Ouyang and A. Grill, "High-speed Germanium-on-SOI lateral PIN photodiodes," *Phot. Tech. Lett.* **16**, 2547 (2004).

[DelMonte'06] F. Del Monte, Ó. Martínez-Matos, J. A. Rodrigo, M.L. Calvo and P. Cheben, "A volume holographic sol-gel material with large enhancement of dynamic range by incorporating high refractive index species," *Adv. Mater.* **18**, 2014 (2006).

[Densmore'06] A. Densmore, D.-X. Xu, P. Waldron, S. Janz, P. Cheben, J. Lapointe, A. Delâge, B. Lamontagne, J. H. Schmid, and E. Post, "A silicon-on-insulator photonic wire based evanescent field sensor," *IEEE Phot. Technol. Lett.* **18**, 2520 (2006).

[Densmore'07] A. Densmore, D.-X. Xu, P. Waldron, S. Janz, P. Cheben, A. Delâge, P. Cheben and J. Lapointe, "Thin silicon waveguides for biological and chemical sensing," *Proc SPIE.* **6477**, 18 (2007).

[Dickey'03] Fred M. Dickey, "Laser beam shaping," *Opt. Photonics News* **14**, 30 (2003).

[DeOliveira'12] N. De Oliveira, "High-resolution broad-bandwidth Fourier-transform absorption spectroscopy in the VUV range down to 40 nm". *Nat. Photonics* **5**, 149 (2011).

[Domínguez'11] P. Domínguez-García, M.A. Rubio, A. V. Velasco, M.P. Hernández-Garay, M.L. Calvo and P. Cheben, "Single-particle micro-rheology of photopolymerizable sol-gel materials for optical applications," presented at *Colloids and materials*, Amsterdam (Holland), May 2011.

[Dumon'06] P. Dumon, W. Bogaerts, D. Van Thourhout, D. Taillaert, R. Baets, J. Wouters, S. Beckx, and P. Jaenen, "Compact wavelength router based on a Silicon-on-insulator arrayed waveguide grating pigtailed to a fiber array," *Opt. Express* **14**, 664 (2006).

[Doerr'06] C. R. Doerr and K. Okamoto, "Advances in silica planar lightwave circuits," *J. Lightwave Technol.* **24**, 4763 (2006).

[Ebelemen'55] J. J. Ebelemen and L. A. Salvetat, *Recueil des travaux scientifiques* (1885).

[Extermann'36] R. Extermann and G. Wannier, *Helv. Phys. Acta* **9**, 520 (1936).

[Fang'10] Q. Fang, T.-Y. Liow, J. F. Song, K. W. Ang, Y. T. Phang, M. B. Yu, G. Qiang and D. L. Kwong, "Monolithic Silicon Photonic DWDM Receiver for Terabit Data Communications," presented at *Optical Fiber Communication Conference*, San Diego (USA), March 2010.

[Feng'09] D. Feng, S. Liao, P. Dong, N-N. Feng, H. Liang, D. W. Zheng, C.-C. C. Kung, J. Fong, R. Shafiiha, J. E. Cunningham, A. V. Krishnamoorthy, V. Ashok and M. Asghari, "High-speed Ge photodetector monolithically integrated with large cross-section silicon-on-insulator waveguide," *App. Phys. Lett.* **95**, 261105 (2009).

[Feng'11] D. Feng, N.-N. Feng, C.-C. Kung, H. Liang, W. Qian, J. Fong, B. J. Luff, and M. Asghari, "Compact single-chip VMUX/DEMUX on the silicon-on-insulator platform," *Opt. Express* **19**, 6125 (2011).

[Filler'64] A. S. Filler, "Apodization and Interpolation in Fourier-Transform Spectroscopy," *J. Opt. Soc. Am.* **54**, 762 (1964).

[Fleisher'81] M. Fleisher, U. Mahlab and J. Shamir, "Entropy optimized filter for pattern recognition," *Appl. Opt.* **29**, 2091 (1990).

[Florjańczyk'07] M. Florjańczyk, P. Cheben, S. Janz, A. Scott, B. Solheim, and D. X. Xu, "Multiaperture planar waveguide spectrometer formed by arrayed Mach-Zehnder interferometers," *Opt. Express* **15**, 18176 (2007).

[Florjańczyk'12] M. Florjańczyk, C. Alonso-Ramos, P. Bock, A. Bogdanov, P. Cheben, I. Molina-Fernández, S. Janz, B. Lamontagne, A. Ortega-Moñux, and A. Scott, "Development of Fourier-transform waveguide spectrometer for space applications," *Opt. Quant. Electron.* **44,** 549 (2012).

[Foster'06] M. A. Foster, A. C. Turner, J. E. Sharping, B. S. Schmidt, M. Lipson, and A. L. Gaeta, "Broadband optical parametric gain on a silicon photonic chip," *Nature* **441**, 960 (2006).

[Fujii'80] H. Fujii, S. P. Almeida and J. E. Dowling, "Rotational matched spatial filter for biological pattern recognition," *Appl. Opt.* **19**, 1190 (1980).

[Fukada'06] H. Fukada, K. Yamada, T. Tsuchizawa, T. Watanabe, H. Shinojima and S. Itabashi, "Ultrasmall polarization splitter based on silicon wire waveguides," *Opt. Express* **14**, 12401 (2006).

[Fukada'08] H. Fukada, K. Yamada, T. Tsuchizawa, T. Watanabe, H. Shinojima and S. Itabashi, "Silicon photonic circuit with polarization diversity," *Opt. Express* **16**, 4872 (2008).

[Gabor'48] D. Gabor, "A new microsopic principle," *Nature* **161**, 777 (1948).

[Gallagher'03] D. F.G. Gallagher and T. P. Felici, "Eigenmode Expansion Methods for Simulation of Optical Propagation in Photonics - Pros and Cons," *Proceedings of SPIE* **4987**, 69 (2003).

[Gaylord'81] T. K. Gaylord and M. G. Moharam, "Thin and thick gratings: terminology clarification," *App. Optics* **20**, 3271 (1981).

[Golub'70] G. H. Golub and C. Reinsch, "Singular value decomposition and least squares solutions," *Numerische Mathematik* **14**, 403 (1970).

[Green'01] M. A. Green, J. Zhao, A. Wang, P. J. Reece and M. Gal, "Efficient silicon light-emitting diodes," *Nature* **412**, 805 (2001).

[Griffiths'07] P. R. Griffiths, J. A. de Haseth, *Fourier transform infrared spectrometry* (Wiley, New York, 2007).

[Halir'10] R. Halir, P. Cheben, J. H. Schmid, R. Ma, D. Bedard, S. Janz, D.-X. Xu, A. Densmore, J. Lapointe, and I. Molina-Fernández, "Continuously apodized fiber-to-chip surface grating coupler with refractive index engineered subwavelength structure," *Opt. Lett.* **35**, 3243 (2010).

[Han-Yong'08] N. Han-Yong, R. W. Michael, L. Daqun, W. Xuan, M. Jose, R. P. Roberto, and P. Kachesh, "4 x 4 wavelength reconfigurable photonic switch based on thermally tuned silicon microring resonators," *Opt. Eng.* **47**, 0446011 (2008).

[Hao'06] Y. Hao, Y. Wu, J. Yang, X. Jiang, and M. Wang, "Novel dispersive and focusing device configuration based on curved waveguide grating," *Opt. Express* **14,** 8639 **(**2006).

[Hariharan'87] P. Hariharan and S. A. Benton, *Optical holography: principles, techniques and applications* (Media Laboratory, Cambridge, 1987).

[Harlander'92] J. M. Harlander, R. J. Reynolds and F. L. Roesler, "Spatial heterodyne spectroscopy for the exploration of diffuse intersetellar emission lines at far ultraviolet wavelengths," *Astroph. J.* **396**, 730 (1992).

[Harlander'02]	J. M. Harlander, F. L. Roesler, J. G. Cardon, C. R. Englert, and R. R. Conway, "A spatial heterodyne spectrometer for remote sensing of earth middle atmosphere," *Appl. Opt.* **41**, 1343 (2002).
[Harlander'04]	J. M. Harlander, F. L. Roesler, C. R. Englert, J. G. Cardon, and J. Wimperis, "Spatial heterodyne spectroscopy for high spectral resolution space-based remote sensing," *Opt. Photonics News* **15**, 46 (2004).
[Harrisson'02]	S. Harrisson, S. R. Mackenzie, and D. M. Haddleton, "Application of ionic liquids as solvents for polymerization processes," *Chem. Commun.* **23**, 2850 (2002).
[Hernández'11]	M. P. Hernández-Garay, O. Martínez-Matos, J. G. Izquierdo, M. L. Calvo, P. Vaveliuk, P. Cheben, and L. Bañares, "Femtosecond spectral pulse shaping with holographic gratings recorded in photopolymerizable glasses," *Opt. Express* **19**, 1516 (2011).
[Haw'03]	M. D. Haw, M. Gillie and W. C. K. Poon, 'Effects of phase behaviour on drying of a Holographic data storage: The light fantastic," *Nature* **422**, 556 (2003).
[Hill'93]	K. B. Hill and D. J. Brady, "Pulse shaping in volume reflection holograms," *Opt. Lett.* **18**, 1739 (1993).
[Holmes'06]	B. M. Holmes and D. C. Hutchings, "Realization of a novel low-loss monolithically integrated passive waveguide mode converter," *IEEE Phot. Technol. Lett.* **18**, 43 (2006).
[Hong'02]	K. Hong, H. Zhang, J. M. Mays, A. E. Visser, C. S. Brazel, J. H. Holbrey, W. M. Reichert, and R. D. Rogers, "Conventional free radical polymerization in room temperature ionic liquids: a green approach to commodity polymers with practical advantages," *Chem. Commun.* **13**, 1368 (2002).
[Horst'08]	F. Horst, W. M. Green, B. J. Offrein, and Y. Vlasov, "Echelle grating WDM (de-)multiplexer in SOI technology, based on a design with two stigmatic points," Proc. SPIE 6996, 69960R, (2008).
[Jacquinot'54]	P. Jacquinot, "The luminosity of spectrometers with prisms, gratings, or Fabry-Perot etalons," *J. Opt. Soc. Am.* **44**, 761 (1954).
[Jalali'07]	B. Jalali, "Teaching silicon new tricks," *Nat. Photonics* **1**, 193 (2007).
[Janz'04]	S. Janz, A. Balakrishnan, S. Charbonneau, P. Cheben, M. Cloutier, A. Delâge, K. Dossou, L. Erickson, M. Gao, P.A. Krug, B. Lamontagne, M. Packirisamy, M. Pearson, and D.-X. Xu, "Planar

waveguide echelle gratings in silica-on-silicon," IEEE *Photon. Technol. Lett.* **16**, 503 (2004).

[Jungwirth'05] K. Jungwirth, "Recent highlights of the PALS research program," *Laser and Particle Beams* **23**, 177 (2005).

[Justice'12] J. Justice, C. Bower, M. Meitl, M. B. Mooney, M. A. Gubbins and B. Corbett, "Wafer-scale integration of group III–V lasers on silicon using transfer printing of epitaxial layers," *Nat. Photonics* **6,** 610 (2012).

[Karsten'07] B. Karsten, F. Havermeyer, L. Wenhai, M. Christophe and D. Psaltis, *Holographic filters in photorefractive materials and their applications* (Springer, Berlin, 2007).

[Kim'09] S. H. Kim, R. Takei, Y. Shoji, and T. Mizumoto, "Single-trench waveguide TE-TM mode converter," *Opt. Express* **17**, 11267 (2009).

[Kirchain'07] R. Kirchain and L. Kimerling, "A roadmap for nanophotonics," *Nat. Photonics* **1**, 303 (2007).

[Kiyat'05] I. Kiyat, A. Aydinli and N. Dagli, "A compact silicon-on-insulator polarization splitter," *Phot. Tech. Lett.* **17**, 100 (2005).

[Klingshirn'05] M.A. Klingshirn, S.K. Spear, J.D. Holbrey and R.D. Rogers, "Ionic liquids as solvent and solvent additives for the synthesis of sol–gel materials," *Jour. Mater. Chem.* **15**, 5174 (2005).

[Kogelnik'69] H. Kogelnik, "Coupled Wave Theory for Thick Hologram Gratings" *Bell. Syst. Tech. J.* **48**, 2909 (1969).

[Lee'12] H. Lee, T. Chen, J. Li, O. Painter and K. J. Vahala, "Ultra-low-loss optical delay line on a silicon chip," *Nature Comm.* **3**, 867 (2012).

[Leith'92] E. Leith, G. Chen, Y. Chen, D. Dilworth, J. Lopez, J. Rudd, P.-C. Sun, J. Valdmanis and G. Vossler, "Imaging through scattering media with holography" *J. Opt. Soc. Am. A* **9**, 1148 (1992).

[Leitjens'05] X. Leijtens and M. Smit, "Miniaturization of Passive Devices for Photonic Integration," *Proc. SPIE* 6020, 60201Q (2005).

[Lessard'95] R. A. Lessard and G. Manivannan, "Holographic recording materials: An over-view," *Proc SPIE* **2405**, 2-23 (1995).

[Leung'11] D. M. H. Leung, B. M. A. Rahman, and K. T. V. Grattan, "Numerical analysis of asymmetric silicon nanowire waveguide as compact polarization rotator," *IEEE Phot. J.* **3**, 381 (2011).

[Levy'07] U. Levy, M. Abashin, K. Ikeda, A. Krishnamoorthy, J. Cunningham, and Y. Fainman, "Inhomogenous Dielectric

Metamaterials with Space-Variant Polarizability," *Phys. Rev. Lett.* **98**, 243901 (2007).

[Levy'10] J. S. Levy, A. Gondarenko, M. A. Foster, A. C. Turner-Foster, A. L. Gaeta, and M. Lipson, "CMOS-compatible multiple-wavelength oscillator for on-chip optical interconnects," *Nat. Photonics* **4**, 37 (2010).

[Liang'05] T. K. Liang and H. K. Tsang, "Integrated polarization beam splitter in high index contrast silicon-on-insulator waveguides," *Phot. Tech. Lett.* **17**, 393 (2005).

[Lin'08] H. Lin, P. W. Oliveira and M. Veith, "Ionic liquid as additive to increase sensitivity, resolution, and diffraction efficiency of photopolymerizable hologram material," *Appl. Phys. Lett.* **93**, 141101 (2008).

[Lin'09] H. Lin, P. W. Oliveira, M. Veith, M. Gros and I. Grobelsek, "Optic diffusers based on photopolymerizable hologram material with an ionic liquid as additive," *Opt. Lett.* **34**, 1150 (2009).

[Liu'08a] J. Liu, M. Beals, A. Pomerene, S. Bernardis, R. Sun, J. Cheng, L. Kimerling and J. Michel, "Waveguide-integrated, ultralow energy GeSi electro-absorption modulators," *Nat. Photonics* **2**, 422 (2008).

[Liu'08b] X. Liu, I. Hsieh, X. Chen, M. Takekoshi, J. I. Dadap, N. C. Panoiu, R. M. Osgood Jr., W. M. Green, F. Xia, and Y. A. Vlasov, "Design and fabrication of an ultra-compact silicon on insulator demultiplexer based on arrayed waveguide gratings," presented at *CLEO*, San Jose (USA), May 2008.

[Liu'11] L. Liu, Y. Ding, K. Yvind, and J. M. Hvam, "Efficient and compact TE-TM polarization converter built on silicon-on-insulator platform with a simple fabrication processs," *Opt. Lett.* **36**, 1059 (2011).

[Lockwood'10] D. J. Lockwood and L. Pavesi, *Silicon photonics II: components and integration* (Springer, Berlin, 2010).

[Luo'05] S. Luo, K. Chen, L. Cao, C. Liu, Q. He, G. Jin, D. Zheng and Y. Chen, "Photochromic diarylethene for rewritable holographic data storage," *Opt. Express* **13**, 3123 (2005).

[Madsen'98a] C. K. Madsen, "Efficient architectures for exactly realizing optical filters with optimum bandpass designs" *IEEE Phot. Tech. Lett.* **10**, 1136 (1998).

[Madsen'98b] C. K. Madsen, J. Wagener, T. A. Strasser, D. Muehlner, M. A. Milbrodt, E. J. Laskowski, and J. DeMarco, "Planar waveguide optical spectrum analyzer using a UV-induced grating," *IEEE J. Sel. Top. Quantum Electron.* **4**, 925 (1998).

[Magnusson'78] R. Magnusson and T. K. Gaylord, "Diffraction regimes of transmission gratings," *J. Opt. Soc. Am* **68**, 809 (1978).

[Mak'10] K. F. Mak, M. Y. Sfeir, J. A. Misewich and T. F. Heinz, "The evolution of electronic structure in few-layer graphene revealed by optical spectroscopy," *Proc. Natl. Acad. Sci. USA* **107**, 14999 (2010).

[Martínez'07] Ó. Martínez-Matos, M. L. Calvo, J. A.. Rodrigo, P. Cheben and F. del Monte, "Diffusion study in tailored gratings recorded in photopolymer glass with high refractive index species," *Appl. Phys. Lett.* **91**, 14115 (2007).

[Martínez'09a] Ó. Martínez-Matos, J.A. Rodrigo, M. L. Calvo and P. Cheben, "Polarization and phase-shift properties of high spatial frequency holographic gratings in a photopolymerizable glass," *Opt. Lett.* **34**, 485 (2009).

[Martínez'09b] Ó. Martínez-Matos, J.A. Rodrigo, M. L. Calvo, V. Hevia-Martín, and P. Cheben, "Photopolymerizable glass with high refractive index species: optical performance and emerging implementations," *Optical Memory & Neural Networks* **18**, 21 (2009).

[Martínez'10] Ó. Martínez-Matos, J. A. Rodrigo, M. P. Hernández-Garay, J. G. Izquierdo, R. Weigand, M. L. Calvo, P. Cheben, P. Vaveliuk, and L. Bañares, "Generation of femtosecond paraxial beams with arbitrary spatial distribution," *Opt. Lett.* **35**, 652 (2010).

[Mateus'04] C. F. R. Mateus, M. C. Y. Huang, L. Chen, C. J. Chang-Hasnain, and Y. Suzuki, "Broad-band mirror (1.12-1.62 um) using a subwavelength grating," *IEEE Photon. Technol. Lett.* 16, 1676 (2004).

[Meerholz'94] K. Meerholz, B. L. Volodin, B. Kippelen and N. Peyghambarian, "A photorefractive polymer with high optical gain and diffraction efficiency near 100%," *Nature* **371**, 497 (1994).

[Michelson'87] A. A. Michelson and E. Morley, "On the relative motion of the Earth and the Luminiferous Ether," *Am. J. Sci*. **34**, 333 (1887).

[Mizuno'06] T. Mizuno, M. Oguma, T. Kitoh, Y. Inoue and H. Takahasi, "Lattice-form CWDM interleave filter using silica-based planar lightwave circuit," *IEEE Photon. Technol. Lett.* **18**, 1570 (2006).

[Mok'93] F. H. Mok, "Angle-multiplexed storage of 5000 holograms in litium nioabate," *Opt. Lett.* **18**, 915 (1993).

[Mourou] G. A. Mourou, G. Korn, W. Sandner, and J. L. Collier, *Extreme Light Infrastructure whitebook* (THOSS Media GmbH, Berlin, 2011).

[Mok’00] F. H. Mok, G. Zhou and D. Psaltis, “Holographic Read-Only Memory” in *Holographic Data Storage* (eds. H.J Coufal, D. Psaltis, and G.T. Sincerbox) (Springer, Berlin, 2000).

[Montemezzani’90] G. Montemezzani and P. Günter, “Thermal hologram fixing in pure and doped $KNbO_3$ crystals” *J. Opt. Soc. Am B* **7**, 2323 (1990).

[Moser’09] C. Moser and F. Havermeyer, “Ultra-narrow-band tunable laserline notch filter,” *Appl. Phys. B* **95**, 597 (2009).

[Murciano’04] A. Murciano, S. Blaya, L. Carretero, R. F. Madrigal and A. Fimia “Holographic reflection gratings in photopolymerizable solgel materials,” *Opt. Lett.* **31**, 2317 (2006).

[Nagarajan’10] R. Nagarajan, M. Kato, J. Pleumeekers, P. Evans, S. Corzine, S. Hurtt, A. Dentai, S. Murthy, M. Missey, R. Muthiah, R. A. Salvatore, C. Joyner, R. Schneider, M. Ziari, F. Kish, and D. Welch, “InP Photonic Integrated Circuits,” *IEEE J. Sel. Top. Quantum Electron.* **16**, 1113 (2010).

[Neipp’99] C. Neipp, I. Pascual and A. Beléndez, “Silver halide sensitized gelatin derived from BB-640 holographic emulsion,” *Appl. Opt.* **38**, 1348 (1999).

[Nakajima’11] N. Nakajima, T. Liang, S. Ishida, Y. Tomioka, K. Kihou, C. H. Lee, A. Iyo, H. Eisaki, T. Kakeshita, T. Ito and S. Uchida, “Unprecedented anisotropic metallic state in undoped iron arsenide $BaFe_2As_2$ revealed by optical spectroscopy,” *Proc. Natl. Acad. Sci. USA* **108**, 12238 (2011).

[Nguyen’01] C. Nguyen, “Mode-matching method” in *Analysis methods for RF, microwave, and millimeter-wave planar transmission line structures* (Wiley, New York, 2001).

[Novotny’97] L. Novtny, R. X. Bian and X. S. Xie, “Theory of nanometric optical tweezers,” *Phys. Rev. Lett* **79**, 645 (1997).

[Ohno’06] F. Ohno, K. Sasaki, A. Motegi, and T. Baba, “Reduction in Sidelobe Level in Ultracompact Arrayed Waveguide Grating Demultiplexer Based on Si Wire Waveguide,” *Jpn. J. Appl. Phys.* **45**, 6126 (2006).

[Okamoto’06] K. Okamoto, *Fundamentals of optical waveguides* (Elsevier, 2006).

[Okamoto'10] K. Okamoto, H. Aoyagi, and K. Takada, "Fabrication of Fourier-transform, integrated-optic spatial heterodyne spectrometer on silica-based planar waveguide," *Opt. Lett.* **35**, 2103 (2010).

[Omura'10] K. Omura and Y. Tomita, "Photopolymerization kinetics and volume holographic recording in ZrO2 nanoparticle-polymer composites at 404 nm," *J. Appl. Phys.* **107**, 023107 (2010).

[Ortuño'07] M. Ortuño, E. Fernández, S. Gallego, A. Beléndez and I. Pascual, "New photopolymer holographic recording material with sustainable design," *Opt. Express* **15**, 12425 (2007).

[Pathak'11] S. Pathak, E. Lambert, P. Dumon, D. Thourhout, and W. Bogaerts, "Compact SOI-Based AWG With Flattened Spectral Response Using a MMI," presented in *8th International Conference in Group IV Photonics*, London (UK), September 2011.

[Pearson'00] M. R. T. Pearson, A. Bezinger, A. Delâge, J. W. Fraser, S. Janz, P. E. Jessop, and D.-X. Xu, "Arrayed waveguide grating demultiplexers in silicon-on-insulator," *Proc. SPIE* **3953**, 11 (2000).

[Pelletier'91] M. J. Pelletier and R. C. Reeder, "Characterization of holographic band-reject filters designed for Raman spectroscopy," *Appl. Spectrosc.* **45**, 765 (1991).

[Piazzolla'00] S. Piazzolla and B. K. Jenkins, ”First-harmonic diffusion model for holographic grating formation in photopolymers," *J. Opt. Soc. Am. B* **17**, 1147 (2000).

[Predhel'12] K. Predehl, G. Grosche, S. M. F. Raupach, S. Droste, O. Terra, J. Alnis, Th. Legero**,** T. W. Hänsch, Th. Udem, R. Holzwarth and H. Schnatz, "A 920-kilometer optical fiber link for frequency metrology at the 19th decimal place," *Science* **336**, 441 (2012).

[Psaltis'95] D. Psaltis and F. Mok, "Holographic memories," *Sci. Am.* **273**, 70 (1995).

[Quintanilla'81] M. Quintanilla and A. M. de Frutos, "Holographic filter that transforms a Gaussian into a uniform beam," *Appl. Opt.* **20**, 879 (1981).

[Rakuljic'93] G. A. Rakuljic and V. Leyva, "Volume holographic narrow-band optical filter" *Opt. Lett.* **18**, 459 (1993).

[Ramos'04] G. Ramos, A. Alvarez-Herrero, T. Belenguer, F. del Monte, and D. Levy, ”Shrinkage control in a photopolymerizable hybrid solgel material for holographic recording" *Appl. Opt*. **43**, 4018 (2004).

[Reed'08] T. Reed, *Silicon photonics: the state of the art* (Wiley, Hoboken, 2008).

[Roth’07] J. E. Roth, O. Fidaner, R. K. Schaevitz, Y. H. Kuo, T. I. Kamins, J. S. Harris, and D. A. B. Miller, “Optical modulator on silicon employing germanium quantum wells,” *Opt. Express* **15**, 5851 (2007).

[Rowland’82] H. A. Rowland, “Preliminary notice of results accomplished on the manufacture and theory of gratings for optical purposes,” *Phil. Mag. Suppl.* **13**, 469 (1882).

[Sakaguchi’11] J. Sakaguchi, Y. Awaji, N. Wada, A. Kanno, T. Kawanishi, T. Taru, T. Kobayashi and M. Watanabe, “109-Tb/s (7×97×172-Gb/s SDM/WDM/PDM) QPSK transmission through 16.8-km homogeneous multi-core fiber,” presented at *Optical Fiber Communication Conference*, Los Angeles (USA), June 2011.

[Sanchez’05] C. Sánchez, M. J. Escuti, C. van Heesch, C. W. M. Bastiaansen, D. J. Broer, J. Loos and R. Nussbaumer, “TiO_2 nanoparticle–photopolymer composites for volume holographic recording,” *Adv. Funct. Mat.* **15**, 1623 (2005).

[Sanmamed’07] Y. A. Sanmamed, D. González-Salgado, J. Troncoso, C.A. Cerdeiriña and L. Romaní, “Viscosity-induced errors in the density determination of room temperature ionic liquids using vibrating tube densitometry,” *Fluid phase equilibria* **252**, 96 (2007).

[Schmid’07] J. H. Schmid, P. Cheben, S. Janz, J. Lapointe, E. Post, and D.-X. Xu, “Gradient-index antireflective subwavelength structures for planar waveguide facets,” *Opt. Lett.* **32**, 1794 (2007).

[Schnoes’99] M. G. Schnoes, L. Dhar, M. L. Schilling, S. S. Patel and P. Wiltzius, “Photopolymer-filled nanoporous glass as a dimensionally stable holographic recording medium,” *Opt. Lett.* **24**, 658 (1999).

[Schoen’93] C. L. Schoen, S. K. Sharma, C. E. Helsley and H. Owen, “Performance of a holographic supernotch filter” *Appl. Spectrosc.* **47**, 305 (1993).

[Schwartz’12] E. Schwartz, S. G. Lipson and E. N. Ribak, “Enhanced interferometric identification of spectra in habitable extrasolar Planets,” *Astron J.* **144**, 71 (2012).

[Shankoff’68] T. A. Shankoff, “Phase holography in dichromated gelatin,” *Appl. Opt.* **7**, 2101 (1968).

[Sherwood’08] N. Sherwood-Droz, H. Wang, L. Chen, B. G. Lee, A. Biberman, K. Bergman and M. Lipson, “Optical 4x4 hitless sIlicon router for optical networks-on-chip (NoC),” *Opt. Express* **16**, 15915 (2008).

[Sheu’06] C.-Y. Sheu, S.-F. Lee and K.-H. Lii, “Ionic liquid of choline chloride/malonic acid as a solvent in the synthesis of open-framework iron oxalatophosphates,” *Inorg. Chem.* **45**, 1891 (2006).

[Sincerbox’94] T. Sincerbox, *Current trends in optics* (Academic, London, 1994).

[Smothers’90] W. K. Smothers, B. M. Monroe, A. M. Weber, D. E. Keys “Photopolymers for holograhpy,” *Proc. SPIE* **1212**, 20 (1990).

[Solymar’81] L. Solymar and D.J. Cooke, *Volume holography and volume gratings* (Academic Press, London, 1981).

[Soref’10] R. Soref, *Silicon Photonics: a review of recent literature* (Springer, Berlin, 2010).

[Soref’11] R. Soref, “Reconfigurable integrated optoelectronics,” *Adv. Optoelectron.* **2011**, 1 (2011),

[Suzuki’06] N. Suzuki, Y. Tomita and K. Ohmori, “Highly transparent ZrO2 nanoparticle-dispersed acrylate photopolymers for volume holographic recording,” *Opt. Express* **14**, 12712 (2006).

[Taflove’05] A. Taflove and S. Hagness, *Computational Electrodynamics, The finite-difference time-domain method* (Artech, 2005).

[Takada’90] H. Takada, M. Suzuki, M. Usami, H. Taga, S. Yamamoto and Y. Matsushima, “5-Gb/s performance of integrated light source consisting of $\lambda/4$-shifted DFB laser and EA modulator with SI InP BH structure” *Lightwave Technol. Lett.* **8**, 1357 (1990).

[Takada’11] K. Takada, H. Aoyagi, and K. Okamoto, “Correction for phase-shift deviation in a complex Fourier-transform integrated-optic spatial heterodyne spectrometer with an active phase-shift scheme,” *Opt. Lett.* **36**, 1044 (2011).

[Velasco‘12a] A. V. Velasco, M. L. Calvo, P. Cheben, A. Ortega-Moñux, J. H. Schmid, C. Alonso Ramos, Í. Molina Fernandez, J. Lapointe, M. Vachon, S. Janz, and D.-X. Xu, “Ultracompact polarization converter with a dual subwavelength trench built in a silicon-on-insulator waveguide,” *Opt. Lett* **37**, 365 (2012).

[Vermeulen’10] D. Vermeulen, S. Selvaraja, W. Bogaerts, and G. Roelkens, “High-efficiency broadband CMOS-compatible polarization rotator on SOI,” presented at the *Seventh International Conference on Group IV Photonics*, Beijing (China), September 2010.

[Vodopyanov’08] K. L. Vodopyanov and Y. H. Avetisyan, “Optical terahertz wave generation in a planar GaAs waveguide,” *Opt. Lett.* **33**, 2314 (2008).

[Vest’79] C. M. Vest, *Holographic Interferometry* (Wiley, New York, 1979).

[Wassercheid'03] P. Wassercheid and T. Welton, *Ionic Liquids in Synthesis* (Wiley, Weinheim, 2003).

[Wilson'10] W. Wilson, A. Hoskins, M. Ayres, A. Hill and K. Curtis, *Holographic Data Storage: From Theory to Practical Systems* (John Wiley & Sons, Ltd, Chichester, 2010).

[Xia'07a] F. Xia, M. Rooks, L. Sekaric, and Y. Vlasov, "Ultra-compact high order ring resonator filters using submicron silicon photonic wires for on-chip optical interconnects," *Opt. Express* **15**, 11934 (2007).

[Xia'07b] F. Xia, L. Sekaric, and Y. Vlasov, "Ultracompact optical buffers on a silicon chip," *Nat. Photonics* **1**, 65 (2007).

[Xie'02] C. Xie, M. A. Dinno and Y. Li, "Near infra-red Raman spectroscopy of single optically trapped biological cells," *Opt. Lett.* **27**, 249 (2002).

[Xu'94] C. L. Xu, W. P. Huang, M. S. Stern and S. K. Chaudhuri, "Full-vectorial mode calculations by finite difference method," *IEEE P-Optoelectron* **141**, 281 (1994).

[Wen'11] Y. H. Wen, O. Kuzucu, T. Hou, M. Lipson, and A. L. Gaeta, "All-optical switching of a single resonance in silicon ring resonators," *Opt. Lett.* **36**, 1413 (2011).

[Wilken'12] T. Wilken, G. Lo Curto, R. A. Probst, T. Steinmetz, A. Manescau, L. Pasquini, J. I. González-Hernández, R. Rebolo, T. W. Hänsch, T. Udem and R. Holzwarth, "A spectrograph for exoplanet observations calibrated at the centimetre-per-second level," *Nature* **485**, 611(2012).

[Yamauchi'08] J. Yamauchi, M. Yamanoue, and H. Nakano, "A short polarization converter using a triangular waveguide," *J. Lightwave Technol.* **26**, 1708 (2008).

[Yang'09] J. Yang, D. Hüvonen, U. Nagel, T. Room, N. Ni, P. C. Canfield, S. L. Bud'ko, J. P. Carbotte and T. Timusk, "Optical Spectroscopy of Superconducting $Ba_{0.55}K_{0.45}Fe_2As_2$: Evidence for Strong Coupling to Low-Energy Bosons," *Phys. Rev. Lett.* **102**, 187003 (2009).

[Yee'66] K. Yee, "Numerical solution of initial boundary value problems involving Maxwell's equations in isotropic media," *IEEE T. Antenn. Propag.* **14**, 302 (1966).

[Yue'09] Y. Yue, L. Zhang, M. Song, R. G. Beausoleil, and A. E. Willner, "Higher-order-mode assisted silicon-on-insulator 90^o degree polarization rotator," *Opt. Express* **17**, 20694 (2009).

[Zhang'04] Y. Zhang, R. Burzynski, S. Ghosal and M. K. Casstevens, "Photorefractive polymers and composites," *Adv. Mat.* **8**, 111 (2004).

[Zhang'10] J. Zhang, T. Y. Liow, M. Yu, G. Q. Lo, and D. L. Kwong, "Silicon waveguide based TE mode converter," *Opt. Express* **18**, 25264 (2010).

[Zhao'95] C. Z. Zhao, G. Z. Li, E. K. Liu, Y. Gao and X. D. Liu "Silicon on insulator Mach–Zehnder waveguide interferometers operating at 1.3 µm," *App. Phys. Lett*. **67**, 2448 (1995).

[Zheng'10] X. Zheng, I. Shubin, G. Li, T. Pinguet, A. Mekis, J. Yao, H. Thacker, Y. Luo, J. Costa, K. Raj, J. E. Cunningham, and A. V. Krishnamoorthy, "A tunable 1x4 silicon CMOS photonic wavelength multiplexer/demultiplexer for dense optical interconnects," *Opt. Express* **18**, 5151 (2010).

[Zheng'12] X. Zheng, F. Y. Liu, J. Lexau, D. Patil, Li. Guoliang, Y. Luo, H. D. Thacker, I. Shubin, J. Yao, K. Raj, R. Ho, J. E. Cunningham and A. V. Krishnamoorthy, "Ultralow Power 80 Gb/s Arrayed CMOS Silicon Photonic Transceivers for WDM Optical Links," *J. Lightwave Technol.* **30**, 641 (2012).

[Zhu'06] L. Zhu, Y. Huang, and A. Yariv, "Integration of a multimode interference coupler with a corrugated sidewall Bragg grating in planar polymer waveguides," *IEEE Phot. Tech. Lett* **18**, 740 (2006).

List of acronyms

AA	Acrylamide
AWG	Arrayed Waveguide Grating
CCD	Charge-coupled device
CMOS	Complementary metal-oxide-semiconductor
DEMUX	Demultiplexer
ELI	Extreme Light Infrastructure
EME	Eigenmode Expansion
ER	Extinction Ratio
FDTD	Finite Difference Time Domain
FSR	Free Spectral Range
FT	Fourier Transform
FWHM	Full Width at Half Maximum
GMPTS	Glycidoxypropyltrimethoxysilane
HOE	Holographic Optical Element
HRIS	High Refractive Index Species
HSQ	Hydrogen Silsesquioxane
ICP	Inductively Coupled Plasma
IL	Ionic Liquid
IR	Infra-red
LIDT	Laser-induced Damage Threshold
MA	Metacrylic Acid
MUX	Multiplexer
MZI	Mach-Zehnder Interferometer

Nd:YAG	Neodymium-doped Yttrium Aluminum Garnet
NRC	National Research Council
PIC	Photonic Integrated Circuit
PALS	Prague Asterix Laser System
POEA	Phenoxyethyl acrylate
RIE	Reactive Ion Etch
SEM	Scanning Electron Microscopy
SHFT	Spatial Heterodyne Fourier Transform
SOI	Silicon-On-Insulator
SWG	Sub-wavelength Grating
TE	Transversal Electric
TEOS	Tetraethylorthosilicate
TM	Transversal Magnetic
UV	Ultra-violet
VPHG	Volume Phase Holographic Grating
WORM	Write Once Read Many

Publications

Aitor Villafranca Velasco (signed as A. V. Velasco)

Journal Papers (ISI, peer reviewed)

(1) A. V. Velasco, M. P. Hernández-Garay, M. L. Calvo, P. Cheben and F. Del Monte, "Photopolymerizable glasses incorporating high refractive index species and ionic liquid: A comparative study," *J. App. Phys.* **109**, 053106 (2011).

(2) A. V. Velasco, M. L. Calvo, P. Cheben, A. Ortega-Moñux, J. H. Schmid, C. Alonso Ramos, Í. Molina Fernandez, J. Lapointe, M. Vachon, S. Janz, and D.-X. Xu, "Ultracompact polarization converter with a dual subwavelength trench built in a silicon-on-insulator waveguide," *Opt. Lett* **37**, 365 (2012).

(3) A. V. Velasco, P. J. Bock, P. Cheben, M. L. Calvo, J. H. Schmid, J. Lapointe, D.-X. Xu, S. Janz and A. Delâge "Bandpass filter implemented with blazed waveguide sidewall gratings in silicon-on-insulator," *Elec. Lett.* **48**, 715 (2012).

(4) P. Bock, P. Cheben, J. Schmid, A. V. Velasco, A. Delâge, S. Janz, D.-X. Xu, J. Lapointe, T. J. Hall and M. L. Calvo, "Demonstration of a curved sidewall grating demultiplexer on silicon," *Opt. Express* **20**, 19882 (2012).

(5) A. V. Velasco, M. L. Calvo and P. Cheben, "Photopolymerizable organically modified holographic glass with enhanced thickness for spectral filters," *J. Appl. Phys.* **113**, 033101 (2013).

(6) A. V. Velasco, P. Cheben, P. J. Bock, A. Delâge, J. H. Schmid, J. Lapointe, S. Janz, M. L. Calvo, D.-X. Xu, M. Florjanczyk and M. Vachon, "High resolution Fourier-transform spectrometer chip with microphotonic silicon spiral waveguides," *Opt. Lett.* **38**, 706 (2013).

(7) A. V. Velasco, P. Cheben, P. J. Bock, A. Delâge, J. H. Schmid, J. Lapointe, S. Janz, M. L. Calvo, D.-X. Xu, and M. Florjanczyk, "Espectrómetro de transformada de Fourier implementado mediante guías de onda en espiral con base de silicio," *Opt. Pura Apl.* **46**, 99 (2013).

Conferences, workshops and schools

Invited

(8) M. L. Calvo*, P. Cheben, M. P. Hernández-Garay, A. V. Velasco and O. Martínez-Matos, “Holographic photopolymerizable glasses: current challenges for emerging optical information storage and laser beams manipulation applications,” *Photonics 2010*, Guwahati (India), December 2010.

(9) P. Cheben*, J.H. Schmid, P.J. Bock, J. Lapointe, S. Janz, D.-X. Xu1 A. Delâge, M. Vachon, R. Halir, A. Ortega-Moñux, C. Alonso Ramos, I. Molina-Fernandez, J.-M. Fédéli, M. Ibrahim, W.N. Ye, A.V. Velasco, M.L. Calvo and I. Glesk, “Refractive Index Engineering with Sub-Wavelength Gratings in Silicon Waveguides,” *Integrated Photonics Research*, Colorado (United States), June 2012.

(10) M. L. Calvo*, T. Alieva, O. Martínez-Matos, J. A. Rodrigo, A. V. Velasco, Pavel Cheben, M. P. Hernández-Garay and A. Cámara, “Holographic photopolymerizable glasses: current challenges for emerging optical information storage and laser beams manipulation applications,” *Optics Within Life Science*, Genova (Italy), July 2012.

(11) P. Cheben*, J. H. Schmid, P. J. Bock, J. Lapointe, S. Janz, D.-X. Xu A. Delâge, M. Vachon, R. Halir, A. Ortega-Moñux, C. Alonso Ramos, I. Molina-Fernandez, J.-M. Fédéli, M. Ibrahim, W. N. Ye, A. V. Velasco, M. L. Calvo and I. Glesk. “Subwavelength Structures in Integrated Optics,” *Optical Fiber Communication Conference*, Anaheim (United States), March 2013.

(12) A. V. Velasco*, M. L. Calvo, P. Cheben, M. Florjańczyk, P. J. Bock, A. Delâge, J. H. Schmid, J. Lapointe, S. Janz, D.-X. Xu and M. Vachon, “High resolution Fourier-transform microspectroscopy based on spiral silicon waveguides,” *International Conference on Transparent Optical Networks (ICTON)*, Cartagena (Spain), June 2013.

(13) P. Cheben*, A. V. Velasco, R. Halir, C. Alonso-Ramos, P.J. Bock, J.H. Schmid, A. Ortega-Moñux, A. Maese, M. Ibrahim, D.-X. Xu, J. Lapointe, S. Janz, A. Delâge, M. Vachon, A. Aleali, W.N. Ye, I. Molina-Fernández, M.L. Calvo, and L. Vivien, “Recent advances in subwavelength engineering in integrated optics,” *International Conference on Transparent Optical Networks (ICTON)*, Cartagena (Spain), June 2013.

Oral

(14) A. V. Velasco*, M. P. Hernández-Garay, M.L. Calvo, P. Cheben and F. Del Monte, "Study of holographic diffraction gratings implemented in photopolymerizable glasses incorporating ionic liquid," *Conference on Applications of Optics and Photonics*, Braga (Portugal), Apr. 2011.
PUBLICATION: *Proc. SPIE* **8001**, International Conference on Applications of Optics and Photonics (M. F. Costa, ed.), 80010N (July 26, 2011); doi: 10.1117/12.891523.

(15) A. V. Velasco*, M. P. Hernández-Garay, M.L. Calvo, P. Cheben and F. Del Monte, "Study of photopolymerizable sol-gel glasses incorporating ionic liquid," *Information Photonics*, Ottawa (Canada), May 2011.
PUBLICATION: *Proc. IP 2011* (P. Cheben, ed.) *Proc. IEEE*, IEEE Catalog Number: CFP1141N-CDR. ISBN: 978-1-61284-317-9.

(16) P. Cheben*, P. J. Bock, J. H. Schmid, J. Lapointe, S. Janz, D.-X. Xu, R.Ma, A. Densmore, A. Delâge, B. Lamontagne, R.Halir, I. Molina-Fernández, A. Ortega-Moñux, C. Alonso- Ramos, A.V. Velasco, M. L. Calvo, I. Glesk, J.-M. Fédéli, L. Vivien, M. Ibrahim and W. N. Ye, "Subwavelength silicon nanophotonics," *International Conference on Micro and nano-photonics materials and devices*, COST MP0702, Trento (Italy), January 2012.
PUBLICATION: *Proc. MINAP 2012* (M. Ferrari, M. Marciniak, G. C. Righini, T. Szoplik and S. Varas, eds.), CNR, page 29. ISBN: 978-83-7798-020-0.

(17) A. V. Velasco*, P. Cheben, P. J. Bock, J. H. Schmid, J. Lapointe, A. Delage, M. L. Calvo, S. Janz, D.-X. Xu and M. Florjanczyk, "Spatial heterodyne Fourier-yransform spectrometer implemented with silicon wire spiral waveguides," *European Conference on Integrated Optics*, Barcelona (Spain), April 2012.

(18) A. V. Velasco*, M. L. Calvo, P. Cheben, A. Ortega-Moñux, J. H. Schmid, C. Alonso Ramos, Í. Molina Fernandez, J. Lapointe, M. Vachon, S. Janz, and D.-X. Xu, "Ultra-compact polarization mode converter implemented in a dual-trench Silicon-On-Insulator waveguide," *Conference on Laser and Electro Optics*, San Jose (United States), May 2012.
PUBLICATION: *CLEO: Science and Innovations, OSA Technical Digest* (Optical Society of America, 2012), paper CM4M.5.

(19) A. V. Velasco*, M. L. Calvo, P. Cheben, A. Ortega-Moñux, J. H. Schmid, C. Alonso Ramos, Í. Molina Fernandez, J. Lapointe, M. Vachon, S. Janz, and D.-X. Xu, "Ultra-compact Silicon-On-Insulator polarization converter implemented in a dual-trench waveguide," *Photonics North*, Montreal (Canada), June 2012. Student awardee.

(20) A. V. Velasco*, P. Cheben, P. J. Bock, J. H. Schmid, J. Lapointe, A. Delâge, M. L. Calvo, S. Janz, D.-X. Xu and M. Florjańczyk, “Espectrómetro de transformada de Fourier implementado mediante guías de onda en espiral con base de silicio,” *Reunión Nacional de Óptica*, Zaragoza (Spain), September 2012. Invited as awardee (AVV). Young researcher awardee.

(21) A. V. Velasco*, P. Cheben, P. J. Bock, J. H. Schmid, J. Lapointe, A. Delâge, M. L. Calvo, S. Janz, D.-X.. Xu and M. Florjańczyk, “High resolution Fourier-transform microspectrometers in Silicon-on-Insulator waveguides,” *Convención Española de Nanofotónica*, Carmona (España), October 2012. Student awardee.

(22) P. Cheben*, A. V. Velasco, C. Alonso, P. J. Bock, J. H. Schmid, J. Lapointe, A. Delâge, S. Janz, M. L. Calvo, D.-X. Xu and M. Florjańczyk, “Fourier-transform spectrometer chip with silicon spiral waveguides,” *SPIE Optics and optoelectronics*, Prague (Czech Republic), April 2013.

Poster

(23) P. Domínguez-García*, M.A. Rubio, A. V. Velasco, M.P. Hernández-Garay, M.L. Calvo and P. Cheben, “Single-particle micro-rheology of photopolymerizable sol-gel materials for optical applications,” *Colloids and materials*, Amsterdam (Holland), May 2011.

(24) P. A. Mantashyan*, V. E. Nersesyan, R. Kh. Drampyan, A. V. Velasco, P. Cheben and M. L. Calvo, “Optical implementation of annular photonic lattices by Bessel beam technique in photopolymerizable sol-gel glass,” *Frontiers in Optics and Photonics*, Yerevan (Armenia), July 2012.

(25) A. V. Velasco*, M. Calvo and P. Cheben, “Ultracompact polarization and spectral handling in Silicon-On-Insulator,” *Silicon Photonics Winter School*, Tokyo (Japan), January 2013. Invited through grant from JSPS.

Patents

(26) A. V. Velasco, M. Calvo and P. Cheben, “Filtro holográfico y método de síntesis de filtros holográficos,” **P201201084** (October 2012).

---

*presented by